Control of Hox transcription factor concentration and cell-to-cell variability by an auto-regulatory switch

Dimitrios K. Papadopoulos[1,*], Kassiani Skouloudaki[1], Ylva Engström[2], Lars Terenius[3], Rudolf Rigler[4,5], Christoph Zechner[1,6], Vladana Vukojević[3] and Pavel Tomancak[1,*]

[1]Max-Planck Institute of Molecular Cell Biology and Genetics, 01307 Dresden, Germany
[2]Department of Molecular Biosciences, The Wenner-Gren Institute, Stockholm University, 10691 Stockholm, Sweden
[3]Center for Molecular Medicine (CMM), Department of Clinical Neuroscience, Karolinska Institutet, 17176 Stockholm, Sweden
[4]Department of Medical Biochemistry and Biophysics, Karolinska Institutet, 17177 Stockholm, Sweden
[5]Laboratory of Biomedical Optics, Swiss Federal Institute of Technology, 1015 Lausanne, Switzerland
[6]Center for Systems Biology Dresden, 01307, Dresden, Germany
[*]Correspondence: papadopo@mpi-cbg.de and tomancak@mpi-cbg.de

Author contributions: DKP and VV, designed and performed the binding study of *Antp*, analyzed the data; DKP and KS, designed and performed the study of *Antp* relative transcript abundance, analyzed the data; YE, provided the *Antp* P1 and P2 reporter lines; DKP and PT, conceived the comparative analysis of TFs and the examination of Antp variability in second instar imaginal discs; CZ, developed the mathematical model of stochastic Antp expression, DKP, conceived the project, designed and performed all remaining experiments, analyzed the data, prepared figures and wrote the manuscript with critical input from KS, YE, CZ, VV and PT; all authors critically reviewed the manuscript and approved it for submission.

Abstract

Concentration of transcription factors (TFs) and their cell-to-cell protein variability are important functional determinants in development, yet how variability is controlled remains poorly understood. Using Fluorescence Correlation Spectroscopy (FCS), we characterized in live *Drosophila* imaginal discs the concentration and cell-to-cell variability of 14 endogenously tagged TFs. We found that the Hox TF Antennapedia (Antp) transitioned from a low concentration/high variability state early in development to a high concentration/low variability state later in development. Using FCS and temporally resolved genetic studies, we uncovered that Antp is necessary and sufficient to drive a developmental regulatory switch from auto-activation to auto-repression, thereby reducing variability. This switch is controlled by a progressive change in relative concentrations of preferentially activating and repressing Antp protein isoforms, which bind to chromatin with different affinities. We derived a simple mathematical model, confirming that the Antp auto-regulatory circuit would suffice to increase protein concentration while suppressing variability over time.

Introduction

In order to understand the mechanisms that control pattern formation and cell fate specification in developing organisms, the intranuclear concentration, DNA-binding kinetics and cell-to-cell variability of relevant TFs need to be quantitatively characterized. TF concentration variability at the tissue level is thought to arise from diverse processes, including mRNA transcription, protein production and degradation. For example, gene transcription in a given tissue is a noisy process. The noise is due to stochastic binding and interactions of proteins involved in

transcriptional activation of the specific gene (intrinsic noise) (Blake et al., 2003; Elowitz et al., 2002) and also due to differences among cells in terms of abundance of the transcriptional and post-transcriptional cellular machinery which affects the efficiency of transcriptional activation in general (extrinsic noise) (Swain et al., 2002). These can influence the expression and production of functional protein, resulting in protein concentration that exhibits variability among cells.

In undifferentiated tissue or cells, TF cell-to-cell variability can be the driving force for differentiation. For example, progressive establishment of a Nanog salt-and-pepper expression pattern leads to the formation of primitive endoderm in the mouse preimplantation embryo, whereas loss of the variability results in embryos lacking primitive endoderm entirely (Kang et al., 2013). In Drosophila, the Senseless (Sens) TF is required for the establishment of proper number of sensory organ precursors in the ectodermal proneural cluster of cells and unequal concentration among cells is required for their specification (Li et al., 2006). Moreover, variability in concentration (rather than its overall average concentration) of the Yan TF drives the transition of developing photoreceptor cells to a differentiated state during Drosophila eye development (Pelaez et al., 2015).

Conversely, in already differentiated tissue or cells, TF expression variability among cells may need to be counteracted to ensure homogeneity of gene expression patterns and robustness of commitment to a certain transcriptional regime. Such homogenization of expression levels has been identified for the Snail (Sna) TF, which is required for the invagination of the mesoderm during Drosophila gastrulation (Boettiger and Levine, 2013), or the Bicoid (Bcd) and Hunchback (Hb) TFs during early embryogenesis (Gregor et al., 2007a; Gregor et al., 2007b; Little et al., 2013). These studies have quantified the tolerable degrees of concentration

variability that allow establishment of gene expression territories with remarkable precision in the developing embryo.

In addition, differential fates within the same developmental territory may be specified by TFs deploying different DNA-binding dynamics despite the existence of very similar concentrations (i.e. low variability). For example, studies on the Oct4 TF in early mouse embryos have shown that differential kinetic behavior of DNA binding, despite equal Oct4 concentration among blastomeres, ultimately dictates an early developmental bias towards lineage segregation (Kaur et al., 2013; Plachta et al., 2011).

So far, gene expression variability studies have focused predominantly on monitoring the noise of mRNA production (Holloway et al., 2011; Holloway and Spirov, 2015; Little et al., 2013; Lucas et al., 2013; Pare et al., 2009). Little information exists about TF variability at the protein level within a tissue, since studies of this sort would require the use of quantitative methods with single-molecule sensitivity.

We have previously used Fluorescence Microscopy Imaging and FCS, to study Hox TF interactions with nuclear DNA in living salivary gland cells (Papadopoulos et al., 2015; Vukojevic et al., 2010). FCS has also been instrumental for the quantification of TF dynamics in living cells or tissue in several recent studies (Clark et al., 2016; Kaur et al., 2013; Lam et al., 2012; Mistri et al., 2015; Papadopoulos et al., 2015; Perez-Camps et al., 2016; Szaloki et al., 2015; Tiwari et al., 2013; Tsutsumi et al., 2016). Yet, in these studies, protein mobility has been measured in overexpressing systems. However, to understand TF behavior *in vivo*, proteins need to be quantified at endogenous levels (Lo et al., 2015).

105 In this study, we take advantage of the availability of fly toolkits, in which TFs
106 have been endogenously tagged by different methodologies: fosmid, BAC, FlyTrap
107 and MiMIC lines (Buszczak et al., 2007; Ejsmont et al., 2011; Ejsmont et al., 2009;
108 Kelso et al., 2004; Morin et al., 2001; Quinones-Coello et al., 2007; Sarov et al.,
109 2016; Venken et al., 2011), to measure the intranuclear concentration of various TFs
110 *in vivo* by FCS, and their cell-to-cell variability in several fly imaginal discs. The
111 imaginal discs are flat, single-layered epithelia comprised of small diploid cells and
112 many TFs are expressed in defined regions within these tissues during development.
113 In this system, we found that Antp, a well-characterized homeotic selector gene,
114 responsible for specification of thoracic identity in fly tissues, displayed high cell-to-
115 cell variability during early disc development and this variability was suppressed at
116 later developmental stages. Through a combination of genetics, single-molecule
117 measurements of TF dynamics by FCS and computational modeling, we uncovered
118 a mechanism that controls Antp concentration and variability in developing discs.
119

120 ## Results

121

122 Characterization of average protein concentrations and cell-to-cell variability of
123 *Drosophila* TFs

124 Average concentrations of TFs in neighboring nuclei of third instar imaginal
125 discs were measured by FCS (Figure 1 A-J and Figure 1 – figure supplement 1 A-P).
126 FCS is a non-invasive method with single molecule sensitivity, in which a confocal
127 arrangement of optical elements is used to generate a small (sub-femtoliter) volume
128 inside living cells, from which fluorescence is being detected (Figure 1 C and D,
129 green ellipsoid). Fluorescent molecules diffuse through this observation volume,

yielding fluorescence intensity fluctuations that are recorded over time by detectors with single-photon sensitivity (Figure 1 E). These fluctuations are subsequently subjected to temporal autocorrelation analysis, yielding temporal autocorrelation curves (henceforth referred to as FCS curves, Figure 1 F), which are then fitted with selected models to extract quantitative information about the dynamic processes underlying the generation of the recorded fluctuations. In the case of molecular movement of TFs (Supplement 1), information can be obtained regarding: a) the absolute concentrations of TFs (Figure 1 F), (b) TF dynamic properties, such as: diffusion times, differences in their interactions with chromatin and fractions of free-diffusing *versus* chromatin-bound TFs (Figure 1 G); and c) TF cell-to-cell concentration variability (Figure 1 H).

For the 14 selected TFs, we measured average concentrations ranging about two orders of magnitude among different TFs, from $\sim 30\, nM$ to $\sim 1.1\, \mu M$ (Figure 1 I and Figure 1 – figure supplement 1 A-Q). We also obtained various diffusion times and fractions of slow and fast diffusing TF molecules (Figure 1 J), indicating differential mobility and degree of DNA-binding among different TFs (Vukojevic et al., 2010). Comparison of the y-axis amplitudes at the smallest lag time of the FCS curves (the points at which the FCS curves cross the y-axis), which are inversely proportional to the concentration of fluorescent molecules (Figure 1 F), gives information about concentration variability (heterogeneity) among different cell nuclei, i.e. reflects heterogeneity of protein concentration at the tissue level (Figure 1 H). We measured the variability of all 14 TFs in our dataset (expressed as the variance over the mean squared, $CV^2 = \frac{s^2}{m^2}$) to be in the range $7 - 37\%$ (Figure 1 K and Figure 1 – figure supplement 1 Q). These numbers are consistent with previous

observations (Sanchez et al., 2011). We then used this dataset as a starting point for studying the control of variability during imaginal disc development.

Since low variability at the tissue level is likely to be achieved through some active mechanism that controls it, we searched for TFs that exhibited low variability and relatively high concentrations. One TF, the Hox gene Antp, had comparatively lower variability ($CV^2 < 0.2$) for its high average concentrations (Figure 1 K), in particular in the leg disc. This distinction prompted us to measure variability of Antp at different concentrations by examining clusters of neighboring cells from across the disc displaying different average expression levels (Figure 1 L). Because FCS performs best at low to moderate expression levels, we performed this analysis in the wing disc (Figure 1 L). We established that the observed fluorescence intensity fluctuations were caused by diffusion of TF molecules through the illuminated confocal volume (Figure 1 – figure supplement 2 and Supplement 1). Our data showed that Antp cell-to-cell variability decreased with increasing Antp concentration (Figure 1 M), suggesting complex transcriptional regulatory processes (Franz et al., 2011; Smolander et al., 2011) that we further investigated using the powerful *Drosophila* genetic toolkit.

Control of Antp concentration by transcriptional auto-regulation

One mechanism by which genes control their expression level variability is auto-regulation (Becskei and Serrano, 2000; Dublanche et al., 2006; Gronlund et al., 2013; Nevozhay et al., 2009; Shimoga et al., 2013; Thattai and van Oudenaarden, 2001). To test whether Antp can regulate its own protein levels, we monitored the concentration of endogenous Antp protein upon overexpression of *Antp* from a transgene. To distinguish between overexpressed and endogenous protein, we used

179 synthetic Antp (SynthAntp) transgenes fused to eGFP (SynthAntp-eGFP). These
180 transgenes encode the Antp homeodomain, the conserved YPWM motif and the C
181 terminus (but lack the long and non-conserved N terminus of the protein, against
182 which Antp antibodies have been raised) and they harbor Antp-specific homeotic
183 function (Papadopoulos et al., 2011). Clonal overexpression of *SynthAntp-eGFP* in
184 the wing disc notum (Figure 2 A-B' and controls in Figure 2 – figure supplement 1 D
185 and D') repressed the endogenous Antp protein, indicating that Antp is indeed able
186 to regulate its own protein levels.

187 Since Antp is a TF, we next asked whether the auto-repression indeed occurs
188 at the transcriptional level. The *Antp* locus is subject to complex transcriptional
189 regulation, involving a distal and a proximal promoter (P1 and P2 promoters,
190 respectively), spanning more than 100 kb of regulatory sequences. We established
191 that the P1 promoter (rather than the P2 promoter) is predominantly required to drive
192 expression of Antp in the wing disc notum (Figure 2 – figure supplement 1 A-C'), in
193 line with previous observations ((Engstrom et al., 1992; Jorgensen and Garber,
194 1987; Zink et al., 1991) and Materials and Methods). Moreover, mitotic
195 recombination experiments in regions of the wing disc unique to P2 transcription
196 have shown no function of the P2 promoter transcripts in wing disc development
197 (Abbott and Kaufman, 1986). Thus, the P1 Antp reporter serves as a suitable
198 reporter of the *Antp* locus transcriptional activity in this context.

199 Clonal overexpression of SynthAntp-eGFP in the wing disc repressed the
200 *Antp* P1 transcriptional reporter (Figure 2 C and C' and controls in Figure 2 – figure
201 supplement 1 E and E'). To rule out putative dominant negative activity of the small
202 synthetic Antp-eGFP peptide, we also performed these experiments with the full-
203 length Antp protein (Figure 2 – figure supplement 1 F and F'). We conclude that the

Antp protein is able to repress its own transcription from the P1 promoter, suggesting a possible mechanism of suppressing cell-to-cell variability of Antp expression levels (Figure 2 D).

In the course of these experiments, we noticed that ectopic overexpression of *SynthAntp-eGFP* or the full-length Antp protein from the *Distal-less* (*Dll*) (MD23) enhancer surprisingly resulted in activation of the *Antp* P1 reporter in distal compartments of the wing disc, such as the wing pouch, where Antp is normally not detected (Figure 2 E-F' and controls in figure 2 – figure supplement 1 G-H'). This finding suggests that next to its auto-repressing function, Antp is also capable to activate its own transcription (Figure 2 G).

To exclude that the auto-activation and repression of Antp are artifacts of overexpression, we measured by FCS the concentration of Antp triggered by different Gal4-drivers and found it to directly correlate with the degree of its homeotic transformation capacity (Figure 2 – figure supplement 2 A-I). Importantly, we observed indistinguishable DNA-binding behavior not only across the whole concentration range examined (Figure 2 – figure supplement 2 J), but also between endogenous and overexpressed Antp (Figure 2 – figure supplement 3 A-B). Importantly, the auto-activating and auto-repressing capacity of Antp was preserved even with the weak Gal4-driver *69B* (Figure 2 – figure supplement 2 K-P) that triggered concentrations of Antp slightly lower than its normal concentration in the wing disc ($473\,nM$ versus $501\,nM$), indicating that auto-activation and auto-repression of Antp take place at endogenous concentrations.

We conclude that, Antp is able to repress and activate its own transcription (Figure 2 D and G) and hypothesize that this auto-regulatory circuit somehow sets the correct concentration of Antp protein in imaginal discs.

229

230 A temporal switch controls the transition of *Antp* from a state of auto-activation to a
231 state of auto-repression

232 To further investigate the mechanism by which the Antp auto-regulatory circuit
233 sets the Antp expression levels precisely, we next asked whether the seemingly
234 opposing auto-regulatory activities of Antp are separated in time during
235 development. To that end, we induced gain-of-function clones of full-length untagged
236 *Antp* either at 26 h (first larval instar – henceforth referred to as "early" stage) or at
237 60 h (late second larval instar – henceforth referred to as "late" stage) of
238 development and analyzed the clones in late third instar wing imaginal discs (Figure
239 3). As a pre-requisite for this analysis, we established that the Antp-eGFP
240 homozygous viable MiMIC allele recapitulates the endogenous Antp pattern in the
241 embryo and all thoracic imaginal discs and therefore can be used to monitor
242 endogenous Antp protein (Figure 3 – figure supplement 1). Clonal induction of full-
243 length untagged *Antp* in early development triggered strong auto-activation of Antp-
244 eGFP (Figure 3 A, B and B' and controls in Figure 3 – figure supplement 2 A-C'). As
245 before, we confirmed that early auto-activation of Antp is transcriptional and similar
246 for both full-length and SynthAntp proteins (Figure 3 – figure supplement 2 D-E' and
247 controls in F-G'). Early auto-activation was further supported by a loss-of-function
248 experiment, where *RNAi*-mediated early knockdown of Antp resulted in
249 downregulation of the Antp reporter (Figure 3 C and C' and controls in Figure 3 –
250 figure supplement 2 H and H'). The loss and gain-of-function analysis together
251 suggest that during early disc development Antp is required for sustaining its own
252 expression.

In contrast, clonal induction during the late second instar stage (Figure 3 F) repressed Antp-eGFP (Figure 3 G and G') and, reciprocally, the clonal knockdown by *RNAi* triggered auto-activation of Antp transcription (Figure 3 H and H'). Hence, in contrast to early development, Antp represses its own expression in third instar discs.

While the gain-of-function experiments show that Antp is sufficient to execute auto-regulation, loss-of-function analysis indicates that it is also necessary for both repression and activation at the transcriptional level.

Together, these results revealed the existence of a switch in Antp auto-regulatory capacity on its own transcription during development. Starting from a preferentially auto-activating state early in development (Figure 3 D), it changes into an auto-inhibitory mode at later developmental stages (Figure 3 I).

Antp switches from a low-concentration/high-variability to a high-concentration/low-variability state

If the *Antp* auto-repressive state limits the variability of Antp protein concentration among neighboring cells late in development, we expected that the variability would be higher during earlier stages, when auto-repression does not operate. We, therefore, monitored the endogenous expression levels and cell-to-cell variability of Antp nuclear concentration in second instar wing and leg discs by FCS. We observed significantly lower average concentrations of Antp protein in second versus third instar wing and leg discs and the inverse was true for concentration variability (Figure 3 E and Figure 3 – figure supplement 3 A, A' and C), indicating that the developmental increase in concentration is accompanied by suppression of concentration variability. In addition, FCS analysis revealed a notable change in Antp

characteristic decay times (signifying molecular diffusion, limited by chromatin-binding) at early versus late stages (Figure 3 E and Figure 3 – figure supplement 3 B). This behavior indicates that endogenous Antp is initially fast moving in the nucleus and undergoes considerably fewer interactions with chromatin, compared to later stages where its interactions with chromatin are more frequent and longer lasting.

Taken together, our FCS measurements show that *Antp* is expressed at relatively low and highly variable levels in early developing discs, when genetic evidence indicates auto-activation capacity on its own transcription. Later in development, when Antp has reached a state of higher average concentrations, auto-repression kicks in, resulting in considerably lower variability among neighboring cells.

Dynamic control of Antp auto-regulation by different Antp isoforms

The changing binding behavior of Antp on chromatin from second to third instar discs and the developmental transition from an auto-activating to an auto-repressing state suggested a causal relationship between the two phenomena. We, therefore, sought to identify molecular mechanisms that could link the observed changes in Antp chromatin-binding to Antp auto-activation and repression. It is well established that the Antp mRNA contains an alternative splice site in exon 7 immediately upstream of the homeobox-containing exon 8, and generates Antp isoforms differing in as little as 4 amino acids in the linker between the YPWM motif (a cofactor-interacting motif) and the homeodomain (Figure 4 A) (Stroeher et al., 1988). Our previous observation that long linker isoforms favor transcriptional activation of Antp target genes, whereas short linker ones favor repression of Antp

303 targets (Papadopoulos et al., 2011), prompted us to examine whether the linker
304 length is also responsible for differences in auto-regulation.

305 Ectopic expression of SynthAntp-eGFP peptides featuring a long linker
306 displayed significantly weaker repression capacity on endogenous Antp, as
307 compared to their short linker counterparts (Figure 4 B, B', F and F' and quantified in
308 D and H, see also Materials and Methods). We confirmed that, also in this case, the
309 repression was at the transcriptional level (Figure 4 – figure supplement 1 I-J').
310 Inversely, long linker Antp isoforms exhibited stronger activation of Antp reporter, as
311 compared to short linker ones (Figure 4 C, C', G, G' and quantified in D and H, see
312 also Materials and Methods). We, additionally, validated that short linker isoforms
313 encoded by full-length or SynthAntp cDNAs behaved as weaker auto-activating and
314 stronger auto-repressing Antp species in all our previous experiments of
315 endogenous Antp protein and P1 reporter (Figure 4 – figure supplement 1 A-H'). We
316 conclude that, also in the case of Antp auto-regulation, short linker isoforms function
317 as more potent repressors, whereas long linker ones operate as more potent
318 activators.

319 Since the Antp P1 promoter unit changes its configuration from preferential
320 auto-activation to auto-repression, and short and long linker Antp isoforms function
321 as preferential auto-repressors and auto-activators, it appeared possible that the
322 switch in Antp regulation is executed at the level of transcript variant abundance of
323 these isoforms. Therefore, we next quantified the relative abundance of long and
324 short linker transcript variants in the embryo, second and third instar discs (Figure 4
325 D and H). We found that the concentration of the long linker variant decreased,
326 whereas the concentration of the short linker variant increased over time in
327 development, in line with previous observations (Stroeher et al., 1988). As

hypothesized, this finding suggested that relative transcript variant abundance may underlie the switch between auto-activation and auto-repression (without excluding additional mechanisms).

Relative changes in Antp transcript variant concentration (Figure 4 D and H), differential efficiency of their encoding isoforms to repress or activate the *Antp* gene (Figure 4 B-D and F-H), the developmental switch of the *Antp* gene from auto-activation to repression (Figure 3) and the different mobilities of Antp between second and third instar imaginal discs (Figure 3 E) all pointed towards the hypothesis that the two isoforms have different properties in their modes of interaction with chromatin. To investigate this, we expressed the two isoforms in third instar wing and antennal discs from the *69B* enhancer, which we established to result in Antp concentrations close to (if not below) endogenous levels (Figure 2 – figure supplement 2 A-J). FCS measurements revealed that the short linker isoform displayed longer characteristic decay times and higher fraction of DNA-bound molecules, suggesting stronger and more pronounced binding to chromatin than its long linker counterpart (Figure 4 D and H and Figure 4 – figure supplement 2 A-B). With chromatin (and therefore Antp binding sites configuration) being identical between the two instances (short and long linker isoforms examined in third instar wing and antennal imaginal discs of the same age), we were able to directly compare the apparent equilibrium dissociation constants for the two isoforms (Supplement 3). We found that the affinity of binding to chromatin ($K_d{}^{-1}$) of the repressing short linker isoform is at least 2.3 times higher compared to the activating long linker isoform ($\frac{K_{d,Antp}^{long\ linker\ isof.}}{K_{d,Antp}^{short\ linker\ isof.}} > 2.3$) (Figure 4 D and H and Figure 4 – figure supplement 2 C-D'). We, additionally, validated the different affinities of short and long isoforms by gel-shift experiments using different Antp binding sequences and

obtained from two- to eightfold higher affinity of the short linker isoform compared to the long linker isoform in binding of previously characterized Antp and homeodomain binding sites (Figure 4 D and H and Figure 4 – figure supplement 3). Collectively, our experiments support the notion that differences in Antp regulation during disc development can be largely attributed to differences in the affinity of the investigated Antp isoforms.

Taken together, the switch of Antp from an auto-activating to an auto-repressing state and the alteration of its DNA-binding behavior during disc development can be largely explained by a temporal developmental regulation of the relative concentrations of preferentially auto-activating and auto-repressing Antp protein isoforms, which themselves display distinct properties in their modes of interaction with chromatin (Figure 4 E and I).

Robustness of Antp auto-regulation

In order to further substantiate the qualitative model of Antp auto-regulation suggested by our experimental findings, we developed a mathematical model of stochastic *Antp* expression. This model tests whether the identified interplay between positive and negative auto-regulation of Antp through distinct isoforms is sufficient to explain the increase in protein concentration and decrease in nucleus-to-nucleus variability from early to late stages. The model consists of a dynamic promoter, which drives transcription of *Antp* followed by a splicing step, leading to the expression of either the auto-repressing or the auto-activating isoform of Antp. In line with our finding that the repressing isoform has higher concentration at later stages, we assumed that splicing is more likely to generate this isoform than the activating isoform. The initial imbalance of Antp towards the activating isoform

(Figure 4 D and H) is modeled through appropriate initial concentrations of each isoform.

Since Antp copy numbers per nucleus are in the thousands at both early and late stages, intrinsic noise of gene expression is likely to explain only a certain portion of the overall variability in Antp concentrations (Elowitz et al., 2002; Taniguchi et al., 2010). The remaining part (termed extrinsic variability) is due to cell-to-cell differences in certain factors affecting gene expression such as the ribosomal or ATP abundances. To check whether extrinsic variability significantly affects Antp expression, we expressed nuclear RFP constitutively, alongside with endogenous Antp and measured the abundances of green-labeled Antp and RFP. Since extrinsic factors are expected to affect both genes in a similar way, one should observe a correlation between the concentration of nuclear RFP and Antp-eGFP. Our data showed a statistically significant correlation between RFP and Antp (Figure 5 – figure supplement 1, $r = 0.524$ and $p = 9.77 \cdot 10^{-5}$). Correspondingly, we accounted for extrinsic variability also in our model by allowing gene expression rates to randomly vary between cells (Zechner et al., 2012).

The promoter itself is modeled as a Markov chain with three distinct transcriptional states. In the absence of Antp, the promoter is inactive and transcription cannot take place (state “U” in Figure 5 A). From there, the promoter can switch into a highly expressing state “A” at a rate that is assumed to be proportional to the concentration of the long-linker, auto-activating isoform. This resembles the positive auto-regulatory function of Antp. Conversely, the promoter can be repressed by recruitment of the short-linker, auto-repressing isoform, corresponding to state “R” in the model (Figure 5 A). To account for potential leakiness of the promoter, this rate is not assumed to be zero, but significantly lower

than that of state “A”. Since the auto-repressing isoform of Antp can also activate the promoter, albeit significantly weaker than the auto-activating isoform, and vice versa, we allow the promoter to switch between states “A” and “R”.

While this promoter model resembles the dual-feedback structure of *Antp* locus inferred from experiments, it is unclear whether the two isoforms compete for the same binding sites on the P1 promoter or if auto-repression can take place regardless of whether an activating isoform is already bound to the promoter. In the former case, an increase in concentration of repressing Antp species enhances the probability to reach state “R” only if the promoter is in state “U” (Figure 5 B and B’’). In the latter case, also the rate of switching between “A” and “R” depends on the concentration of repressing isoforms of Antp (Figure 5 A-A’’). We analyzed both model variants by forward simulation and found that both of them can explain the increase in average Antp concentration between early and late stages (Figure 5 A’’ and B’’), as well as the relative fraction of repressing and activating isoforms (Figure 5 D and D’). However, only the non-competitive binding model (Figure 5 A) can explain the substantial reduction of total Antp variability between early and late stages (Figure 5 A’), whereas in the competitive model variability is not reduced (Figure 5 B’). We additionally established that the negative feedback is required for suppression of variability (Figure 5 C-C’’), since without this, no suppression of variability is conferred (Figure 5 C’). Thus, our model suggested that auto-repression is required and it is possible also if an activating isoform of Antp is already bound to the P1 promoter. Correspondingly, we use the non-competitive promoter model for further analyses.

To further validate our model, we first examined its predictions on variability by comparing the variability values predicted by the model to the ones generated by

our experimental measurements. Next to the CV^2, the Fano factor (expressed as the variance over the mean, $FF = \frac{s^2}{m}$, in concentration units) is another commonly used index to quantify variability in biological systems. Fano factor values that increase with average concentrations indicate that the underlying transcriptional processes cannot be sufficiently explained by a simple one-step promoter configuration with purely intrinsic Poissonian noise and that extrinsic noise is likely to contribute significantly to the overall variability (Newman et al., 2006; Schwanhausser et al., 2011; Taniguchi et al., 2010). Our model predicted a decrease in variability as a function of total Antp concentration and an increase in the Fano factor. These findings are in good agreement with our experimental data (compare Figure 5 E to E' and F to F').

We next analyzed the model behavior under different genetic perturbations. We found that overexpression of both auto-activating and auto-repressing isoforms leads to an increase of the total Antp concentration (Figure 5 G' and H'), but there is no negative effect on the noise suppressing property of the circuit (Figure 5 G and H). In fact, the variability is even further decreased, which can be explained by the characteristic inverse relation between intrinsic noise and average concentration (Paulsson, 2004). In line with this prediction, flies expressing roughly eightfold concentration of either SynthAntp auto-activating or auto-repressing isoform in distal appendages (Figure 5 I and J, Figure 2 – figure supplement 2 A and I) or the notum (Figure 5 K and Figure 5 – figure supplement 2 A and A') displayed the wild type morphology, indicative of normal Antp function.

However, overexpression of an exogenous repressor, such as Sex combs reduced (Scr), which can only repress Antp at the transcriptional level, but can neither activate it nor activate its own transcription (Figure 5 – figure supplement 2 B-

G'), was predicted by the model to block transcription almost entirely and to have correspondingly severe effects on Antp dynamics (Figure 5 – figure L and L'), leading to high variability even at late stages and to very low expression levels. As expected, flies overexpressing SynthScr in the distal appendages or the notum, displayed severe malformations of both leg and notum development (Figure 5 M-O).

Taken together, the minimal model of Antp auto-regulatory genetic circuit is able to explain the experimentally observed differences in Antp concentration and cell-to-cell variability at early and late developmental stages.

Discussion

In this work, we have characterized the endogenous molecular numbers (concentration) and cell-to-cell variability in concentration of 14 TFs in *Drosophila* imaginal discs by FCS. We have identified Antp as a TF displaying, for its high average concentrations, considerably lower variability among cells. We used a combination of genetics, FCS and mathematical modeling to quantitatively characterize Antp behavior in live imaginal discs and identified a kinetic mechanism responsible for the suppression of variability in third instar discs compared to earlier developmental stages. We found that *Antp* can auto-regulate its expression levels during the course of development, starting from a preferentially auto-activating state early in development and transitioning to a preferentially auto-repressing state later. The early state is characterized by lower average Antp concentrations and high variability, whereas the opposite is true for the later repressing state. Without excluding other mechanisms, such as chromatin configuration and accessibility of Hox binding sites to Antp, we showed that differential expression of Antp isoforms is one contributing mechanism for the observed regulatory switch. These isoforms

478 have preferentially activating or repressing activities on the Antp promoter, bind
479 chromatin with different affinities and are themselves expressed in different relative
480 amounts during development. Finally, based on this data, we have derived a simple
481 kinetic model of *Antp* auto-regulation and confirmed its predictions by introducing
482 genetic perturbations.

483 Negative auto-regulation has been identified as a frequently deployed
484 mechanism for the reduction of noise (cell-to-cell variability) and the increase of
485 regulatory robustness in various systems (Becskei and Serrano, 2000; Dublanche et
486 al., 2006; Gronlund et al., 2013; Nevozhay et al., 2009; Shimoga et al., 2013; Thattai
487 and van Oudenaarden, 2001). Auto-repression has been described for the Hox gene
488 *Ultrabithorax* (*Ubx*) in haltere specification and as a mechanism of controlling Ubx
489 levels against genetic variation (Crickmore et al., 2009; Garaulet et al., 2008), as well
490 as in *Ubx* promoter regulation in Drosophila S2 cells (Krasnow et al., 1989). In
491 contrast, an auto-activating mechanism is responsible for the maintenance of
492 *Deformed* expression in the embryo (Kuziora and McGinnis, 1988). Moreover, global
493 auto-regulation of *Hox* gene complexes has been shown to be in effect also in
494 mammalian limb development (Sheth et al., 2014). These experiments point to
495 evolutionarily conserved mechanisms for establishing (auto-activation) or limiting
496 (auto-repression) Hox TF levels and variability in different developmental contexts.

497 Our data suggest that the developmental switch from auto-activation to auto-
498 repression is, at least in part, mediated by molecularly distinct Antp linker isoforms.
499 Differences in affinities of different Hox TF isoforms, based on their linker between
500 the YPWM motif and the homeodomain, have also been identified for the Hox TF
501 Ubx. Interestingly, its linker is also subject to alternative splicing at the RNA level
502 (Reed et al., 2010). In a similar way to Antp, the long linker Ubx isoform displays 4-

503 5fold lower affinity of DNA binding, as compared to short linker isoforms, and the two
504 isoforms are not functionally interchangeable in *in vivo* assays. Finally, the Ubx linker
505 also affects the strength of its interaction with the Hox cofactor Extradenticle (Exd),
506 underscoring the functional importance of linker length in Hox TF function (Saadaoui
507 et al., 2011). Thus, protein isoform control might represent a common regulatory
508 mechanism of Hox-mediated transcriptional regulation.

509 Our model predicted that the Antp auto-regulatory circuit is robust with respect
510 to initial conditions and extrinsic noise by being able to suppress cell-to-cell
511 concentration variability even at very high concentrations of the auto-repressing or
512 the auto-activating Antp isoform. This “buffering” capacity on cell-to-cell variability is
513 reflected in the ability of flies to tolerate up to 7-fold overexpression of Antp without
514 exhibiting abnormal phenotypes. Therefore, two different isoforms produced from the
515 same gene with opposing roles in transcriptional regulation and different auto-
516 regulatory binding sites on the gene’s promoter seem to suffice to create a robust
517 gene expression circuit that is able to “buffer” perturbations of the starting conditions.
518 So far, we have only been able to indiscriminately increase or decrease Antp
519 concentration at the tissue level and record the phenotypic outcome of these
520 perturbations. It will be interesting to test whether controlled perturbations of TF
521 variability at the tissue level (making TF concentration patterns less or more noisy
522 among neighboring cells) lead to abnormal phenotypes, however the technology for
523 such manipulation is currently not readily accessible in flies.

524 While our study has focused on the quantitative analysis of the influence of
525 Antp on its own expression, it may also have important implications for the regulation
526 of Antp target genes. In particular, the repression and activation of genes through
527 different isoforms of the same TF represents a plausible design principle to achieve

528 differential expression of target genes. This could be achieved either through
529 temporal developmental control of isoform abundance, or by spatial control, for
530 example through the formation of different nuclear microenvironments.

531 In the case of temporal control, since target genes harbor different amounts of
532 binding sites for activating and repressing isoforms, transcriptional programs of cells
533 could be easily switched by changes in relative concentration of TF isoforms. In the
534 case of Antp, for instance, targets that allow binding of only the short-linker,
535 repressing isoform, could be highly expressed initially, but expression would be shut
536 down at later stages as soon as this isoform becomes dominant. Conversely, the
537 opposite behavior would be observed for targets featuring binding sites for only the
538 activating isoform. We previously established that Antp target genes are activated or
539 repressed with different efficiencies by Antp isoforms (Papadopoulos et al., 2011).
540 Such a mechanism would allow distinct sets of target genes to be differentially
541 regulated by the same Hox TF at different developmental stages. Evidence from
542 genome-wide investigation of Hox target sites in the wing disc during development
543 (third instar larval, prepupal and pupal wing discs) has shown that target gene
544 batteries change dramatically in development (Pavlopoulos and Akam, 2011).

545 In the case of spatial control, enhancer binding sites of similar affinity could
546 cluster in topologically distinct regions in the nucleus, according to the highest
547 concentrations of either the preferentially activating or the repressing Antp isoform,
548 thus creating microenvironments, capable of favoring transcriptional activation or
549 repression. In this case, developmental control of the abundances of these two
550 isoforms would change the efficiencies of activation and repression of their targets
551 by enrichment or shrinkage of the microenvironments and/or departure/arrival of
552 enhancers to pre-existing microenvironments. We have already observed that Antp

553 nuclear distribution is not even, but features sites of accumulation (Figure 5 – figure
554 supplement 1 B). While this scenario remains to be examined in detail for Antp,
555 recent work on the Ubx-dependent expression of the *shavenbaby* (*svb*) gene
556 identified that this mechanism of generation of functionally distinct nuclear
557 microenvironments not only exists, but also allows robust expression of the *svb* locus
558 from low-affinity enhancers (Crocker et al., 2015; Crocker et al., 2016; Crocker et al.,
559 2017).

560 In general, while this work has increased our understanding of how
561 developmentally important TFs secure their own regulatory robustness, it will be
562 interesting to investigate whether the design principles of auto-regulatory circuits
563 extend also to target genes.

564

565 ## Figure legends

566 Figure 1: **Study of concentration, DNA-binding dynamics and cell-to-cell**
567 **protein concentration variability of 14 Drosophila TFs in imaginal discs.** (A-H)
568 Workflow of the study of TF concentration, mobility/DNA-binding and nucleus-to-
569 nucleus variability of TFs in imaginal discs by FCS. Live imaging of imaginal discs,
570 expressing endogenously-tagged TFs, visualized by fluorescence microscopy and
571 neighboring cells, expressing TFs at different levels, selected for FCS
572 measurements (A-B). FCS measurements are performed by placing the focal point
573 of the laser light into the nucleus (C-D) and recording fluorescence intensity
574 fluctuations (E), generated by the increase or decrease of the fluorescence intensity,
575 caused by the arrival or departure of fast- and slowly-diffusing TF molecules into or
576 out of the confocal detection volume (D). The recorded fluctuations are subjected to
577 temporal autocorrelation analysis, which generates temporal autocorrelation curves

(henceforth referred to as FCS curves), which by fitting with an appropriate model (Supplement 1), yield information about the absolute concentration of fluorescent molecules (F) and, after normalization to the same amplitude, their corresponding diffusion times, as well as the fraction of fast- and slowly-diffusing TF molecules (G). The concentration of molecules is inversely proportional to the y-axis amplitude at the origin of the FCS curve (F). Processes that slow down the diffusion of TF molecules, such as binding to very large molecules (e.g. chromosomal DNA), are visible by a shift of the FCS curves to longer characteristic times (G). Measurements in a collection of neighboring cell nuclei also allow the calculation of protein concentration variability at the live tissue level (H). (I) Representative average FCS measurements of eight TFs, selected to demonstrate the full span of the concentration range observed. (J) FCS curves shown in (I), normalized to the same amplitude, $G_n(\tau) = 1$ at $\tau = 10\ \mu s$, show the shift of the characteristic decay times to higher values and the increase of the relative amplitude of the slow component, indicating slower diffusion and/or higher degree of TF binding to the DNA. (K) Variability of the 14 TFs as a function of concentration. Antp in the wing, but even more in the leg, disc displays markedly lower variability for its average concentrations. (L) Variability in concentration of endogenous Antp in the wing disc, observed among clusters of neighboring cells, each displaying a different average concentration. (M) Variability of Antp concentration in clusters of neighboring cell nuclei (plotted as a function of its average concentrations), decreases as the average Antp concentration in the cluster increases, i.e. low average concentration clusters are associated with high variability, whereas high average concentration clusters exhibit low variability. Error bars in (K) and (N) represent 1 standard deviation of average TF concentration.

Figure 1 – figure supplement 1: **Measurement of average concentrations and nucleus-to-nucleus variability of 14 endogenously-tagged TFs in Drosophila imaginal discs by FCS.** (A-P) Fluorescence imaging of TFs, showing their expression pattern in imaginal discs and the salivary gland. White arrows indicate regions where FCS measurements of endogenous intra-nuclear concentration were performed and the average concentrations are given for each TF. Images have been contrasted for visualization purposes. For the Antp and Grn TFs, both leg and wing imaginal discs have been used for measurements. Average concentrations of TFs measured in different cells span a range of two orders of magnitude, from few tens to a thousand nanomolar. Scale bars denote $100\,\mu m$, unless otherwise indicated. (Q) Characterization of nucleus-to-nucleus variability among neighboring cells within the same expression domain in imaginal discs of the 14 TF studied by FCS. Black bars show concentration averages (with error bars representing 1 standard deviation), whereas grey bars show the variability, i.e. the squared coefficient of variability (expressed as the variance over the squared mean, $CV^2 = \frac{s^2}{m^2}$). TFs have been sorted according to increasing variability.

Figure 1 – figure supplement 2: **Characteristic decay times of Antp-eGFP do not change as a function of total concentration.** (A-B) Characteristic decay times τ_{D_1} (A) and τ_{D_2} (B) do not vary with the concentration of Antp-eGFP TF molecules, as evident from $\tau_{D_1} = f(N_1)$ and $\tau_{D_2} = f(N_2)$, where N_1 is the number of freely diffusing, N_2 the number of bound Antp-eGFP TF molecules and τ_{D_1}, τ_{D_2} their respective diffusion times.

628 Figure 2: **Antp is able to repress and activate its own expression at the**
629 **transcriptional level.** (A) Schematic representation of the wing disc showing the
630 region of highest Antp expression (green cells). Antp is highly expressed in the wing
631 disc in the regions of the notum that correspond to the structure of the prescutum in
632 the adult cuticle, as well as in the base of the wing blade, which gives rise to the
633 mesopleura and pteropleura of the adult thoracic cuticle. The black rectangle
634 indicates the approximate region where the clonal analysis has been performed in
635 (B-C'). (B-B') Clonal overexpression of a *SynthAntp-eGFP* construct (green) in the
636 wing disc represses the endogenous Antp protein (magenta). The region enclosed
637 by a dashed line in (B) shows a clone induced in the notum within the *Antp*
638 expression domain. (C-C') Auto-repression of Antp occurs at the transcriptional level.
639 Induction of *SynthAntp-eGFP*-overexpressing clones, while monitoring *Antp*
640 transcription by the *Antp* P1-*lacZ* reporter. Dashed lines indicate clones within the
641 *Antp* P1 reporter expression domain that express *SynthAntp-eGFP* and down-
642 regulate *Antp* P1-*lacZ*. (D) Schematic representation of Antp repressive function on
643 its own transcription. (E) Schematic representation of the wing disc. The black
644 rectangle indicates the approximate region of ectopic Antp P1 reporter expression in
645 (F-F'). (F-F') Expression of *SynthAntp-eGFP* by *Dll*-Gal4 (MD23) results in ectopic
646 activation of *Antp* P1-*lacZ* in distal compartments of the wing disc. Note the
647 endogenous and ectopic expression pattern of the reporter in (F), indicated by white
648 arrows. (G) Schematic representation of Antp activating function on its own
649 transcription. Scale bars denote $100\ \mu m$.
650
651 Figure 2 – figure supplement 1: **Antp is able to repress and activate itself at the**
652 **transcriptional level – controls.** (A-C') Normal expression patterns of the Antp P1

(A-A') and P2 (B-B') transcriptional reporters and Antp protein immunohistochemistry (C-C'). Boxed areas in (A), (B) and (C) are magnified in (A'), (B') and (C'). The Antp P1 reporter is highly expressed in the prescutum region of the notum (A') and the peripodial cells at the base of the wing blade (giving rise to the mesopleura and pteropleura of the thorax, white arrows in (A)), which overlaps with the Antp protein pattern ((C') and arrows in (C)). The Antp P2 promoter reporter construct exhibits very weak, if any, expression at these two domains (B-B'). (D-E') Negative controls of Antp protein (D-D') and P1 reporter transcription (E-E') upon overexpression of eGFP. Dashed lines outline the regions of clonal induction in (D) and (E), where neither the Antp protein (D) nor the Antp P1 reporter (E) are repressed. (F-F') Repression of Antp P1 reporter transcription upon clonal overexpression of the full-length untagged Antp protein (Antp-FL). The ectopic expression domain is outlined by white dashed lines in (F) and marked by the expression of eGFP (F'). (G-G') Activation of Antp P1 reporter transcription upon ectopic expression of untagged Antp full-length (Antp-FL) with *Dll* (MD23) driver in the distal region of wing pouch. The ectopic expression domain is outlined by a yellow dashed line in (G) and is marked by the expression of nuclear mRFP1. (H-H') Negative control of ectopic activation of Antp P1 transcription upon overexpression of nuclear mRFP1 alone by *Dll* (MD23)-Gal4. Scale bars denote $100\ \mu m$.

Figure 2 – figure supplement 2: **Direct correlation between Antp concentration and homeotic function – Antp auto-repression and activation occurs at endogenous concentrations.** (A-D) Live imaging (one optical section) of SynthAntp-eGFP expressed in the distal antennal portion of the eye-antennal disc by different Gal4 drivers. The concentration was measured using FCS and average

678 concentrations are indicated. An eightfold difference was observed between the
679 strong *Dll*-Gal4 driver (MD23) (A) and weak *69B*-Gal4 driver (D). (E-H)
680 Transformations of the distal antenna into a tarsus in adult flies, caused by
681 *SynthAntp-eGFP* overexpression in antennal discs (A-D). The strength of the
682 transformation correlates with the level of expression from the different Gal4 drivers.
683 Ectopic tarsi range from complete transformation to milder transformations of the
684 arista or ectopic leg bristles in the third antennal segment in (G) and (H), indicated by
685 black arrows. (I) Average FCS measurements performed in nuclei overexpressing
686 *SynthAntp-eGFP*, using different Gal4 drivers. Note that the y-axis amplitudes at the
687 origin of the FCS curves are inversely proportional to the concentration. (J) FCS
688 curves of measurements in (I) normalized to the same amplitude, $G_n(\tau) = 1$ at
689 $\tau = 10\ \mu s$, show major overlap, indicating indistinguishable behavior of Antp binding
690 to chromatin across the concentration range examined $(0.5 - 3.8\ nM)$. (K-P) Antp
691 auto-regulation occurs at endogenous concentrations. (K-L) Repression of
692 endogenous Antp protein upon induction of *SynthAntp-eGFP* in the proximal regions
693 of the wing disc by *69B*-Gal4, which results in Antp expression very similar to
694 endogenous levels. (M-N) No repression is observed upon overexpression of *eGFP*
695 (negative control), as indicated by white arrows in (M). White arrows in (K) and (M)
696 point to the equivalent area in the wing disc, where Antp repression is observed. (O)
697 X-gal stainings of the *Antp* P1 reporter show weak but detectable ectopic β-
698 galactosidase activity in the antennal disc (black arrows). (P) Negative control
699 stainings of eGFP induced by the *69B* enhancer show complete absence of ectopic
700 reporter transcription. Scale bars denote $100\ \mu m$, unless otherwise indicated.
701

Figure 2 – figure supplement 3: **Comparison of endogenous and overexpressed Antp by FCS.** (A) FCS curves of Antp-eGFP in wing disc nuclei. Concentration differences of fluorescent Antp protein are obvious among cells expressing one or two copies of Antp-eGFP (homozygous and heterozygous larvae) or overexpressing SynthAntp-eGFP from the *Dll* MD23)-Gal4 driver. (B) FCS curves shown in (A) normalized to the same amplitude, $G_n(\tau) = 1$ at $\tau = 10\,\mu s$, show pronounced overlap between homozygous and heterozygous *Antp-eGFP*-expressing cells, as well as between endogenously expressed *Antp* and overexpressed *SynthAntp-eGFP*, indicating similar diffusion times and modes of interaction with chromatin. FCS curves are color-coded as outlined in panel (B).

Figure 3: **Antp is necessary and sufficient to trigger a developmental switch from transcriptional auto-activation to auto-repression.** (A and F) Schematic representations of the experimental setup. Clones were induced at 26 h (early clones) or 60 h (late clones). The analysis was performed at third instar larval stage (~96-120 h of development). Black rectangles enclose the blown up regions of interest in the corresponding data panels. (B-B') Early-induced clones, expressing full-length, untagged *Antp*, marked by the absence of mCherry, reveal strong auto-activation of Antp-eGFP (dashed lines in (B)), monitored by the endogenous Antp-eGFP protein. The cyan line in (B) outlines the region of highest endogenous Antp expression. Note the absence of repression of the endogenous gene in overexpression clones within this region at this stage. The whole *Antp* expression domain expresses *Antp-eGFP*, but overexpression clones (sub-regions marked by absence of mCherry staining) express *Antp-eGFP* much stronger (B'). (C-C') Antp is required for sustaining its own expression by auto-activation. Induction of *RNAi*

727 knockdown clones of *Antp* at 26 h of development (early clonal induction, dashed
728 line in (C)) results in cells with pronounced reduction in *Antp* P1 reporter expression.
729 Knockdown clones have been marked by nuclear mRFP1 in (C'). (D) Updated Antp
730 auto-activation model showing the pronounced auto-activating capacity of Antp at
731 early stages, without excluding concurrent weak auto-repression. (E) Study of
732 concentration, DNA-binding and nucleus-to-nucleus variability by FCS at second
733 instar leg and wing discs (derived by the FCS analysis in Figure 3 – figure
734 supplement 3). Low concentration, short decay times (indicative of low degree of
735 DNA-binding) and high variability were observed in second instar wing and leg discs.
736 Reciprocally, high concentration, long decay times (indicative of pronounced
737 chromatin binding) and low variability were observed in third instar wing and leg
738 discs. Statistical significance was determined using a two-tailed Student's T-test (***,
739 $p < 0.001$ and *, $p < 0.05$, namely $p_{concentration}^{2nd\ vs\ 3rd\ instar} = 2.04 \cdot 10^{-20}$, $p_{\tau D2}^{2nd\ vs\ 3rd\ instar} =$
740 $7.2 \cdot 10^{-4}$ and $p_{variation}^{2nd\ vs\ 3rd\ instar} = 3.4 \cdot 10^{-2}$). (G-G') Late-induced clones, expressing
741 full-length, untagged *Antp*, marked by the absence of mCherry, reveal strong auto-
742 repression of Antp-eGFP (dashed lines in (G)), monitored by the endogenous Antp-
743 eGFP protein. The cyan lines in (G) outline the region of strong endogenous
744 expression. (H-H') Late induction of *Antp* knockdown clones by *RNAi* (60 h of
745 development) within its normal expression domain results in upregulation of the *Antp*
746 P1 reporter above endogenous levels (dashed line in (H)). The cyan line in (H)
747 outlines the region of strong endogenous expression of the P1 reporter. Cytoplasmic
748 eGFP marks the clone of *Antp* knockdown by *RNAi* (H'). (I) Updated Antp auto-
749 repression model showing the pronounced auto-repressing capacity of Antp at late
750 stages, without excluding concurrent weak auto-activation.
751

Figure 3 – figure supplement 1: **Antp expression patterns are not altered by the MiMIC MI02272 insertion.** (A) Schematic representation of the Antp-eGFP fusion protein produced by the conversion of the MiMIC MI02272 construct to an artificial exon. The eGFP-encoding artificial exon is situated in intron 6 of the mRNA and is spliced in between exons 6 and 7 that correspond to the long and non-conserved N-terminal coding sequence of the protein, which has little (if any) function *in vivo* (Papadopoulos et al., 2011), and does not disrupt the homeodomain or YPWM motif. All features have been drawn to scale. (B) Heterozygous flies (embryos and third instar larvae), examined for their Antp-eGFP pattern (detected by an antibody to GFP, green), as compared to the total amount of Antp (expressed by the sum of the MiMIC *Antp-eGFP* and the wild type *Antp* loci), detected by an Antp antibody (magenta). Comparisons of the Antp pattern in wild type embryos and all thoracic imaginal discs are provided case-wise in the right panel. In discs, dashed lines approximately separate the anterior (indicated by "A") from the posterior (indicated by "P") domain of the disc. Note the high expression of Antp in the humeral disc. In the leg discs, Antp is expressed most strongly in the posterior compartment of the prothoracic leg disc, the anterior compartment of the mesothoracic leg disc and in an abundant pattern in the metathoracic leg disc. Cyan arrows point to Antp positive cells in the second and third leg discs that are centrally located, as previously shown (Engstrom et al., 1992). All images represent Z-projections. Scale bars denote $100\ \mu m$.

Figure 3 – figure supplement 2: **Antp is sufficient and required to trigger a developmental switch from transcriptional auto-activation to auto-repression – controls.** (A-C') Negative controls of Antp clonal auto-activation and repression

using early and late clone induction regimes. (A-A') Without induction of clones expressing full-length untagged Antp, no repression or activation of endogenous Antp protein is observed. (B-C') Upon induction of non-overexpressing clones (clones expressing only Gal4, without a UAS transgene), no activation or repression of Antp protein is observed at early or late induction time points. White dashed lines in (B) and (C) outline the induced clones, marked by the absence of mCherry. (D-E') Early ectopic induction of either Antp full-length untagged protein (D-D') or SynthAntp (E-E') result in upregulation of the Antp P1 reporter. Yellow dashed lines in (D) and arrows in (E) point to the induced clones and cyan continuous lines show the regions of high endogenous expression of the reporter. Clones have been marked by cytoplasmic eGFP. (F-G') Negative controls of early clonal induction of eGFP alone (without concurrent induction of Antp) show no repression of the Antp protein (F-F') or the P1 reporter (G-G'). Dashed lines in (G) mark the clones of eGFP induction. (H-H') Positive control of clonal knockdown of the Antp *RNAi* line used in Figure 3. Clonal knockdown by *RNAi* (indicated by the dashed line in (H) and marked by nuclear mRFP1 in (H')) resulted in efficient downregulation of the endogenous Antp protein. Scale bars denote $100\ \mu m$, unless otherwise indicated.

Figure 3 – figure supplement 3: **Antp concentration and cell-to-cell variability in second and third instar wing and leg imaginal discs** (A-A'') Representative FCS curves recorded in second and third instar wing and leg imaginal discs, expressing *Antp-eGFP*. Note the low concentration in second instar leg and wing discs, reflected by the relatively high amplitude of the FCS curves (inversely proportional to concentration) in (A), as compared to the high concentration in third instar discs in (A'). (B) FCS curves shown in (A) and (A'), normalized to the same amplitude,

802 $G_n(\tau) = 1$ at $\tau = 10\ \mu s$, show a shift towards longer decay times in the third instar
803 leg and wing discs, indicative of pronounced interactions of Antp with chromatin.
804 FCS curves are color-coded as outlined in panel (A). (C) Quantification of average
805 concentrations and cell-to-cell variability in protein concentration among neighboring
806 nuclei in wing and leg, second and third instar, discs. Black bars denote the average
807 concentration and grey bars denote the variability, expressed as the variance over
808 the squared mean. Note the increase in average concentration from second to third
809 instar (eleven-fold increase in the leg disc) and the concurrent drop in variability to
810 almost half of its value. Statistical significance was determined using Student's two-
811 tailed T-test (***, p<0.001, namely $p_{3rd-2nd\ instar\ leg} = 4.4 \cdot 10^{-18}$ and
812 $p_{3rd-2nd\ instar\ wing} = 3.2 \cdot 10^{-8}$).
813
814 Figure 4: **Developmental control of Antp auto-activation and auto-repression**
815 **relies on the relative concentrations of preferentially activating and repressing**
816 **Antp isoforms, which display different binding affinities to chromatin.** (A)
817 Schematic representation of the Antp mRNA, generated from the P1 promoter, with
818 exons represented by grey boxes, the nucleotide length of which is indicated above
819 each exon in base pairs (bp). A higher magnification of exons 4-7 (omitting their in-
820 between splicing points for simplicity) indicates an alternative splice site at the 3' end
821 of exon 7, which results in an isoform featuring a short linker between the YPWM
822 motif and the homeodomain (encoded by four amino acids: RSQF, grey box), or a
823 long linker isoform (encoded by eight amino acids: RSQFGKCQ, white box). All
824 exons have been drawn to scale. (B-B') *SynthAntp-eGFP* transgenes encoding Antp
825 isoforms with a long linker were induced from the *ptc* enhancer and endogenous
826 Antp protein auto-repression was monitored at the proximal portion of the wing disc.

827 A white dashed line outlines the region of auto-repression that was used for
828 quantification (see Materials and Methods). The long linker isoform (preferentially
829 auto-activating isoform) acts as a weak repressor of Antp protein, as compared to its
830 short linker equivalent in (F-F'). (C-C') *SynthAntp-eGFP* transgenes encoding Antp
831 isoforms with a long linker were induced from the *Dll* (MD23) enhancer and Antp P1
832 reporter auto-activation was monitored at the distal portion of the wing disc (wing
833 blade), indicated by a yellow dashed line. The long linker isoform (preferential auto-
834 activator) induces stronger transcription of the P1 Antp reporter, as compared to its
835 short linker counterpart in (G-G'). (D) Relative concentration of long linker isoform
836 (see Materials and Methods); quantification of its auto-activation and auto-repression
837 capacities (see Materials and Methods); fraction of DNA-bound fluorescent
838 molecules, measured by FCS (see also Figure 4 – figure supplement 2); and relative
839 affinity of binding to the DNA (quantified by the calculation of its apparent equilibrium
840 dissociation constant using both FCS measurements and gel-shifts (EMSA), see
841 also Figure 4 – figure supplements 2 and 3) are provided for comparison with (H).
842 (E) Updated qualitative model of the dual auto-regulation of Antp by activating and
843 repressing Antp isoforms, equivalent to an early developmental stage. The activating
844 isoform binds with lower affinity to the P1 Antp promoter, but is produced in excess,
845 relative to the repressing one, resulting in preferential activation of transcription,
846 without cancelling out partial binding of the auto-repressive isoform as well. (F-F')
847 Similar to (B-B'), except induction has been with the short linker (preferentially auto-
848 repressing) isoform. It acts as a stronger repressor of Antp protein, as compared to
849 its long linker equivalent in (B-B'). (G-G') Similar to (C-C'), except induction has been
850 with the short linker (preferentially auto-repressing) isoform. It acts as a weaker
851 activator of Antp P1 transcription, as compared to its long linker equivalent in (C-C').

852 (H) The same parameters as in (D) have been evaluated and are provided for
853 comparison with (D). Statistical significance was determined using a two-tailed
854 Student's T-test between measurements performed with the long linker (auto-
855 activating) isoform in (D) and the short linker (auto-repressing) isoform in (H) (***,
856 $p < 0.001$ and *, $p < 0.05$, namely $p^{embryo\ long\ vs\ short}_{concentration} = 3.16 \cdot 10^{-5}$,
857 $p^{2nd\ instar\ long\ vs\ short}_{concentration} = 1.16 \cdot 10^{-4}$, $p^{3rd\ instar\ long\ vs\ short}_{concentration} = 2.85 \cdot 10^{-6}$,
858 $p^{long\ vs\ short}_{relative\ activation} = 4.1 \cdot 10^{-3}$, $p^{long\ vs\ short}_{relative\ repression} = 2.4 \cdot 10^{-4}$ and
859 $p^{long\ vs\ short}_{DNA-bound\ fraction\ (FCS)} = 5.6 \cdot 10^{-10}$). (I) Updated qualitative model representation of
860 Antp repression as in (E), whereby at later stages excess of Antp auto-repressor
861 accounts for negative feedback on transcriptional regulation of the P1 promoter,
862 without ruling out partial binding by the activating isoform as well, resulting in partial
863 activation of transcription, hence expression is maintained.
864
865 Figure 4 – supplement 1: **Developmental control of Antp auto-activation and**
866 **repression relies on the relative concentrations of preferentially auto-**
867 **activating and auto-repressing Antp isoforms, which display different binding**
868 **affinities to chromatin – short linker isoform controls.** (A-H') Experiments of
869 Figures 2-4, performed with short linker (preferentially auto-repressing) full-length
870 and SynthAntp isoforms on their capacity to repress and activate Antp P1 reporter
871 transcription and Antp protein. Dashed lines in all panels outline the clones induced
872 or the region of ectopic expression using *Dll* (MD23)-Gal4, whereas closed
873 continuous cyan lines outline the regions of endogenous Antp P1 reporter
874 expression in (G) and (H). (A-A') Repression of Antp protein by late clonal induction
875 of SynthAntp in the wing notum. (B-B') Equivalent assay as in (A-A'), but monitoring
876 auto-repression of the Antp P1 promoter transcription. (C-C') Similar assay to (B-B'),

using the full-length Antp protein, induced at the later time point. (D-D') Ectopic induction of full-length, short linker, untagged Antp cDNA with concurrent labeling of the expression domain by nuclear mRFP1 results in weak ectopic auto-activation of the Antp P1 reporter. (E-F') Early and late clonal induction of full-length, short linker, untagged Antp results in auto-repression (E-E'), or induction (F-F'), of the endogenous Antp protein, respectively. (G-H') Early clonal induction of SynthAntp (G-G') or the full-length cDNA (H-H'), both featuring a short linker, triggers ectopic activation of P1 promoter transcription. (I-J') Antp long (I-I') and short (J-J') linker isoforms repress Antp at the transcriptional level (monitored by Antp P1 reporter expression) when induced by *ptc*-Gal4 in the wing disc. Arrows point to the regions of auto-repressed Antp promoter. Scale bars denote $100\,\mu m$, unless otherwise indicated.

Figure 4 – figure supplement 2: **Comparative binding study of Antp short and long linker isoforms by FCS.** (A-B) FCS analysis performed on third instar wing and antennal imaginal discs, expressing short or long linker Antp isoforms (tagged to eGFP) close to endogenous concentrations, from the *69B*-enhancer. Cell nuclei of similar concentrations in the two datasets have been selected for analysis (A). Average FCS measurements on the short linker Antp isoform display a consistent shift towards longer decay times, as compared to its long linker counterpart (B), indicating higher degree of chromatin binding. (C-D') Binding study of short and long linker Antp isoforms in third instar wing and antennal discs, expressed by *69B*-Gal4. The concentration of the Antp short and long linker isoform DNA-bound complexes (derived by fitting the FCS curves in (A)) is plotted as a function of the total concentration of Antp-eGFP molecules. From the linear regression equations,

902 $y = 0.34x - 5.31$ (D') and $y = 0.24x - 3.28$ (E'), the ratio of apparent dissociation
903 constants for the long and short linker isoforms was calculated to be $\frac{K_{d,Antp}^{long\ linker\ isof.}}{K_{d,Antp}^{short\ linker\ isof.}} >$
904 2.3 (for the calculation refer to Supplement 3). The two dissociation constants differ
905 at least 2.3 times, indicating stronger binding of the short linker isoform to the DNA,
906 as compared to the long linker one.
907
908 Figure 4 – figure supplement 3: **In vitro binding study of Antp full-length long**
909 **and short linker isoforms to Antp and homeodomain binding sites by gel-shift**
910 **assays.** (A-D) Gel-shift experiments using purified full-length Antp protein, featuring
911 a long or a short linker, show from twofold (C) to eightfold (A) stronger binding of the
912 short linker isoform to Antp binding sites. The Antp-DNA complexes and the free
913 DNA-binding site are shown in (A) and are the same for (B-D). In (C) and (D) an
914 antibody to Antp has been used in the fifth lane of the serial dilutions of Antp protein
915 (black asterisks) to indicate specific Antp binding (super-shift). Equal starting
916 concentrations of purified Antp short and long linker protein have been used and
917 determined by Western blot. Each successive lane of long or short linker isoform
918 binding represents a twofold lower concentration of Antp protein. Triangles above the
919 concentration range of each sample denote declining concentrations and the black
920 areas therein indicate the corresponding concentration range at which Antp binding
921 to the probe has been observed.
922
923 Figure 5: **Mathematical model for stochastic Antp expression and system**
924 **perturbations.** (A-A'') A dynamic promoter, which drives transcription of *Antp*
925 followed by a splicing step, leads to either the repressing ("R" in (A)) or activating
926 ("A" in (A)) isoform of Antp. In the absence of Antp, the promoter is inactive and

transcription cannot take place ("U" in (A)). This promoter configuration leads to suppression of variability (A') and increase in Antp concentration (A''). (B-B'') Competition of Antp binding, whereby state "A" can be reached only through the unbound state "U" in (B), results in increase in Antp protein numbers (B'') without decrease in variability (cyan bar in (B')). (C-C'') Requirement of the negative feedback for suppression of variability. In the absence of the state "R" (C), concentration increases (C''), but variability also increases rather than being suppressed (cyan bar in (C')). (D-D') In all three models (A-A'', B-B'' and C-C''), changing relative concentrations of repressing and activating Antp isoforms are predicted, starting with excess of the activating isoform at early stages (D) and ending with excess of the repressing one at later stages (D'). (E-F') Model predictions (E and F) and experimental data validation (E' and F') of the decrease of variability (E) and the increase of the protein Fano factor (F) as a function of increasing Antp concentrations. (G-K) Perturbations of the model in (A-A'') by overexpression of Antp long linker (auto-activating) and short linker (auto-repressing) isoforms. (G-H') High concentration of both auto-repressing (G-G') and auto-activating (H-H') Antp isoforms result in increase of Antp protein copy numbers in (G') and (H') with concurrent repression of variability in (G) and (H), similar to the unperturbed system in (A-A''). (I-K) Overexpression of SynthAntp activating or repressing isoforms by *Dll* (MD23)-Gal4 in distal portion of appendages, such as the antenna and the leg imaginal discs, result in tarsal transformations in the antenna (where Antp is normally not expressed (I)), but normal development of tarsi in all legs (J). These flies are fully viable and can be maintained as a stock. Similarly normal is the development of the prescutum region of the notum, upon overexpression of SynthAntp activating or repressing isoforms by *MS243*-Gal4 (K). (L-O) Perturbations

of the model system in (A-A'') by overexpression of an exogenous Antp repressor. As expected, overexpression of the Hox transcription factor Scr, which is able to only repress, but neither activate Antp expression, nor its own (see Figure 5 – figure supplement 1 B-E' for details), is predicted to result in drastic reduction of Antp at later stages (cyan bar in (L')) and have barely any effect in Antp variability at these stages (L). In this case, ectopic expression of SynthScr by *Dll* (MD23)-Gal4 still triggers transformation of the antenna, which is devoid of Antp expression, into a tarsus (M), similar to induction of Antp in this tissue (I), but in overlapping domains with Antp normal expression, such as the distal leg portion, malformations of the tarsus and femur are observed (N). Overexpression of SynthScr transgenes by *MS243*-Gal4 in the fly notum results in severe malformations, indicated by developmental defects of the adult cuticle (O). Both fly genotypes in (N) and (O) die as pharate adults.

Figure 5 – figure supplement 1: **Investigation of extrinsic variability in the endogenous Antp-eGFP expression domain.** (A-B') Live imaging of a wing disc notum, where nuclear mRFP1 protein is highly expressed from a constitute enhancer (*ubi*-mRFP1(NLS)), alongside with endogenous Antp-eGFP. FCS measurements were performed in the region of high co-expression of Antp and RFP. (B-B') Higher magnification of cells as in (A-A'). Note the uneven distribution of Antp in the nuclei and the formation of sites of accumulation in (B). (C) Plot of the concentration of Antp-eGFP (expressed as number of fluorescent molecules in the Observation Volume Element (OVE)). The correlation coefficient r was calculated to be $r = 0.523$ and the p-value to be $p_{correlation} = 9.77 \cdot 10^{-5}$. Scale bars denote $100\,\mu m$, unless otherwise indicated.

Figure 5 – figure supplement 2: **Controls of Antp model predictions and Scr-mediated perturbations.** (A-A') *MS243*-Gal4-mediated expression of repressing or activating SynthAntp isoforms results in repression of the Antp endogenous protein in the notum region of the wing disc. (B-B') Ectopic expression of SynthScr in the wing disc using *ptc*-Gal4 results in drastic reduction of endogenous Antp protein levels. (C-C') Ectopic expression of SynthScr by *MS243*-Gal4 in the notum results in repression of the Antp protein. (D-D') SynthScr represses Antp at the transcriptional level, as indicated by the absence of transcription of the Antp P1 reporter (white arrows in (D)). (E-E') Unlike SynthAntp, SynthScr is not able to activate the Antp P1 promoter reporter transcription (E), when induced by *Dll* (MD23)-Gal4. (F-F') SynthScr is not able to downregulate its own endogenous protein levels upon overexpression by *Dll* (MD23)-Gal4. Dashed line in (F') outlines the region of high overlap between the overexpressed SynthScr and endogenous Scr stainings. (G-G') Negative control staining for the induction of eGFP in the wing disc notum by *MS243*-Gal4, which fails to repress endogenous Antp protein. Dashed lines in (A), (B) and (C) outline the regions of ectopic overexpression of SynthAntp or SynthScr, where endogenous Antp is repressed, whereas the dashed line in (F') outlines the region of overlap between SynthScr overexpression and endogenous expression of the Scr protein, where no repression is observed. Scale bars denote $100\ \mu m$, unless otherwise indicated.

Acknowledgements

We are deeply saddened by the unexpected passing of Prof. Walter J. Gehring, at the very inception of this work, when the project was still in the planning and preliminary data gathering stage. Prof. Gehring was an extraordinary human being and a scientific giant, whose work will continue to educate and inspire generations to come. The authors are indepted to Sonal Nagarkar Jaiswal, Paolo Mangahas, and Hugo J. Bellen for creating and sharing with us the Antp-eGFP line. DKP has been supported by a long-term fellowship from the Swiss National Science Foundation (PBBSP-138700) and a long-term fellowship from the Federation of European Biochemical Societies (FEBS) at initial stages of this project. VV has been supported by the Knut and Alice Wallenberg foundation and Karolinska Institute Research Funds. DKP would like to express his gratitude to PT for outstanding scientific, and uninterrupted financial, support. DKP is indebted to Markus Burkhardt, head of the imaging platform at the Center for Regenerative Therapies Dresden (CRTD), for help and discussions regarding FCS experiments in Dresden; Sylke Winkler and the DNA sequencing facility of the Max-Planck Institute of Molecular Cell Biology and Genetics (MPI-CBG) for providing assistance with Antp transcript variant quantification; Aliona Bogdanova and the Protein expression and purification facility of the MPI-CBG for purification of the repressing and activating Antp isoforms; as well as the Light Microscopy facility of MPI-CBG. DKP is also grateful to KS for numerous discussions and support throughout the implementation of this work and to Konstantinos Papadopoulos for advice on the mathematical analysis of the relative binding constants of repressing and activating Antp isoforms. The authors would like to acknowledge Jan Brugues and Thomas M. Schultheiss for their critical reading and insightful comments on the manuscript.

Materials and Methods

Fly stocks used

The Antp-eGFP MiMIC line has been a kind gift from Hugo J. Bellen. The *atonal* (VDRC ID 318959), *brinker* (VDRC ID 318246), *spalt major* (VDRC ID 318068), *yorkie* (VDRC ID 318237), *senseless* (VDRC ID 318017) and *Sex combs reduced* (VDRC ID 318441) fosmid lines are available from the Vienna Drosophila Resource Center (VDRC) and have been generated recently in our laboratory (Sarov et al., 2016). The *fork head* (stock 43951), *grainy head* (stock 42272), *Abdominal B* (stock 38625), *eyeless,* (stock 42271), *spineless* (transcript variant A, stock 42289), and *grain* (stock 58483) tagged BACs were generated by Rebecca Spokony and Kevin P. White and are available at the Bloomington Stock Center. For the *scalloped* gene, a GFP-trap line was used (Buszczak et al., 2007), a kind gift from Allan C. Spradling laboratory (line CA07575), with which genome-wide chromatin immunoprecipitation experiments have been performed (Slattery et al., 2013). For the *spineless* gene, Bloomington stock 42676, which tags isoforms C and D of the Spineless protein has been also tried in fluorescence imaging and FCS experiments, but did not yield detectable fluorescence in the antennal disc, rendering it inappropriate to be used in our analysis. Therefore, we resided to stock 42289, which tags the A isoform of the protein. For the *eyeless* gene, the FlyFos015860(pRedFlp-Hgr)(ey13630::2XTY1-SGFP-V5-preTEV-BLRP-3XFLAG)dFRT line (VDRC ID 318018) has been tried also in fluorescence imaging and FCS experiments, but did not yield detectable fluorescence in the eye disc for it to be used in our analysis. The *act5C*-FRT-yellow-FRT-Gal4 (Ay-Gal4) line used for clonal overexpression or *RNAi* knockdown has been described (Ito et al., 1997). The

UAS-Antp lines (synthetic and full-length), as well as UAS-SynthScr constructs have been previously described (Papadopoulos et al., 2011; Papadopoulos et al., 2010). The *Dll*-Gal4 (MD23) line has been a kind gift of Ginés Morata (Calleja et al., 1996). *69B*-Gal4 and *ptc*-Gal4 have been obtained from the Bloomington Stock Center. The *Antp* P1-*lacZ* and P2-*lacZ* have been previously described (Engstrom et al., 1992; Zink et al., 1991). The P1 reporter construct spans the region between 9.4 kb upstream of the P1 promoter transcription initiation site and 7.8 kb downstream into the first intron, including the first exon sequences and thus comprising 17.2 kb of Antp regulatory sequences (pAPT 1.8). The line used has been an insertion of the pAPT 1.8 vector bearing the P1 promoter regulatory sequences upstream of an *actin-lacZ* cytoplasmic reporter and has been inserted in cytogenetic location 99F on the right chromosomal arm of chromosome 3. The *Antp-RNAi* line has been from VDRC, line KK101774. UAS-eGFP stock was a kind gift of Konrad Basler. We are indebted to Sebastian Dunst for generating the *ubi*-FRT-mCherry(stop)-FRT-Gal4(VK37)/CyO line, which drives clonal overexpression upon flippase excision, while simultaneously marking cells by the loss of mCherry. For red-color labeling of clones the *act5C*-FRT-CD2-FRT-Gal4, UAS-mRFP1(NLS)/TM3 stock 30558 from the Bloomington Stock Center has been used. For marking the ectopic expression domain of untagged Antp proteins the UAS-mRFP1(NLS)/TM3 stock 31417 from the Bloomington Stock Center has been used. The *MS243*-Gal4; UAS-GFP/CyO line was a kind gift from the laboratory of Ernesto Sánchez-Herrero.

<u>Fly genotypes corresponding to fluorescence images</u>

Figure 1 – figure supplement 1 A: FlyFos018487(pRedFlp-Hgr)(ato37785::2XTY1-SGFP-V5-preTEV-BLRP-3XFLAG)dFRT

Figure 1 – figure supplement 1 B: FlyFos024884(pRedFlp-Hgr)(brk25146::2XTY1-SGFP-V5-preTEV-BLRP-3XFLAG)dFRT

Figure 1 – figure supplement 1 C: FlyFos030836(pRedFlp-Hgr)(salm30926::2XTY1-SGFP-V5-preTEV-BLRP-3XFLAG)dFRT

Figure 1 – figure supplement 1 D: FlyFos029681(pRedFlp-Hgr)(yki19975::2XTY1-SGFP-V5-preTEV-BLRP-3XFLAG)dFRT

Figure 1 – figure supplement 1 E: w^{1118}; PBac(fkh-GFP.FPTB)VK00037/SM5

Figure 1 – figure supplement 1 F: *sd*-eGFP (FlyTrap, homozygous)

Figure 1 – figure supplement 1 G: w^{1118}; PBac(grh-GFP.FPTB)VK00033

Figure 1 – figure supplement 1 H: FlyFos018974(pRedFlp-Hgr)(Scr19370::2XTY1-SGFP-V5-preTEV-BLRP-3XFLAG)dFRT

Figure 1 – figure supplement 1 I: FlyFos015942(pRedFlp-Hgr)(sens31022::2XTY1-SGFP-V5-preTEV-BLRP-3XFLAG)dFRT

Figure 1 – figure supplement 1 J and K: Antp-eGFP (MiMIC) homozygous (line MI02272, converted to an artificial exon)

Figure 1 – figure supplement 1 L: w^{1118}; PBac(Abd-B-EGFP.S)VK00037/SM5

Figure 1 – figure supplement 1 M: w^{1118}; PBac(ey-GFP.FPTB)VK00033

Figure 1 – figure supplement 1 N: w^{1118}; PBac(ss-GFP.A.FPTB)VK00037

Figure 1 – figure supplement 1 O and P: w^{1118}; PBac(grn-GFP.FPTB)VK00037

Figure 2 B and B': *hs*-flp/+; *act5C*-FRT-yellow-FRT-Gal4/+; UAS-SynthAntp long linker-eGFP/+

Figure 2 C and C': *hs*-flp/+; *act5C*-FRT-yellow-FRT-Gal4, UAS-eGFP/+; UAS-Antp long linker (full-length, untagged)/+

Figure 2 F and F': *Dll*-Gal4 (MD23)/+; UAS-SynthAntp-eGFP/*Antp* P1-*lacZ*

Figure 2 – figure supplement 1 A and A': *Antp* P1-*lacZ*/TM3

Figure 2 – figure supplement 1 B and B': *Antp* P2-*lacZ*/CyO

Figure 2 – figure supplement 1 C and C': wild type

Figure 2 – figure supplement 1 D and D': *hs*-flp; *act5C*-FRT-yellow-FRT-Gal4, UAS-eGFP

Figure 2 – figure supplement 1 E and E': *hs*-flp/+; *act5C*-FRT-yellow-FRT-Gal4, UAS-eGFP/+; *Antp* P1-*lacZ*/+

Figure 2 – figure supplement 1 F and F': *hs*-flp/+; *act5C*-FRT-yellow-FRT-Gal4, UAS-eGFP/+; UAS-Antp long linker (full-length, untagged)/*Antp* P1-*lacZ*

Figure 2 – figure supplement 1 G and G': *Dll*-Gal4 (MD23)/+; UAS-Antp long linker (full-length, untagged), UAS-mRFP1(NLS)/ *Antp* P1-*lacZ*

Figure 2 – figure supplement 1 H and H': *Dll*-Gal4 (MD23)/+; UAS-mRFP1(NLS)/ *Antp* P1-*lacZ*

Figure 2 – figure supplement 2 A and E: *Dll*-Gal4 (MD23)/+; UAS-SynthAntp long linker-eGFP/+

Fig 2 – figure supplement 2 B and F: *ptc*-Gal4/+; UAS-SynthAntp long linker-eGFP/+

Figure 2 – figure supplement 2 C and G: *Dll*-Gal4 (MD713)/+; UAS-SynthAntp long linker-eGFP/+

Figure 2 – figure supplement 2 D, H and K, L, O: *69B*-Gal4/UAS-SynthAntp long linker-eGFP

Figure 2 – figure supplement 2 M, N and P: *69B*-Gal4/UAS- eGFP

Figure 3 B, B', G and G': *hs*-flp/+; *ubi*-FRT-mChery-FRT-Gal4/+; Antp-eGFP (MiMIC)/UAS-Antp long linker (full-length, untagged)

Figure 3 C and C': *hs*-flp/+; UAS-Antp^{RNAi}/+; *Antp* P1-*lacZ*/*act5C*-FRT-CD2-FRT-Gal4, UAS-mRFP1(NLS)

Figure 3 H and H': *hs*-flp/+; UAS-Antp^{RNAi}/*act5C*-FRT-yellow-FRT-Gal4, UAS-eGFP; *Antp* P1-*lacZ*/+

Figure 3 – figure supplement 1 B: *Antp* P1-*lacZ*/TM6B

Figure 3 – figure supplement 2 A and A': *hs*-flp/+; *ubi*-FRT-mChery-FRT-Gal4/+; Antp-eGFP (MiMIC)/UAS-Antp long linker (full-length, untagged)

Figure 3 – figure supplement 2 B-C': *hs*-flp/+; *ubi*-FRT-mChery-FRT-Gal4/+; Antp-eGFP (MiMIC)/+

Figure 3 – figure supplement 2 D and D': *hs*-flp/+; *act5C*-FRT-yellow-FRT-Gal4, UAS-eGFP/+; *Antp* P1-*lacZ*/UAS-Antp long linker (full-length, untagged)

Figure 3 – figure supplement 2 E and E': *hs*-flp/+; *act5C*-FRT-yellow-FRT-Gal4/+; UAS-SynthAntp long linker-eGFP/+

Figure 3 – figure supplement 2 F and F': *hs*-flp/+; *act5C*-FRT-yellow-FRT-Gal4, UAS-eGFP/+

Figure 3 – figure supplement 2 G and G': *hs*-flp/+; *act5C*-FRT-yellow-FRT-Gal4, UAS-eGFP/+; *Antp* P1-*lacZ*/+

Figure 3 – figure supplement 2 H and H': *hs*-flp/+; UAS-Antp^{RNAi}/+; Antp-eGFP (MiMIC)/*act5C*-FRT-CD2-FRT-Gal4, UAS-mRFP1(NLS)

Figure 4 B and B': *ptc*-Gal4/+; UAS-SynthAntp long linker-eGFP/+

Figure 4 C and C': *Dll*-Gal4 (MD23)/+; UAS-SynthAntp long linker-eGFP/*Antp* P1-*lacZ*

Figure 4 F and F': *ptc*-Gal4/+; UAS-SynthAntp long linker-eGFP/+

Figure 4 G and G': *Dll*-Gal4 (MD23)/+; UAS-SynthAntp short linker-eGFP/*Antp* P1-*lacZ*

Figure 4 – figure supplement 1 A and A': *hs*-flp/+; *act5C*-FRT-yellow-FRT-Gal4/+; UAS-SynthAntp short linker-eGFP/+

Figure 4 – figure supplement 1 B, B', G and G': *hs*-flp/+; *act5C*-FRT-yellow-FRT-Gal4/+; UAS-SynthAntp short linker-eGFP/*Antp* P1-*lacZ*

Figure 4 – figure supplement 1 C, C', H and H': *hs*-flp/+; *act5C*-FRT-yellow-FRT-Gal4/+; UAS-Antp short linker (full-length, untagged)/*Antp* P1-*lacZ*

Figure 4 – figure supplement 1 D and D': *hs*-flp/+; *Dll*-Gal4 (MD23)/+; UAS-Antp short linker (full-length, untagged), UAS-mRFP1(NLS)/*Antp* P1-*lacZ*

Figure 4 – figure supplement 1 E-F': *hs*-flp/+; *ubi*-FRT-mChery-FRT-Gal4/+; Antp-eGFP (MiMIC)/UAS-Antp short linker (full-length, untagged)

Figure 4 – figure supplement 1 I and I': *ptc*-Gal4/+; UAS-SynthAntp long linker-eGFP/*Antp* P1-*lacZ*

Figure 4 – figure supplement 1 J and J': *ptc*-Gal4/+; UAS-SynthAntp short linker-eGFP/*Antp* P1-*lacZ*

Figure 5 I and J: *Dll*-Gal4 (MD23)/+; UAS-SynthAntp long linker-eGFP/+ or *Dll*-Gal4 (MD23)/+; UAS-SynthAntp short linker-eGFP/+

Figure 5 K: *MS243*-Gal4/+; UAS-SynthAntp long linker-eGFP/*Dr* or *MS243*-Gal4/+; UAS-SynthAntp long linker-eGFP/*Dr*

Figure 5 M and N: *Dll*-Gal4 (MD23)/+; UAS-mCitrine-SynthScr/+

Figure 5 O: *MS243*-Gal4/+; UAS-mCitrine-SynthScr/+

Figure 5 P: *MS243*-Gal4/+; UAS-mCitrine-SynthScr/+

Figure 5 – figure supplement 1 A-B': *ubi*-mRFP1(NLS)/+ or y; Antp-eGFP (MiMIC)/+

Figure 5 – figure supplement 2 A and A': *MS243*-Gal4/+; UAS-SynthAntp long linker-eGFP/*Dr* or *MS243*-Gal4/+; UAS-SynthAntp long linker-eGFP/*Dr*

Figure 5 – figure supplement 2 B and B': *ptc*-Gal4/+; UAS-mCitrine-SynthScr/+

Figure 5 – figure supplement 2 C and C': *MS243*-Gal4/+; UAS-mCitrine-SynthScr/+

Figure 5 – figure supplement 2 D and D': *ptc*-Gal4/+; UAS-mCitrine-SynthScr/*Antp* P1-*lacZ*

Figure 5 – figure supplement 2 E and E': *Dll*-Gal4 (MD23)/+; UAS-mCitrine-SynthScr/*Antp* P1-*lacZ*

Figure 5 – figure supplement 2 F and F': *Dll*-Gal4 (MD23)/+; UAS-mCitrine-SynthScr/+

Figure 5 – figure supplement 2 G and G': *MS243*-Gal4/+; UAS-eGFP/+

Preparation of second and third instar imaginal discs for FCS measurements

For FCS measurements, imaginal discs (eye-antennal, wing, leg, humeral and genital) and salivary glands were dissected from third instar wandering larvae, or wing and leg discs from second instar larvae, in Grace's insect tissue culture medium (ThermoFisher Scientific, 11595030) and transferred to 8-well chambered coverglass (Nunc® Lab-Tek™, 155411) containing PBS just prior to imaging or FCS measurements. Floating imaginal discs or salivary glands were sunk to the bottom of the well using forceps.

Immunostainings in larval imaginal discs

Larval imaginal discs were stained according to (Papadopoulos et al., 2010). Stainings for the endogenous Antp protein have been performed using a mouse anti-Antp antibody (Developmental Studies Hybridoma Bank, University of Iowa, anti-Antp 4C3) in a dilution of 1:250 for embryos and 1:500 for imaginal discs. eGFP, or eGFP-tagged proteins have been stained using mouse or rabbit anti-GFP antibodies from ThermoFisher Scientific in a dilution of 1:500 in imaginal discs and 1:250 in embryos. mRFP1 was stained using a Chromotek rat anti-RFP antibody. For *Antp*

P1 promoter stainings in imaginal discs we used the mouse anti-β-galactosidase 40-1a antibody from Developmental Studies Hybridoma Bank, University of Iowa in a dilution of 1:50. The rabbit anti-Scr antibody was used in a dilution of 1:300 (LeMotte et al., 1989). Confocal images of antibody stainings represent predominatly Z-projections and Zeiss LSM510, Zeiss LSM700 or Zeiss LSM880 Airyscan confocal laser scanning microscopy systems with an inverted stand Axio Observer microscope were used for imaging. Image processing and quantifications have been performed in Fiji (Schindelin et al., 2012). For optimal spectral separation, secondary antibodies coupled to Alexa405, Alexa488, Alexa594 and Cy5 (ThermoFischer Scientific) were used.

Colocalization of wild type and eGFP-tagged MiMIC Antp alleles in imaginal discs

To examine whether the pattern of the MiMIC Antp-eGFP fusion protein recapitulates the Antp wild type expression pattern in both embryo and larval imaginal discs, we performed immunostainings of heterozygous Antp-eGFP and wild type flies to visualize the embryonic (stage 13) and larval expression of *Antp* and eGFP. In this experiment, we 1) visualized the overlap between eGFP and *Antp* (the eGFP pattern reflects the protein encoded by the MiMIC allele, whereas the *Antp* pattern reflects the sum of protein produced by the MiMIC allele and the allele of the balancer chromosome) and 2) compared the eGFP expression pattern to the Antp expression pattern in wild type discs and embryos.

Induction of early and late overexpression and *RNAi*-knockdown clones in imaginal discs

Genetic crosses with approximately 100 virgin female and 100 male flies were set up in bottles and the flies were allowed to mate for 2 days. Then, they were transferred to new bottles and embryos were collected for 6 hours at 25°C. Flies were then transferred to fresh bottles and kept until the next collection at 18°C. To asses Antp auto-activation, the collected eggs were allowed to grow at 25°C for 26 h from the midpoint of collection, when they were subjected to heat-shock by submersion to a water-bath of 38°C for 30 min and then placed back at 25°C until they reached the stage of third instar wandering larvae, when they were collected for dissection, fixation and staining with antibodies. To assess Antp auto-repression, the same procedure was followed, except that the heat-shock was performed at 60 h of development after the midpoint of embryo collection. Whenever necessary, larval genotypes were selected under a dissection stereomicroscope with green and red fluorescence filters on the basis of *deformed* (*dfd*)-YFP bearing balancer chromosomes (Le et al., 2006) and visual inspection of fluorescence in imaginal discs.

Measurement of Antp transcript variant abundance

The linker between the Antp YPWM motif and the homeodomain contains the sequence RSQFGKCQE. Short linker isoforms encode the sequence RSQFE, whereas long linker isoforms are generated by alternative splicing of a 12 base pair sequence encoding the four amino acid sequence GKCQ into the mRNA. We initially designed primer pairs for RT-qPCR experiments to distinguish between the short and long linker mRNA variants. For the short linker variant, we used nucleotide sequences corresponding to RSQFERKR (with RKR being the first 3 amino acids of the homeodomain). For detection of the long linker variant we designed primers

either corresponding to the RSQFGKCQ sequence, or GKCQERKR. We observed in control PCRs (using plasmid DNA harboring either a long or a short linker cDNA) that primers designed for the short linker variant still amplified the long linker one. Moreover, with linker sequences differing in only four amino acids, encoded by 12 base pars, primer pairs flanking the linker could also not be used, since, due to very similar sizes, both variants would be amplified in RT-qPCR experiments with almost equal efficiencies. Therefore, we used primer pairs flanking the linker region to indiscriminately amplify short and long linker variants, using non-saturating PCR (18 cycles) on total cDNA generated from total RNA. We then resolved and assessed the relative amounts of long and short linker amplicons in a second step using Fragment Analyzer (Advanced Analytical). RNA was extracted from stage 13 embryos, second instar larvae at 60 h of development, and leg or wing discs from third instar wandering larvae using the Trizol® reagent (ThermoFischer Scientific), following the manufacturer's instructions. Total RNA amounts were measured by NanoDrop and equal amounts were used to synthesize cDNA using High-Capacity RNA-to-cDNA™ Kit (ThermoFischer Scientific), following the manufacturer's instructions. Total cDNA yields were measured by NanoDrop and equal amounts were used in PCR, using in-house produced Taq polymerase. 10 ng of plasmid DNA, bearing either a long or a short transcript cDNA were used as a control. PCR product abundance was analyzed both by agarose gel electrophoresis and using Fragment Analyzer (Advanced Analytical).

The quantification of the transcript variant concentration (Figure 4 D and H) has been made considering 100% (value equal to 1 on the y axis) as the sum of long and short isoforms at each developmental stage, whereas the quantification of the relative activation and repression efficiency has been performed considering the

short linker variant as having 100% repression and the long linker variant as having 100% activation (values equal to 1 on the y-axis) efficiency.

Quantification of the relative repressing and activating efficiencies of different Antp isoforms

Quantification of the relative efficiency of Antp activating and repressing isoforms (Figure 4 D and H) were performed in Fiji (Schindelin et al., 2012) by selection of the total region of repression or activation of Antp protein or P1 reporter staining and quantification of the relative fluorescence intensity of the selected regions. 5-7 imaginal disc images per investigated genotype were used for analysis. For the repression assay the obtained values have been normalized over the intensity of Antp protein calculated in the region of overlap between eGFP and Antp (negative control). In both cases (repression and activation), the highest efficiency per transcript variant (for repression, the short linker isoform; for activation the long linker isoform) have been set to 100%.

Gel-shifts (Electrophoretic Mobility Shift Assays – EMSAs)

Full-length Antp short and long linker variants (transcript variants RM and RN), encoding activating and repressing Antp isoforms, respectively, were cloned into the pET21b(+) vector (Novagen), which features a C-terminal 6xHis tag, and expressed in Rosetta^{TM} 2 cells (Novagen), following the manufacturer's standard protocol. The two proteins were then Ni-column purified and subjected to gel-filtration. The concentrations of purified proteins were then compared by Western blotting, using the anti-Antp 4C3 antibody (Developmental Studies Hybridoma Bank, University of Iowa), and equal starting concentrations were used in successive

twofold serial dilutions in gel-shift experiments. The BS1and BS2 binding sites have been identified ~2 kb upstream of the *engrailed* gene promoter and characterized for Antp binding previously (Affolter et al., 1990). The HB1 binding site has been described previously (Keegan et al., 1997) and is a binding site found in the intron of the mouse *Hoxa-4* gene. The D4 probe has been characterized previously (Duncan et al., 2010) as a functional element in the *spineless* gene.

Fluorescence Microscopy Imaging of live imaginal discs and FCS

Fluorescence imaging and FCS measurements were performed on two uniquely modified confocal laser scanning microscopy systems, both comprised of the ConfoCor3 system (Carl Zeiss, Jena, Germany) and consisting of either an inverted microscope for transmitted light and epifluorescence (Axiovert 200 M); a VIS-laser module comprising the Ar/ArKr (458, 477, 488 and 514 nm), HeNe 543 nm and HeNe 633 nm lasers and the scanning module LSM510 META; or a Zeiss LSM780 inverted setup, comprising Diode 405 nm, Ar multiline 458, 488 and 514 nm, DPSS 561 nm and HeNe 633 nm lasers. Both instruments were modified to enable detection using silicon Avalanche Photo Detectors (SPCM-AQR-1X; PerkinElmer, USA) for imaging and FCS. Images were recorded at a 512X512 pixel resolution. C-Apochromat 40x/1.2 W UV-VIS-IR objectives were used throughout. Fluorescence intensity fluctuations were recorded in arrays of 10 consecutive measurements, each measurement lasting 10 s. Averaged curves were analyzed using the software for online data analysis or exported and fitted offline using the OriginPro 8 data analysis software (OriginLab Corporation, Northampton, MA). In either case, the nonlinear least square fitting of the autocorrelation curve was performed using the Levenberg–Marquardt algorithm. Quality of the fitting was

evaluated by visual inspection and by residuals analysis. Control FCS measurements to asses the detection volume were routinely performed prior to data acquisition, using dilute solutions of known concentration of Rhodamine 6G and Alexa488 dyes. The variability between independent measurements reflects variabilitys between cells, rather than imprecision of FCS measurements. For more details on Fluorescence Microscopy Imaging and FCS, refer to Supplement 1.

Sample size, biological and technical replicates

For the measurement of TF molecular numbers and variability (Figure 1 and Figure 1 – figure supplement 1), 7-10 larvae of each fly strain were dissected, yielding at least 15 imaginal discs, which were used in FCS analysis. For the Fkh TF, 7 pairs of salivary glands were analyzed and for AbdB, 12 genital discs were dissected from 12 larvae. More than 50 FCS measurements were performed in patches of neighboring cells of these dissected discs, in the regions of expression indicated in Figure 1 by arrows. Imaginal discs from the same fly strain (expressing a given endogenously-tagged TF) were analyzed on at least 3 independent instances (FCS sessions), taking place on different days (biological replicates) and for Antp, which was further analyzed in this study, more than 20 independent FCS sessions were used. As routinely done with FCS measurements in live cells, these measurements were evaluated during acquisition and subsequent analysis and, based on their quality (high counts per molecule and second, low photobleaching), were included in the calculation of concentration and variability. In Figure 1 – figure supplement 1 Q, *n* denotes the number of FCS measurements included in the calculations.

For experiments involving immunostainings in imaginal discs to investigate the auto-regulatory behavior of Antp (Figures 2-5 and supplements thereof, except for the temporally-resolved auto-activating and repressing study of Antp in Figure 3, as discussed above), 14-20 male and female flies were mated in bottles and 10 larvae were selected by means of fluorescent balancers and processed downstream. Up to 20 imaginal discs were visualized by fluorescence microscopy and high resolution Z-stacks were acquired for 3-5 representative discs or disc regions of interest per experiment. All experiments were performed in triplicate, except for the temporal analysis of Antp auto-regulatory behavior in Figure 3 (and figure supplements thereof), which was performed 6 times and the quantification of repression efficiency of short and long linker Antp isoforms in Figure 5 (and figure supplements thereof), which was performed 5 times.

For the quantification of transcript variant abundance in Figure 4 D and H, RNA and thus cDNA was prepared from each stage 3 independent times (biological replicates) and the transcript abundance per RNA/cDNA sample was also analyzed 3 times.

For the experiments involving perturbations in Antp expression whereby the proper development of the leg and the notum have been assessed in Figure 5, more than 100 adult flies have been analyzed and this experiment has been performed more than 10 times independently.

References

Abbott, M.K., and Kaufman, T.C. (1986). The relationship between the functional complexity and the molecular organization of the Antennapedia locus of Drosophila melanogaster. Genetics *114*, 919-942.

1372 Affolter, M., Percival-Smith, A., Muller, M., Leupin, W., and Gehring, W.J. (1990).
1373 DNA binding properties of the purified Antennapedia homeodomain. Proc Natl Acad
1374 Sci U S A *87*, 4093-4097.
1375 Becskei, A., and Serrano, L. (2000). Engineering stability in gene networks by
1376 autoregulation. Nature *405*, 590-593.
1377 Blake, W.J., M, K.A., Cantor, C.R., and Collins, J.J. (2003). Noise in eukaryotic gene
1378 expression. Nature *422*, 633-637.
1379 Boettiger, A.N., and Levine, M. (2013). Rapid transcription fosters coordinate snail
1380 expression in the Drosophila embryo. Cell reports *3*, 8-15.
1381 Buszczak, M., Paterno, S., Lighthouse, D., Bachman, J., Planck, J., Owen, S.,
1382 Skora, A.D., Nystul, T.G., Ohlstein, B., Allen, A.*, et al.* (2007). The carnegie protein
1383 trap library: a versatile tool for Drosophila developmental studies. Genetics *175*,
1384 1505-1531.
1385 Calleja, M., Moreno, E., Pelaz, S., and Morata, G. (1996). Visualization of gene
1386 expression in living adult Drosophila. Science *274*, 252-255.
1387 Clark, N.M., Hinde, E., Winter, C.M., Fisher, A.P., Crosti, G., Blilou, I., Gratton, E.,
1388 Benfey, P.N., and Sozzani, R. (2016). Tracking transcription factor mobility and
1389 interaction in Arabidopsis roots with fluorescence correlation spectroscopy. eLife *5*.
1390 Crickmore, M.A., Ranade, V., and Mann, R.S. (2009). Regulation of Ubx expression
1391 by epigenetic enhancer silencing in response to Ubx levels and genetic variation.
1392 PLoS genetics *5*, e1000633.
1393 Crocker, J., Abe, N., Rinaldi, L., McGregor, A.P., Frankel, N., Wang, S., Alsawadi,
1394 A., Valenti, P., Plaza, S., Payre, F.*, et al.* (2015). Low affinity binding site clusters
1395 confer hox specificity and regulatory robustness. Cell *160*, 191-203.

1396 Crocker, J., Noon, E.P., and Stern, D.L. (2016). The Soft Touch: Low-Affinity
1397 Transcription Factor Binding Sites in Development and Evolution. Current topics in
1398 developmental biology *117*, 455-469.
1399 Crocker, J., Tsai, A., Muthusamy, A.K., Lavis, L.K., Singer, R.H., and Stern, D.L.
1400 (2017). Nuclear microenvironments modulate transcription from low-affinity
1401 enhancers. bioRxiv.
1402 Dublanche, Y., Michalodimitrakis, K., Kummerer, N., Foglierini, M., and Serrano, L.
1403 (2006). Noise in transcription negative feedback loops: simulation and experimental
1404 analysis. Mol Syst Biol *2*, 41.
1405 Duncan, D., Kiefel, P., and Duncan, I. (2010). Control of the spineless antennal
1406 enhancer: direct repression of antennal target genes by Antennapedia. Dev Biol *347*,
1407 82-91.
1408 Dworkin, I., Lee, W., McCloskey, F., and Larsen, E. (2007). Complex genetic
1409 interactions govern the temporal effects of Antennapedia on antenna-to-leg
1410 transformations in Drosophila melanogaster. J Genet *86*, 111-123.
1411 Ejsmont, R.K., Bogdanzaliewa, M., Lipinski, K.A., and Tomancak, P. (2011).
1412 Production of fosmid genomic libraries optimized for liquid culture recombineering
1413 and cross-species transgenesis. Methods in molecular biology *772*, 423-443.
1414 Ejsmont, R.K., Sarov, M., Winkler, S., Lipinski, K.A., and Tomancak, P. (2009). A
1415 toolkit for high-throughput, cross-species gene engineering in Drosophila. Nat
1416 Methods *6*, 435-437.
1417 Elowitz, M.B., Levine, A.J., Siggia, E.D., and Swain, P.S. (2002). Stochastic gene
1418 expression in a single cell. Science *297*, 1183-1186.
1419 Engstrom, Y., Schneuwly, S., and Gehring, W.J. (1992). Spatial and Temporal
1420 Expression of an Antennapedia Lac Z Gene Construct Integrated into the

1421 Endogenous Antennapedia Gene of Drosophila-Melanogaster. Dev Genes Evol *201*,
1422 65-80.
1423 Franz, K., Singh, A., and Weinberger, L.S. (2011). Lentiviral vectors to study
1424 stochastic noise in gene expression. Methods in enzymology *497*, 603-622.
1425 Garaulet, D.L., Foronda, D., Calleja, M., and Sanchez-Herrero, E. (2008). Polycomb-
1426 dependent Ultrabithorax Hox gene silencing induced by high Ultrabithorax levels in
1427 Drosophila. Development *135*, 3219-3228.
1428 Gillespie, D.T. (2007). Stochastic simulation of chemical kinetics. Annu Rev Phys
1429 Chem *58*, 35-55.
1430 Gregor, T., Tank, D.W., Wieschaus, E.F., and Bialek, W. (2007a). Probing the limits
1431 to positional information. Cell *130*, 153-164.
1432 Gregor, T., Wieschaus, E.F., McGregor, A.P., Bialek, W., and Tank, D.W. (2007b).
1433 Stability and nuclear dynamics of the bicoid morphogen gradient. Cell *130*, 141-152.
1434 Gronlund, A., Lotstedt, P., and Elf, J. (2013). Transcription factor binding kinetics
1435 constrain noise suppression via negative feedback. Nat Commun *4*, 1864.
1436 Holloway, D.M., Lopes, F.J., da Fontoura Costa, L., Travencolo, B.A., Golyandina,
1437 N., Usevich, K., and Spirov, A.V. (2011). Gene expression noise in spatial patterning:
1438 hunchback promoter structure affects noise amplitude and distribution in Drosophila
1439 segmentation. PLoS computational biology *7*, e1001069.
1440 Holloway, D.M., and Spirov, A.V. (2015). Mid-embryo patterning and precision in
1441 Drosophila segmentation: Kruppel dual regulation of hunchback. PLoS One *10*,
1442 e0118450.
1443 Ito, K., Awano, W., Suzuki, K., Hiromi, Y., and Yamamoto, D. (1997). The Drosophila
1444 mushroom body is a quadruple structure of clonal units each of which contains a
1445 virtually identical set of neurones and glial cells. Development *124*, 761-771.

1446 Jorgensen, E.M., and Garber, R.L. (1987). Function and misfunction of the two
1447 promoters of the Drosophila Antennapedia gene. Genes Dev *1*, 544-555.
1448 Kang, M., Piliszek, A., Artus, J., and Hadjantonakis, A.K. (2013). FGF4 is required
1449 for lineage restriction and salt-and-pepper distribution of primitive endoderm factors
1450 but not their initial expression in the mouse. Development *140*, 267-279.
1451 Kaur, G., Costa, M.W., Nefzger, C.M., Silva, J., Fierro-Gonzalez, J.C., Polo, J.M.,
1452 Bell, T.D., and Plachta, N. (2013). Probing transcription factor diffusion dynamics in
1453 the living mammalian embryo with photoactivatable fluorescence correlation
1454 spectroscopy. Nat Commun *4*, 1637.
1455 Keegan, L.P., Haerry, T.E., Crotty, D.A., Packer, A.I., Wolgemuth, D.J., and Gehring,
1456 W.J. (1997). A sequence conserved in vertebrate Hox gene introns functions as an
1457 enhancer regulated by posterior homeotic genes in Drosophila imaginal discs.
1458 Mechanisms of development *63*, 145-157.
1459 Kelso, R.J., Buszczak, M., Quinones, A.T., Castiblanco, C., Mazzalupo, S., and
1460 Cooley, L. (2004). Flytrap, a database documenting a GFP protein-trap insertion
1461 screen in Drosophila melanogaster. Nucleic Acids Res *32*, D418-420.
1462 Krasnow, M.A., Saffman, E.E., Kornfeld, K., and Hogness, D.S. (1989).
1463 Transcriptional activation and repression by Ultrabithorax proteins in cultured
1464 Drosophila cells. Cell *57*, 1031-1043.
1465 Kuziora, M.A., and McGinnis, W. (1988). Autoregulation of a Drosophila homeotic
1466 selector gene. Cell *55*, 477-485.
1467 Lam, C.S., Mistri, T.K., Foo, Y.H., Sudhaharan, T., Gan, H.T., Rodda, D., Lim, L.H.,
1468 Chou, C., Robson, P., Wohland, T.*, et al.* (2012). DNA-dependent Oct4-Sox2
1469 interaction and diffusion properties characteristic of the pluripotent cell state revealed
1470 by fluorescence spectroscopy. The Biochemical journal *448*, 21-33.

Le, T., Liang, Z., Patel, H., Yu, M.H., Sivasubramaniam, G., Slovitt, M., Tanentzapf, G., Mohanty, N., Paul, S.M., Wu, V.M., *et al.* (2006). A new family of Drosophila balancer chromosomes with a w- dfd-GMR yellow fluorescent protein marker. Genetics *174*, 2255-2257.

LeMotte, P.K., Kuroiwa, A., Fessler, L.I., and Gehring, W.J. (1989). The homeotic gene Sex Combs Reduced of Drosophila: gene structure and embryonic expression. EMBO J *8*, 219-227.

Li, Y., Wang, F., Lee, J.A., and Gao, F.B. (2006). MicroRNA-9a ensures the precise specification of sensory organ precursors in Drosophila. Genes Dev *20*, 2793-2805.

Little, S.C., Tikhonov, M., and Gregor, T. (2013). Precise developmental gene expression arises from globally stochastic transcriptional activity. Cell *154*, 789-800.

Lo, C.A., Kays, I., Emran, F., Lin, T.J., Cvetkovska, V., and Chen, B.E. (2015). Quantification of Protein Levels in Single Living Cells. Cell reports *13*, 2634-2644.

Lucas, T., Ferraro, T., Roelens, B., De Las Heras Chanes, J., Walczak, A.M., Coppey, M., and Dostatni, N. (2013). Live imaging of bicoid-dependent transcription in Drosophila embryos. Current biology : CB *23*, 2135-2139.

Mistri, T.K., Devasia, A.G., Chu, L.T., Ng, W.P., Halbritter, F., Colby, D., Martynoga, B., Tomlinson, S.R., Chambers, I., Robson, P., *et al.* (2015). Selective influence of Sox2 on POU transcription factor binding in embryonic and neural stem cells. EMBO reports *16*, 1177-1191.

Morin, X., Daneman, R., Zavortink, M., and Chia, W. (2001). A protein trap strategy to detect GFP-tagged proteins expressed from their endogenous loci in Drosophila. Proc Natl Acad Sci U S A *98*, 15050-15055.

1494 Muller, C.B., Loman, A., Pacheco, V., Koberling, F., Willbold, D., Richtering, W., and
1495 Enderlein, J. (2008). Precise measurement of diffusion by multi-color dual-focus
1496 fluorescence correlation spectroscopy. Epl-Europhys Lett *83*.
1497 Nevozhay, D., Adams, R.M., Murphy, K.F., Josic, K., and Balazsi, G. (2009).
1498 Negative autoregulation linearizes the dose-response and suppresses the
1499 heterogeneity of gene expression. Proc Natl Acad Sci U S A *106*, 5123-5128.
1500 Newman, J.R., Ghaemmaghami, S., Ihmels, J., Breslow, D.K., Noble, M., DeRisi,
1501 J.L., and Weissman, J.S. (2006). Single-cell proteomic analysis of S. cerevisiae
1502 reveals the architecture of biological noise. Nature *441*, 840-846.
1503 Papadopoulos, D.K., Krmpot, A.J., Nikolic, S.N., Krautz, R., Terenius, L., Tomancak,
1504 P., Rigler, R., Gehring, W.J., and Vukojevic, V. (2015). Probing the kinetic landscape
1505 of Hox transcription factor-DNA binding in live cells by massively parallel
1506 Fluorescence Correlation Spectroscopy. Mechanisms of development *138 Pt 2*, 218-
1507 225.
1508 Papadopoulos, D.K., Resendez-Perez, D., Cardenas-Chavez, D.L., Villanueva-
1509 Segura, K., Canales-del-Castillo, R., Felix, D.A., Funfschilling, R., and Gehring, W.J.
1510 (2011). Functional synthetic Antennapedia genes and the dual roles of YPWM motif
1511 and linker size in transcriptional activation and repression. Proc Natl Acad Sci U S A
1512 *108*, 11959-11964.
1513 Papadopoulos, D.K., Vukojevic, V., Adachi, Y., Terenius, L., Rigler, R., and Gehring,
1514 W.J. (2010). Function and specificity of synthetic Hox transcription factors in vivo.
1515 Proc Natl Acad Sci U S A *107*, 4087-4092.
1516 Pare, A., Lemons, D., Kosman, D., Beaver, W., Freund, Y., and McGinnis, W.
1517 (2009). Visualization of individual Scr mRNAs during Drosophila embryogenesis
1518 yields evidence for transcriptional bursting. Current biology : CB *19*, 2037-2042.

1519 Paulsson, J. (2004). Summing up the noise in gene networks. Nature *427*, 415-418.

1520 Pavlopoulos, A., and Akam, M. (2011). Hox gene Ultrabithorax regulates distinct sets
1521 of target genes at successive stages of Drosophila haltere morphogenesis. Proc Natl
1522 Acad Sci U S A *108*, 2855-2860.

1523 Pelaez, N., Gavalda-Miralles, A., Wang, B., Navarro, H.T., Gudjonson, H., Rebay, I.,
1524 Dinner, A.R., Katsaggelos, A.K., Amaral, L.A., and Carthew, R.W. (2015). Dynamics
1525 and heterogeneity of a fate determinant during transition towards cell differentiation.
1526 eLife *4*.

1527 Perez-Camps, M., Tian, J., Chng, S.C., Sem, K.P., Sudhaharan, T., Teh, C.,
1528 Wachsmuth, M., Korzh, V., Ahmed, S., and Reversade, B. (2016). Quantitative
1529 imaging reveals real-time Pou5f3-Nanog complexes driving dorsoventral
1530 mesendoderm patterning in zebrafish. eLife *5*.

1531 Plachta, N., Bollenbach, T., Pease, S., Fraser, S.E., and Pantazis, P. (2011). Oct4
1532 kinetics predict cell lineage patterning in the early mammalian embryo. Nat Cell Biol
1533 *13*, 117-123.

1534 Quinones-Coello, A.T., Petrella, L.N., Ayers, K., Melillo, A., Mazzalupo, S., Hudson,
1535 A.M., Wang, S., Castiblanco, C., Buszczak, M., Hoskins, R.A.*, et al.* (2007).
1536 Exploring strategies for protein trapping in Drosophila. Genetics *175*, 1089-1104.

1537 Rao, C.V., and Arkin, A.P. (2003). Stochastic chemical kinetics and the quasi-
1538 steady-state assumption: Application to the Gillespie algorithm. J Chem Phys *118*,
1539 4999-5010.

1540 Reed, H.C., Hoare, T., Thomsen, S., Weaver, T.A., White, R.A., Akam, M., and
1541 Alonso, C.R. (2010). Alternative splicing modulates Ubx protein function in
1542 Drosophila melanogaster. Genetics *184*, 745-758.

1543 Saadaoui, M., Merabet, S., Litim-Mecheri, I., Arbeille, E., Sambrani, N., Damen, W.,
1544 Brena, C., Pradel, J., and Graba, Y. (2011). Selection of distinct Hox-Extradenticle
1545 interaction modes fine-tunes Hox protein activity. Proc Natl Acad Sci U S A *108*,
1546 2276-2281.
1547 Sanchez, A., Garcia, H.G., Jones, D., Phillips, R., and Kondev, J. (2011). Effect of
1548 promoter architecture on the cell-to-cell variability in gene expression. PLoS
1549 computational biology *7*, e1001100.
1550 Sarov, M., Barz, C., Jambor, H., Hein, M.Y., Schmied, C., Suchold, D., Stender, B.,
1551 Janosch, S., K, J.V., Krishnan, R.T.*, et al.* (2016). A genome-wide resource for the
1552 analysis of protein localisation in Drosophila. eLife *5*, e12068.
1553 Schindelin, J., Arganda-Carreras, I., Frise, E., Kaynig, V., Longair, M., Pietzsch, T.,
1554 Preibisch, S., Rueden, C., Saalfeld, S., Schmid, B.*, et al.* (2012). Fiji: an open-source
1555 platform for biological-image analysis. Nat Methods *9*, 676-682.
1556 Schwanhausser, B., Busse, D., Li, N., Dittmar, G., Schuchhardt, J., Wolf, J., Chen,
1557 W., and Selbach, M. (2011). Global quantification of mammalian gene expression
1558 control. Nature *473*, 337-342.
1559 Sheth, R., Bastida, M.F., Kmita, M., and Ros, M. (2014). "Self-Regulation," A New
1560 Facet of Hox Genes' Function. Dev Dynam *243*, 182-191.
1561 Shimoga, V., White, J.T., Li, Y., Sontag, E., and Bleris, L. (2013). Synthetic
1562 mammalian transgene negative autoregulation. Mol Syst Biol *9*, 670.
1563 Slattery, M., Voutev, R., Ma, L., Negre, N., White, K.P., and Mann, R.S. (2013).
1564 Divergent transcriptional regulatory logic at the intersection of tissue growth and
1565 developmental patterning. PLoS genetics *9*, e1003753.
1566 Smolander, O.P., Kandhavelu, M., Mannerstrom, H., Lihavainen, E., Kalaichelvan,
1567 S., Healy, S., Yli-Harja, O., Karp, M., and Ribeiro, A.S. (2011). Cell-to-cell diversity in

protein levels of a gene driven by a tetracycline inducible promoter. BMC molecular biology *12*, 21.

Stroeher, V.L., Gaiser, J.C., and Garber, R.L. (1988). Alternative RNA splicing that is spatially regulated: generation of transcripts from the Antennapedia gene of Drosophila melanogaster with different protein-coding regions. Molecular and cellular biology *8*, 4143-4154.

Swain, P.S., Elowitz, M.B., and Siggia, E.D. (2002). Intrinsic and extrinsic contributions to stochasticity in gene expression. Proc Natl Acad Sci U S A *99*, 12795-12800.

Szaloki, N., Krieger, J.W., Komaromi, I., Toth, K., and Vamosi, G. (2015). Evidence for Homodimerization of the c-Fos Transcription Factor in Live Cells Revealed by Fluorescence Microscopy and Computer Modeling. Molecular and cellular biology *35*, 3785-3798.

Taniguchi, Y., Choi, P.J., Li, G.W., Chen, H., Babu, M., Hearn, J., Emili, A., and Xie, X.S. (2010). Quantifying E. coli proteome and transcriptome with single-molecule sensitivity in single cells. Science *329*, 533-538.

Thattai, M., and van Oudenaarden, A. (2001). Intrinsic noise in gene regulatory networks. Proc Natl Acad Sci U S A *98*, 8614-8619.

Tiwari, M., Mikuni, S., Muto, H., and Kinjo, M. (2013). Determination of dissociation constant of the NFkappaB p50/p65 heterodimer using fluorescence cross-correlation spectroscopy in the living cell. Biochemical and biophysical research communications *436*, 430-435.

Tsutsumi, M., Muto, H., Myoba, S., Kimoto, M., Kitamura, A., Kamiya, M., Kikukawa, T., Takiya, S., Demura, M., Kawano, K.*, et al.* (2016). In vivo fluorescence correlation

spectroscopy analyses of FMBP-1, a silkworm transcription factor. FEBS open bio *6*, 106-125.

Venken, K.J., Schulze, K.L., Haelterman, N.A., Pan, H., He, Y., Evans-Holm, M., Carlson, J.W., Levis, R.W., Spradling, A.C., Hoskins, R.A.*, et al.* (2011). MiMIC: a highly versatile transposon insertion resource for engineering Drosophila melanogaster genes. Nat Methods *8*, 737-743.

Vukojevic, V., Heidkamp, M., Ming, Y., Johansson, B., Terenius, L., and Rigler, R. (2008). Quantitative single-molecule imaging by confocal laser scanning microscopy. Proc Natl Acad Sci U S A *105*, 18176-18181.

Vukojevic, V., Papadopoulos, D.K., Terenius, L., Gehring, W.J., and Rigler, R. (2010). Quantitative study of synthetic Hox transcription factor-DNA interactions in live cells. Proc Natl Acad Sci U S A *107*, 4093-4098.

Zechner, C., Ruess, J., Krenn, P., Pelet, S., Peter, M., Lygeros, J., and Koeppl, H. (2012). Moment-based inference predicts bimodality in transient gene expression. Proc Natl Acad Sci U S A *109*, 8340-8345.

Zink, B., Engstrom, Y., Gehring, W.J., and Paro, R. (1991). Direct interaction of the Polycomb protein with Antennapedia regulatory sequences in polytene chromosomes of Drosophila melanogaster. EMBO J *10*, 153-162.

Supplemental information

Supplement 1: Background on Fluorescence Microscopy Imaging and FCS

Two individually modified instruments (Zeiss, LSM 510 and 780, ConfoCor 3) with fully integrated FCS/CLSM optical pathways were used for imaging. The detection efficiency of CLSM imaging was significantly improved by the introduction of APD detectors. As compared to PMTs, which are normally used as detectors in

conventional CLSM, the APDs are characterized by higher quantum yield and collection efficiency – about 70 % in APDs as compared to 15 – 25 % in PMTs, higher gain, negligible dark current and better efficiency in the red part of the spectrum. Enhanced fluorescence detection efficiency enabled image collection using fast scanning ($1 - 5\ \mu s/pixel$). This enhances further the signal-to-noise-ratio by avoiding fluorescence loss due to triplet state formation, enabling fluorescence imaging with single-molecule sensitivity. In addition, low laser intensities ($150 - 750\ \mu W$) could be applied for imaging, significantly reducing the photo-toxicity (Vukojevic et al., 2008).

FCS measurements are performed by recording fluorescence intensity fluctuations in a very small, approximately ellipsoidal observation volume element (OVE) (about $0.2 \mu m$ wide and $1 \mu m$ long) that is generated in imaginal disc cells by focusing the laser light through the microscope objective and by collecting the fluorescence light through the same objective using a pinhole in front of the detector to block out-of-focus light. The fluorescence intensity fluctuations, caused by fluorescently labeled molecules passing through the OVE are analyzed using temporal autocorrelation analysis.

In temporal autocorrelation analysis we first derive the autocorrelation function $G(\tau)$:

$$G(\tau) = 1 + \frac{\langle \delta I(t) \cdot \delta I(t+\tau) \rangle}{\langle I(t) \rangle^2} \quad \text{(S1)},$$

where $\delta I(t) = I(t) - \langle I(t) \rangle$ is the deviation from the mean intensity at time t and $\delta I(t+\tau) = I(t+\tau) - \langle I(t) \rangle$ is the deviation from the mean intensity at time $t + \tau$. For further analysis, an autocorrelation curve is derived by plotting $G(\tau)$ as a function of the lag time, i.e. the autocorrelation time τ.

To derive information about molecular numbers and their corresponding diffusion time, the experimentally obtained autocorrelation curves are compared to autocorrelation functions derived for different model systems. A model describing free three dimensional (3D) diffusion of two components and triplet formation was used in this study:

$$G(\tau) = 1 + \frac{1}{N}\left(\frac{1-y}{\left(1+\frac{\tau}{\tau_{D_1}}\right)\cdot\sqrt{1+\frac{w_{xy}^2\tau}{w_z^2\tau_{D_1}}}} + \frac{y}{\left(1+\frac{\tau}{\tau_{D_2}}\right)\cdot\sqrt{1+\frac{w_{xy}^2\tau}{w_z^2\tau_{D_2}}}}\right)\cdot\left(1+\frac{T}{1-T}\cdot e^{-\frac{\tau}{\tau_T}}\right) \quad \text{(S2)}$$

In the above equation, *N* is the average number of molecules in the OVE; *y* is the fraction of the slowly moving Antp-eGFP molecules; τ_{D_1} is the diffusion time of the free Antp-eGFP molecules; τ_{D_2} is the diffusion time of Antp-eGFP molecules undergoing interactions with the DNA; w_{xy} and w_z are radial and axial parameters, respectively, related to spatial properties of the OVE; T is the average equilibrium fraction of molecules in the triplet state; and τ_T the triplet correlation time related to rate constants for intersystem crossing and the triplet decay. Spatial properties of the detection volume, represented by the square of the ratio of the axial and radial parameters ($\left(\frac{w_z}{w_{xy}}\right)^2$), are determined in calibration measurements performed using a solution of Rhodamine 6G for which the diffusion coefficient (D) is known to be $D_{Rh6G} = 4.1 \cdot 10^{-10}\, m^2 s^{-1}$ (Muller et al., 2008). The diffusion time, τ_D, measured by FCS, is related to the translation diffusion coefficient *D* by:

$$\tau_D = \frac{w_{xy}^2}{4D} \quad \text{(S3)}.$$

To establish that Antp molecules diffusing through the OVE are the underlying cause of the recorded fluorescence intensity fluctuations, we plotted the characteristic decay times τ_{D1} and τ_{D2}, obtained by FCS, as a function of the total concentration of Antp molecules (Figure

1 – figure supplement 2). We observed that both characteristic decay times remain stable for increasing total concentration of Antp molecules, signifying that the underlying process triggering the fluorescence intensity fluctuations is diffusion of fluorescent Antp molecules through the OVE (which should be independent of the total concentration of Antp molecules).

Supplement 2: Calculation of the concentration of endogenous TFs and average number of molecules in imaginal disc cell nuclei from FCS measurements (exemplified for Antp)

The Observation Volume Element (OVE), which can be approximated by a prolate ellipsoid, has a volume of:

$$V_{OVE} = \pi^{\frac{3}{2}} \cdot w_{xy}^2 \cdot z_0 = 5.57 \cdot 0.1847^{\mathbf{2}} \cdot 1 = 0.223 \cdot 10^{-18}\, m^3 = 0.19 \cdot 10^{-15} L \quad \text{(S4)}.$$

Therefore, one fluorescent molecule in the OVE yields equal concentration to:

$\frac{1}{0.19 \cdot 10^{-15}} = 5.263 \cdot 10^{15}$ molecules per L.

$1\ M$ of Antp-eGFP molecules equals $6.022 \cdot 10^{23}$ molecules/L,

$x\ M$ of Antp-eGFP molecules equal $5.263 \cdot 10^{15}$ molecules/L.

Therefore:

$$x = \frac{5.263 \cdot 10^{15}}{6.022 \cdot 10^{23}} = 0.874 \cdot 10^{-8}\ M = 8.74\ nM \quad \text{(S5)}.$$

This indicates that one molecule in the OVE corresponds on the average to $8.74\ nM$ concentration of fluorescent molecules in the nucleus.

The wing disc cells within the Antp expression domain (prescutum precursors) are not spherical, but rather ellipsoidal. Their axes were determined by fluorescence imaging to be 1.4 μm in the transverse dimension and 2.8 μm in the longitudinal. The volume of the nucleus was approximated by the volume of a prolate ellipsoid:

$$V_{nucleus} = \frac{4}{3}\pi a^2 b = \frac{4}{3} \cdot 3.14 \cdot (1.4 \cdot 10^{-6})^2 \cdot 2.8 \cdot 10^{-6}\, m^3 = 22.99 \cdot 10^{-18}\, m^3 = 22.99 \cdot 10^{-15}\, L \quad \text{(S6)}.$$

Therefore, the OVE represents roughly $1/121$ of the nuclear volume:

$$\frac{V_{nucleus}}{V_{OVE}} = 121 \quad \text{(S7)}$$

and the number of molecules in Antp-eGFP nuclei is on the average $57.37 \cdot 121 \approx 6942$ molecules.

The concentration of Antp in the wing disc nuclei is calculated as follows:

$1\ mol$ of Antp-eGFP molecules equals $6.023 \cdot 10^{23}$,

$n\ mol$ of Antp-eGFP molecules equal 6942.

Thus $n_{Antp-eGFP} = \frac{6942}{6.022 \cdot 10^{23}} = 1152.77 \cdot 10^{-23}\ mol$ (S8).

Thus the concentration of Antp-eGFP within the diploid wing disc nucleus will be:

$$C_{Antp-eGFP} = \frac{1182.77 \cdot 10^{-23}}{22.99 \cdot 10^{-15}} = 50.1 \cdot 10^{-8}\ M \approx 501\ nM \quad \text{(S9)},$$

equivalent to $57.37 \cdot 8.74 \approx 501\ nM$.

Fitting of autocorrelation curves using a model for free three dimensional (3D) diffusion of two components and triplet, revealed that on the average 63% of the total Antp-eGFP molecules are fast moving and appear to be freely diffusing in the nucleus, whereas 37% are slow and are likely participating in the formation of complexes with chromatin.

Supplement 3: Calculation of the ratio of apparent Antp dissociation constant for short and long linker Antp isoforms from FCS measurements on ectopically expressed Antp

The Antp TF undergoes both specific and non-specific interactions with DNA. Assuming that non-specific interactions precede the specific ones, a two-step process of consecutive reactions is anticipated (Vukojevic et al., 2010):

$$DNA_{ns} + Antp - eGFP \underset{k_{-ns}}{\overset{k_{ns}}{\Longleftrightarrow}} (DNA - Antp - eGFP)_{ns}$$
$$(DNA - Antp - eGFP)_{ns} + DNA_s \underset{k_{-s}}{\overset{k_s}{\Longleftrightarrow}} (DNA - Antp - eGFP)_s \quad \text{(S10).}$$

The turnover rate for the non-specific complex is:

$$\frac{d[(DNA-Antp-eGFP)_{ns}]}{dt} = k_{ns} \cdot [DNA_{ns}] \cdot [Antp - eGFP] - (k_{-ns} + k_s \cdot [DNA_s]) \cdot [(DNA - Antp - eGFP)_{ns}] + k_{-s} \cdot [(DNA - Antp - eGFP)_s] \quad \text{(S11).}$$

Assuming a quasi-steady state approximation:

$$\frac{d[(DNA-Antp-eGFP)_{ns}]}{dt} = 0 \quad \text{(S11),}$$

$$(k_{-ns} + k_s \cdot [DNA_s]) \cdot [(DNA - Antp - eGFP)_{ns}] = k_{ns} \cdot [DNA_{ns}] \cdot [Antp - eGFP] + k_{-s} \cdot [(DNA - Antp - eGFP)_s] \quad \text{(S12).}$$

Using the mass balance equation to express the concentration of the free TF:

$$[Antp - eGFP] = [Antp - eGFP]_0 - [(DNA - Antp - eGFP)_{ns}] - [(DNA - Antp - eGFP)_s] \quad \text{(S13)}$$

and assuming that:

$$[DNA]_{ns} \approx [DNA]_0 \quad \text{(S14),}$$

equation (S4) becomes:

$$(k_{-ns} + k_s \cdot [DNA_s]) \cdot [(DNA - Antp - eGFP)_{ns}] = k_{ns} \cdot [DNA]_0 \cdot [Antp - eGFP]_0 - [(DNA - Antp - eGFP)_{ns} - [(DNA - Antp - eGFP)_s] + k_{-s} \cdot [(DNA - Antp - eGFP)_s] \quad \text{(S15),}$$

$$(k_{-ns} + k_s \cdot [DNA_s] + k_{ns} \cdot [DNA]_0) \cdot [(DNA - Antp - eGFP)_{ns}] = k_{ns} \cdot [DNA]_0 \cdot ([Antp - eGFP]_0 - [(DNA - Antp - eGFP)_s]) + k_{-s} \cdot [(DNA - Antp - eGFP)_s] \quad \text{(S16),}$$

$$(k_{-ns} + k_s \cdot [DNA_s] + k_{ns} \cdot [DNA]_0) \cdot [(DNA - Antp - eGFP)_{ns}] = k_{ns} \cdot [DNA]_0 \cdot [Antp - eGFP]_0 - (k_{ns} \cdot [DNA]_0 - k_{-s}) \cdot [(DNA - Antp - eGFP)_s] \text{ (S17)},$$

$$[(DNA - Antp - eGFP)_{ns}] = \frac{k_{ns} \cdot [DNA]_0}{k_{-ns} + k_s \cdot [DNA_S] + k_{ns} \cdot [DNA]_0} \cdot [Antp - eGFP]_0 - \frac{k_{ns} \cdot [DNA]_0 - k_{-s}}{k_{-ns} + k_s \cdot [DNA_S] + k_{ns} \cdot [DNA]_0} \cdot [(DNA - Antp - eGFP)_s] \text{ (S18)}.$$

According to equation (S18) and the FCS data presented in Figure 4 – figure supplement 2, the slope of the linear dependence for

a) the short linker Antp isoform gives:

$$\frac{k_{ns} \cdot [DNA]_0}{k_{-ns} + k_s \cdot [DNA_S] + k_{ns} \cdot [DNA]_0} = 0.34 \text{ (S19)}$$

and the intercept:

$$\frac{k_{ns} \cdot [DNA]_0 - k_{-s}}{k_{-ns} + k_s \cdot [DNA_S] + k_{ns} \cdot [DNA]_0} \cdot [(DNA - Antp - eGFP)_s] = 5.31\ nM \text{ (S20)}.$$

If k_{-s} is small compared to $k_{ns} \cdot [DNA]_0$ and can therefore be neglected, then:

$$0.34 \cdot [(DNA - Antp - eGFP)_s] = 5.31\ nM \text{ (S21)}.$$

Thus, the concentration of specific complex between Antp-eGFP and DNA in the wing disc cell nuclei can be estimated to be:

$$[(DNA - Antp - eGFP)_s] = 15.62\ nM \text{ (S22)}.$$

The average concentration of free-diffusing Antp-eGFP molecules is determined as follows:

$$[Antp - eGFP]_{free} = [Antp - eGFP]_0 - [(DNA - Antp - eGFP)_{ns}] - [(DNA - Antp - eGFP)_s] = [Antp - eGFP]_0 - (0.34 \cdot [Antp - eGFP]_0 - 5.31) - [(DNA - Antp - eGFP)_s] = 785.28 - 0.34 \cdot 785.28 + 5.31 - 15.62 = 507.97nM \text{ (S23)}.$$

Using the experimentally determined concentration of specific DNA–Antp-eGFP complexes (equation (S22)), we could estimate the dissociation constant for the specific DNA–Antp-eGFP, as a function of the total concentration of specific Antp binding sites, to be:

$$K_{d,Antp}^{short\ linker} = \frac{[DNA_s]_{free} \cdot [Antp-eGFP]_{free}}{[(DNA-Antp-eGFP)_s]} = \frac{[DNA_s]_{free} \cdot 507.97}{15.62} \approx ([DNA_s]_{free} \cdot 32.52)\ nM \quad \text{(S24)}.$$

b) The long linker Antp isoform gives:

$$\frac{k_{ns} \cdot [DNA]_0}{k_{-ns} + k_s \cdot [DNA_s] + k_{ns} \cdot [DNA]_0} = 0.24 \quad \text{(S25)}.$$

and the intercept:

$$\frac{k_{ns} \cdot [DNA]_0 - k_{-s}}{k_{-ns} + k_s \cdot [DNA_s] + k_{ns} \cdot [DNA]_0} \cdot [(DNA - Antp - eGFP)_s] = 3.28\ nM \quad \text{(S26)}.$$

If k_{-s} is small compared to $k_{ns} \cdot [DNA]_0$ and can therefore be neglected, then:

$$0.24 \cdot [(DNA - Antp - eGFP)_s] = 3.28\ nM \quad \text{(S27)}.$$

Thus, the concentration of specific complex between Antp-eGFP and DNA in the wing disc cell nuclei can be estimated to be:

$$[(DNA - Antp - eGFP)_s] = 13.67\ nM \quad \text{(S28)}.$$

The average concentration of free-diffusing Antp-eGFP molecules is determined as follows:

$$[Antp - eGFP]_{free} = [Antp - eGFP]_0 - [(DNA - Antp - eGFP)_{ns}] - [(DNA - Antp - eGFP)_s] = [Antp - eGFP]_0 - (0.24 \cdot [Antp - eGFP]_0 - 3.28) - [(DNA - Antp - eGFP)_s] = 1382.95 - 0.24 \cdot 785.28 + 3.28 - 13.67 = 1040.65nM \quad \text{(S29)}.$$

Using the experimentally determined concentration of specific DNA–Antp-eGFP complexes (equation (S14)), we could estimate the dissociation constant for

the specific DNA–Antp-eGFP, as a function of the total concentration of specific Antp binding sites, to be:

$$K_{d,Antp}^{long\ linker} = \frac{[DNA_s]_{free} \cdot [Antp-eGFP]_{free}}{[(DNA-Antp-eGFP)_s]} = \frac{[DNA_s]_{free} \cdot 1040.65}{13.67} \approx ([DNA_s]_{free} \cdot 76.13)\ nM$$

(S30).

From equations (S24) and (S30), we could calculate the ratio of the apparent equilibrium dissociation constants to be:

$$\frac{K_{d,Antp}^{long\ linker}}{K_{d,Antp}^{short\ linker}} = \frac{[DNA_s]_{free}^{long\ linker} \cdot 76.13}{[DNA_s]_{free}^{short\ linker} \cdot 32.52} = 2.34 \cdot \frac{([DNA]_0 - [(DNA-Antp-eGFP)_s]_{long\ linker})}{([DNA]_0 - [(DNA-Antp-eGFP)_s]_{short\ linker})} =$$

$$2.34 \frac{[DNA]_0 - 13.67}{[DNA]_0 - 15.62}$$ (S31).

Therefore:

$$K_{d,Antp}^{long\ linker} > 2.34 \cdot K_{d,Antp}^{short\ linker}$$ (S32),

independently of the total concentration of Antp binding sites in the nucleus. For $[DNA]_0$ tending to $15.62\ nM$ ($[DNA]_0 \to 15.62\ nM$) with $[DNA]_0 > 15.62\ nM$, the ratio of the apparent equilibrium dissociation constants will be high:

$$\lim_{[DNA]_0 \to 15.62} \left(2.34 \frac{[DNA]_0 - 13.67}{[DNA]_0 - 15.62}\right) = +\infty$$ (S33),

indicating that the short linker isoform will bind the Antp binding sites with much higher affinity than the short linker isoform.

In contrast, for considerably higher values of $[DNA]_0$ ($[DNA]_0 \to +\infty$), the ratio of apparent equilibrium dissociation constants will be:

$$\lim_{[DNA]_0\to+\infty}\left(2.34\,\frac{[DNA]_0-13.67}{[DNA]_0-15.62}\right)=$$

$$\lim_{[DNA]_0\to+\infty}\left(2.34\,\frac{[DNA]_0\left(1-\frac{13.67}{[DNA]_0}\right)}{[DNA]_0\left(1-\frac{15.62}{[DNA]_0}\right)}\right)=\lim_{[DNA]_0\to+\infty}\left(2.34\,\frac{1-\frac{13.67}{[DNA]_0}}{1-\frac{15.62}{[DNA]_0}}\right)=2.34 \quad \text{(S34)},$$

indicating a roughly 2.5fold higher affinity of the short linker repressive isoform. This means that, with decreasing total amounts of available Antp binding sites, the short linker repressing Antp isoform will bind with even higher affinity than its long linker counterpart.

Supplement 4: Stochastic modeling of Antennapedia expression

In the following, we develop a simple mathematical model that is able to explain the behavior of Antennapedia (Antp) expression at early and late developmental stages. The Antp promoter is modeled as a continuous-time Markov chain with three distinct transcriptional states. In the absence of Antp, the promoter is in an unbound state ("U"), in which transcription is inactive. From this state, the promoter can switch to a transcriptionally active state "A" at a rate, assumed to be proportional to the concentration of the long-linker, activating isoform of Antp. Analogously, repression of the promoter by the short-linker isoform of Antp is modeled by an additional transcriptionally weak state "R", which can be reached from state "U" at a rate proportional to the concentration of that isoform. The corresponding reverse transitions from states "R" and "A" back into state "U" are assumed to happen at a constant rate k. Since the activating isoform can potentially also repress the promoter, we assume that state "R" can be reached also from the active state "A". Similarly, we model a potential link also in the reverse direction from state "A" to "R". Depending on the model variant, we assume this transition happens either at a constant rate k (competitive promoter model) or at a rate proportional to

the concentration of the repressing isoform of Antp (non-competitive promoter model). In the latter case, repression through short-linker isoforms can take place even if a long-linker isoform is already bound to the promoter. As we have demonstrated in Figure 5 A and B, the two model variants yield qualitative differences in Antp expression. For the sake of illustration, the following description focuses on the non-competitive model variant but we remark that the competitive model can be derived analogously.

At a particular time point t, the transcription rate of Antp is determined by the current state of the promoter, i.e., $\lambda(t)\epsilon\{0, \lambda_A, \lambda_B\}$, with λ_A and λ_B as the transcription rates associated with states "A" and "R", respectively. In line with our experimental findings, we assume that transcripts are spliced into the activating and repressing isoforms at different rates ρ_A and ρ_R, respectively. This allows us to capture the imbalance between the two isoforms that was revealed by our FCS data. The overall expression rates for the two isoforms of Antp are then given by $h_A(t) = \lambda(t)Z\rho_A$ and $h_R(t) = \lambda(t)Z\rho_R$, whereas Z is a random variable that accounts for extrinsic variability in gene expression rates (Zechner et al., 2012). In all of our analyses, we model Z as a Gamma random variable, i.e., $Z \sim \Gamma(\alpha, \beta)$ with α and β as shape and inverse scale parameters of that distribution. In summary, we describe the auto-regulatory circuit of Antp expression by a stochastic reaction network of the form:

$$U \underset{k}{\overset{\gamma_A X_A(t)}{\rightleftarrows}} A$$

$$U \underset{k}{\overset{\gamma_R X_R(t)}{\rightleftarrows}} \mathrm{R}$$

$$A \underset{k}{\overset{\gamma_R X_R(t)}{\rightleftarrows}} \mathrm{R}$$

$$\emptyset \xrightarrow{h_A(t)} X_A \xrightarrow{1/\tau} \emptyset$$

$$\emptyset \xrightarrow{h_R(t)} X_R \xrightarrow{1/\tau} \emptyset$$

(S35),

with $X_A(t)$and $X_R(t)$ as the concentration of the activating and repressing isoforms of Antp and τ as the protein half-live. The initial conditions $X_A(0)$ and $X_R(0)$ were drawn randomly in accordance with our concentration measurements at early stages. In particular, we assume that the total amount of Antp X_{tot} in each cell is drawn from a negative binomial distribution such that $X_{tot} \sim \mathcal{N}B(r,p)$, with r and p as the parameters characterizing this distribution. The total number of Antp molecules was then randomly partitioned into fractions of repressing and activating isoforms according to a Beta distribution. More specifically, we set $X_A(0) = WX_{tot}$ and $X_R(0) = (1-W)X_{tot}$ with $W \sim Beta(a,b)$. The parameters r, p, a and b were chosen based on our experimental data (see Table 1).

Due to the fact that Antp expression takes place at the timescale of hours, we can further simplify our model from (S35). In particular, we can make use of a quasi-steady state assumption (Rao and Arkin, 2003), taking into consideration that promoter switching due to binding and unbinding of the different Antp isoforms occurs at a much faster timescale than production and degradation of Antp. As a consequence, we can replace the stochastic gene expression rates of the two isoforms by their expected value, whereas the expectation is taken with respect to the quasi-stationary distribution of the three state promoter model. More precisely, we have:

$$h_A(t) \approx \mathbb{E}[\lambda(t)]Z\rho_A$$

$$h_R\,(t) \approx \mathbb{E}[\lambda(t)]Z\rho_R$$

1855 (S36),

1856 with $\mathbb{E}[\lambda(t)] = P_U 0 + P_A\lambda_A + P_R\lambda_R$ as the quasi-stationary probabilities of finding the
1857 promoter in state "U", "A" and "R", respectively. These probabilities can be derived
1858 from the generator matrix of the three-state promoter model, which reads:

1859 $$Q = \begin{pmatrix} -\gamma_A X_A(t) - \gamma_R X_R(t) & k & k \\ \gamma_A X_A(t) & -k - \gamma_R X_R(t) & k \\ \gamma_R X_R(t) & \gamma_R X_R(t) & -2k \end{pmatrix}$$ (S37).

1860 Assuming that $X_A(t)$ and $X_R(t)$ remain roughly constant on the timescale of the
1861 promoter, the quasi-stationary distribution can be determined by the null-space of Q,
1862 which in this case is given by:

1863 $$P_{QSS} = \begin{pmatrix} P_U \\ P_A \\ P_R \end{pmatrix} = \begin{pmatrix} \frac{k}{(k+\gamma_A X_A(t)+\gamma_R X_R(t))} \\ \frac{k(2\gamma_A X_A(t)+\gamma_R X_R(t))}{(2k+\gamma_R X_R(t))(k+\gamma_A X_A(t)+\gamma_R X_R(t))} \\ \frac{\gamma_R X_R(t)}{2k+\gamma_R X_R(t)} \end{pmatrix}$$ (S38).

1864 Correspondingly, the expectation of $\lambda(t)$ becomes:

$$\mathbb{E}[\lambda(t)] = (0 \quad \lambda_A \quad \lambda_R)\begin{pmatrix} P_U \\ P_A \\ P_R \end{pmatrix}$$

$$= \frac{\gamma_R X_R(t)\lambda_R}{2k + \gamma_R X_R(t)} + \frac{k\lambda_A\big(2\gamma_A X_A(t) + \gamma_R X_R(t)\big)}{\big(2k + \gamma_R X_R(t)\big)\big(k + \gamma_A X_A(t) + \gamma_R X_R(t)\big)}$$

1865 $$:= \bar{\lambda}(X_A(t), X_R(t))$$ (S39).

1866 The simplified model of Antp expression can then be compactly written as:

$$\emptyset \xrightarrow{\bar{h}_A(X_A(t),X_R(t))} X_A \xrightarrow{1/\tau} \emptyset$$

$$\emptyset \xrightarrow{\bar{h}_R(X_A(t),X_R(t))} X_R \xrightarrow{1/\tau} \emptyset$$

(S40),

with $\bar{h}_A(X_A(t),X_R(t)) = \bar{\lambda}(X_A(t),X_R(t))Z\rho_A$ and $\bar{h}_R(X_A(t),X_R(t)) = \bar{\lambda}(X_A(t),X_R(t))Z\rho_R$.

In all our simulation studies, the circuit from (S40) was simulated using the stochastic simulation algorithm (SSA) (Gillespie, 2007). In case of the perturbation experiments, small modifications to the model were made. In case of overexpressing either of the two isoforms, additional reactions of the form:

$$\emptyset \xrightarrow{\lambda_O} X_A \text{ (S41)}$$

and

$$\emptyset \xrightarrow{\lambda_O} X_A \text{ (S42)}$$

were included in the model. To account for overexpression of an external repressor S, we introduced a fourth state in the promoter model, from which no expression can take place. This state is assumed to be reachable from any of the other three states at a rate $\gamma_S S$ with S as the concentration of the external repressor. The corresponding reaction rates of Antp expression were determined analogously to equations (S37-S39). Table 1 summarizes the parameters used for each of the simulation studies.

Table 1: Parameters used for simulating the stochastic model of Antp expression

Parameter	r	p	a	b	τ	k	γ_A	γ_R	λ_A	λ_R	α	β	λ_O	γ_S	S
Unit	–	–	–	–	h	s^{-1}	s^{-1}	s^{-1}	s^{-1}	s^{-1}	–	–	s^{-1}	–	–
Figure 5 A, D, E and F	2.5	1.0	18	12	12[a]	100	0.25	1	10	0.1	3	0.33	–	–	–

Figure 5 B	2.5	1.0	18	12	12	100	0.25	1	10	0.1	3	0.33	–	–	–
Figure 5 C	2.5	1.0	18	12	12	100	0.25	0	0.5[b]	–	3	0.33	–	–	
Figure 5 G[c]	2.5	1.0	18	12	12	100	0.25	1	10	0.1	3	0.33	10	–	–
Figure 5 H[d]	2.5	1.0	18	12	12	100	0.25	1	10	0.1	3	0.33	10	–	–
Figure 5 M	2.5	1.0	18	12	12	100	0.25	1	10	0.1	3	0.33	10	1	4e4

[a]Experimentally determined value from (Dworkin et al., 2007).

[b]The expression rate λ_A was chosen to achieve average Antp levels similar to those of Figure 5 A (i.e., around 6000 molecules).

[c]Overexpression of X_R.

[d]Overexpression of X_A.

Figure 1

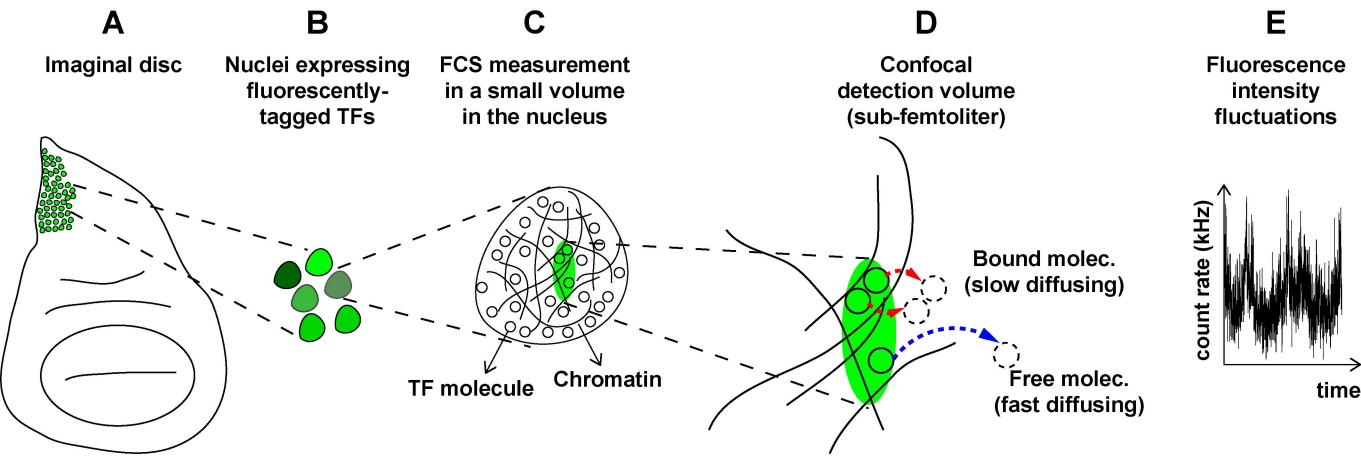

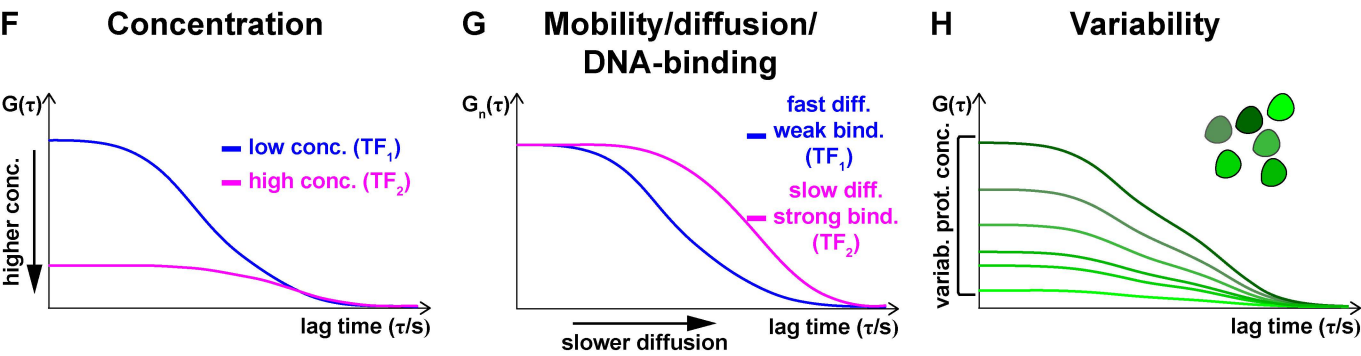

All TFs

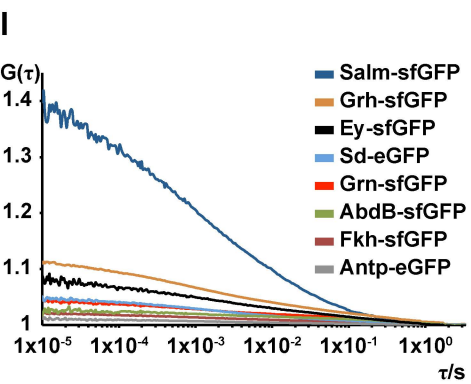

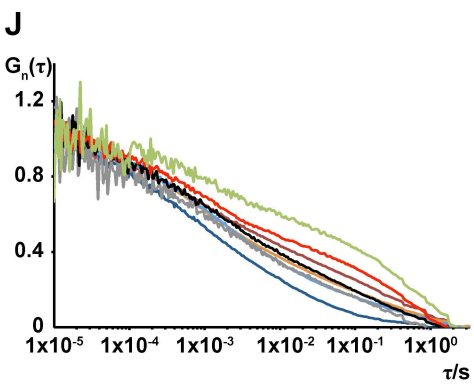

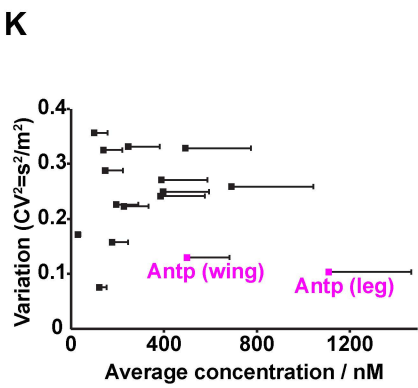

Antennapedia (Antp)

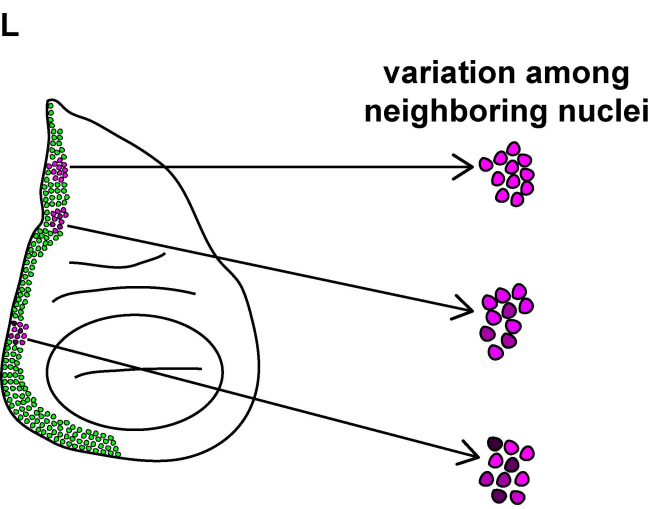

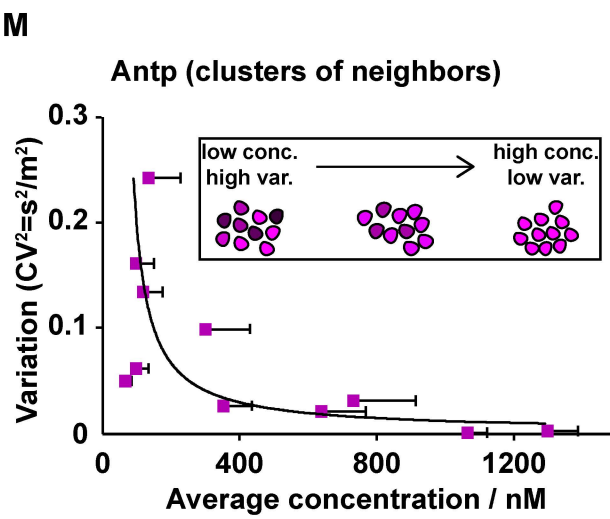

Figure 1 - figure supplement 1

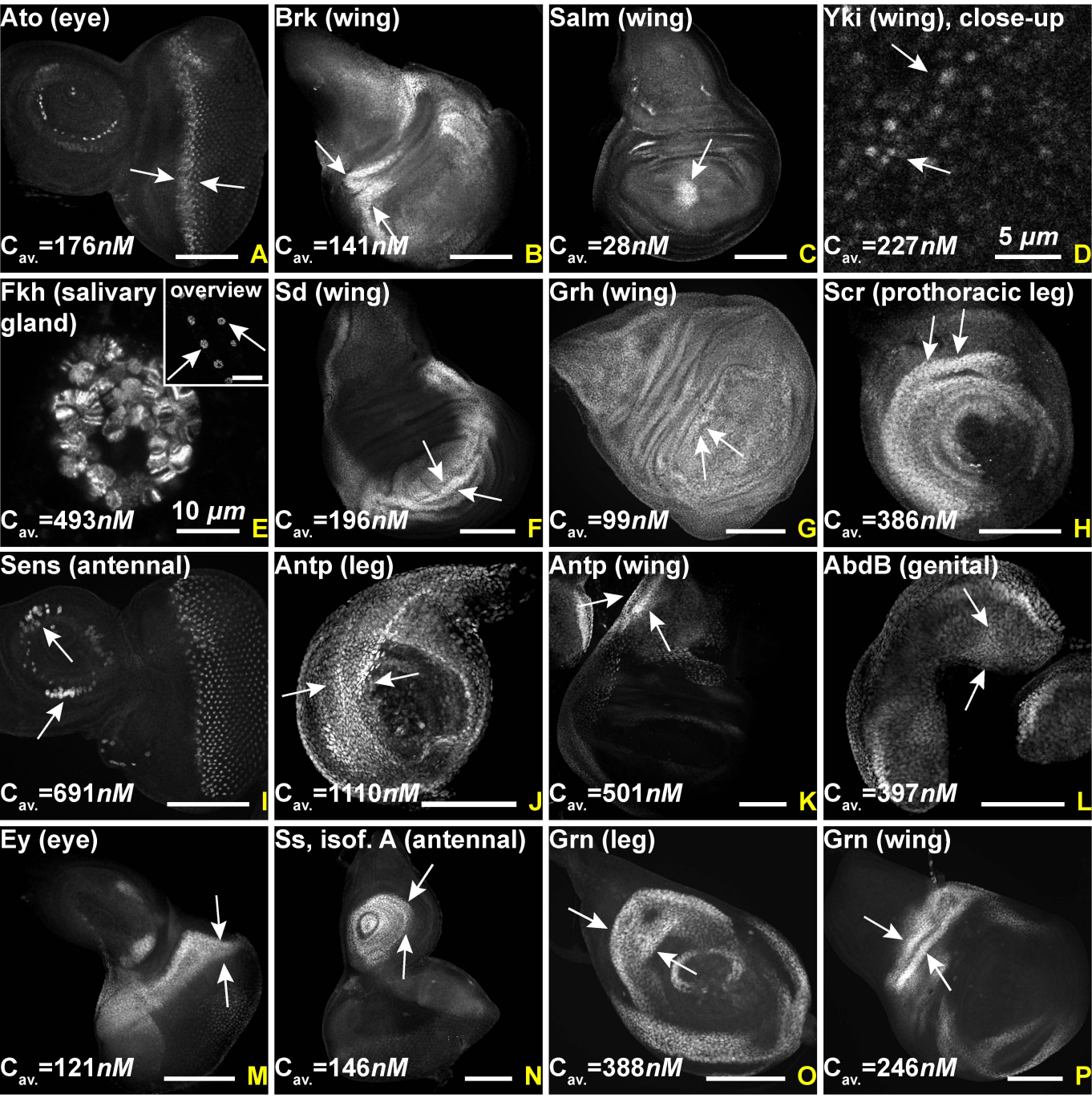

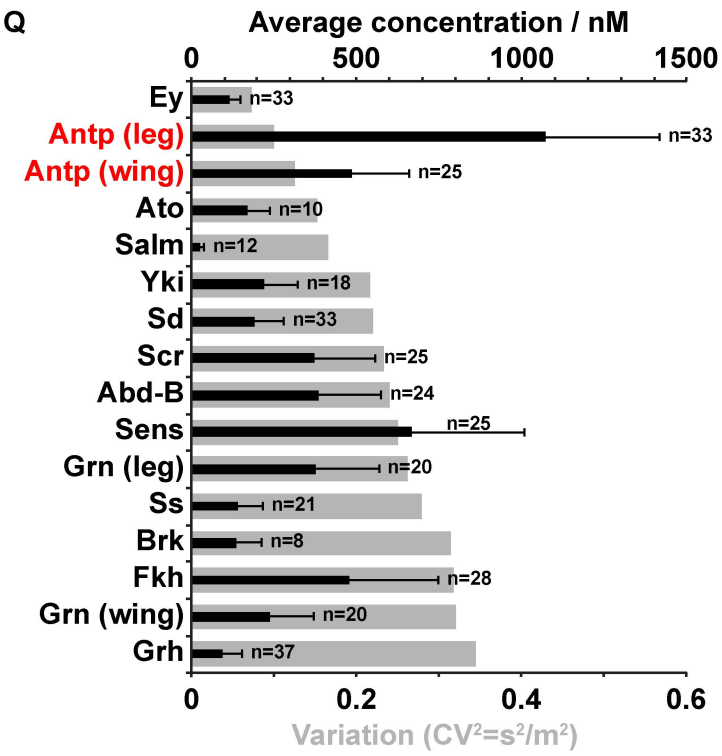

Figure 1 - figure supplement 2

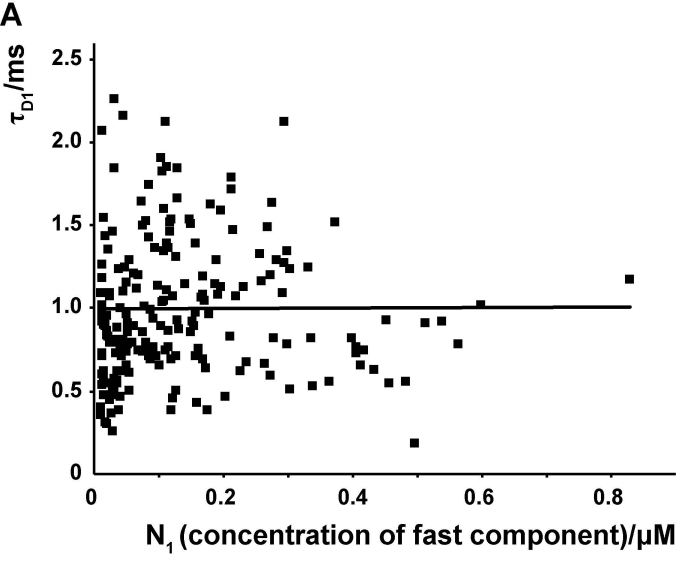

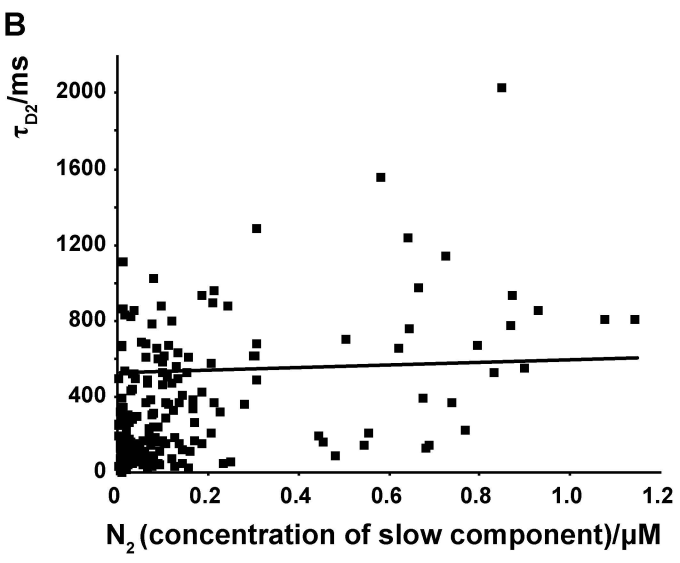

Figure 2

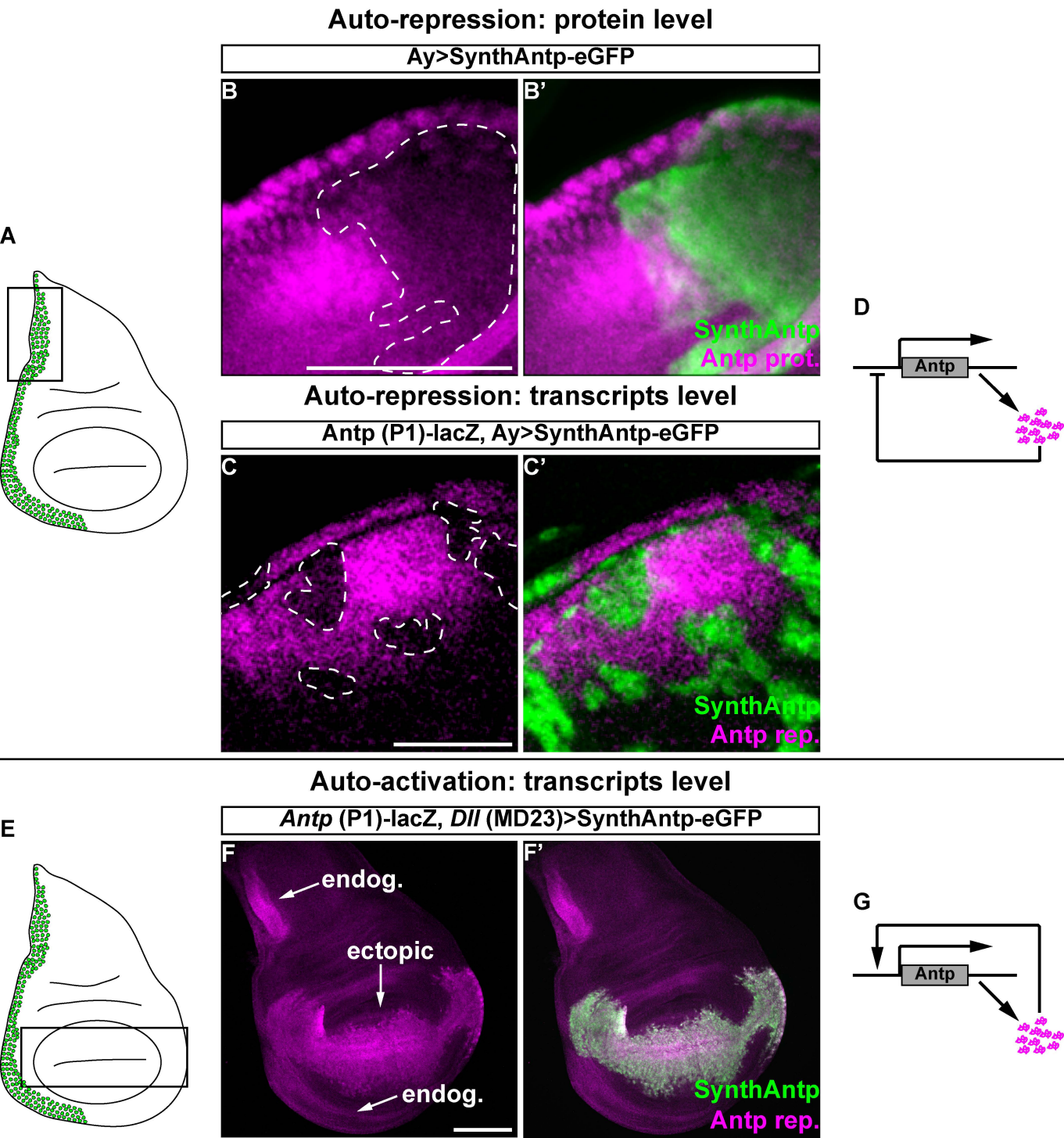
Auto-repression: protein level
Ay>SynthAntp-eGFP
B
B'
SynthAntp
Antp prot.
A
D
Antp
Auto-repression: transcripts level
Antp (P1)-lacZ, Ay>SynthAntp-eGFP
C
C'
SynthAntp
Antp rep.
Auto-activation: transcripts level
Antp (P1)-lacZ, Dll (MD23)>SynthAntp-eGFP
E
F
F'
endog.
ectopic
endog.
SynthAntp
Antp rep.
G
Antp

Figure 2 - figure supplement 1

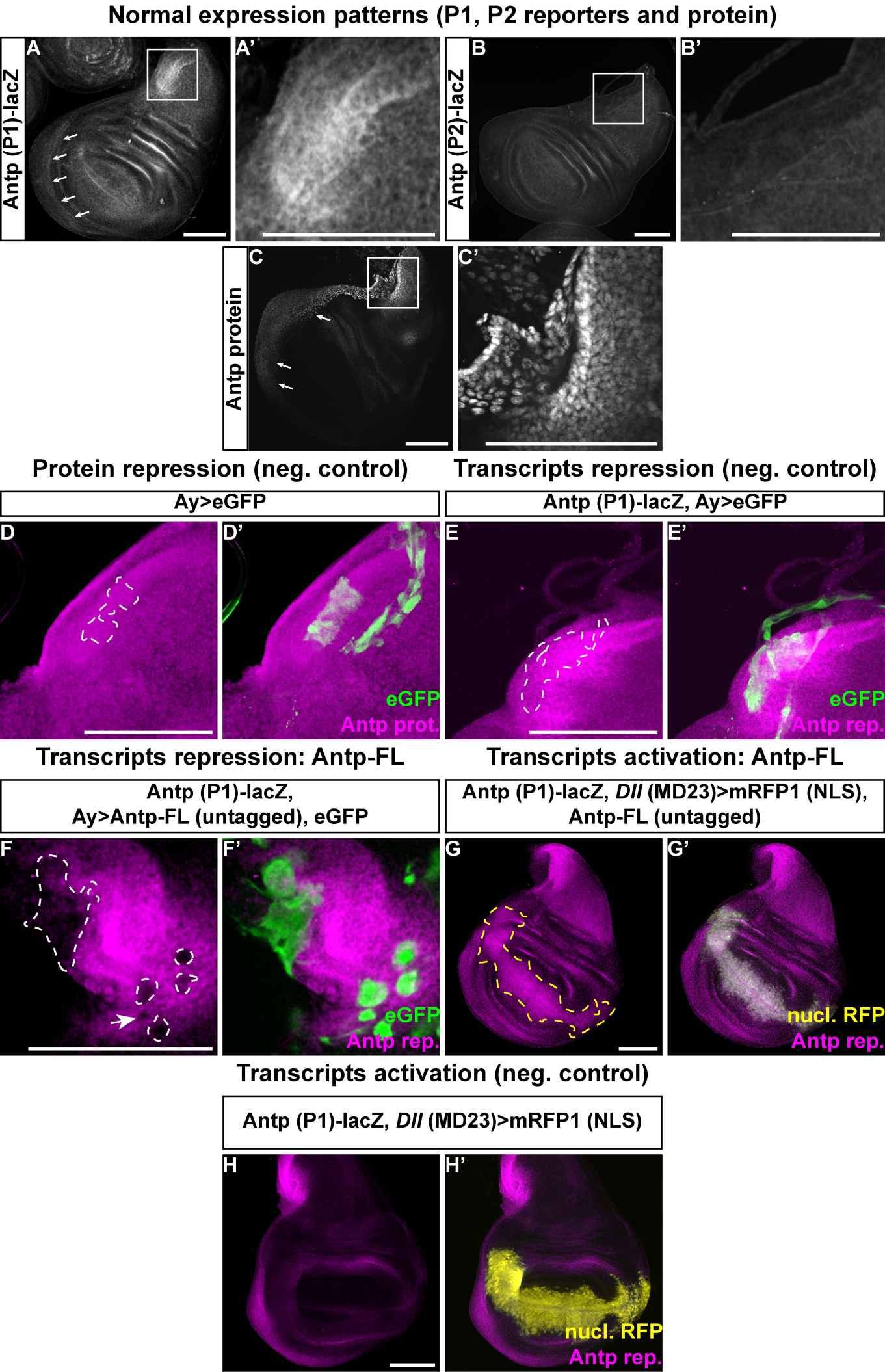

Figure 2 - figure supplement 2

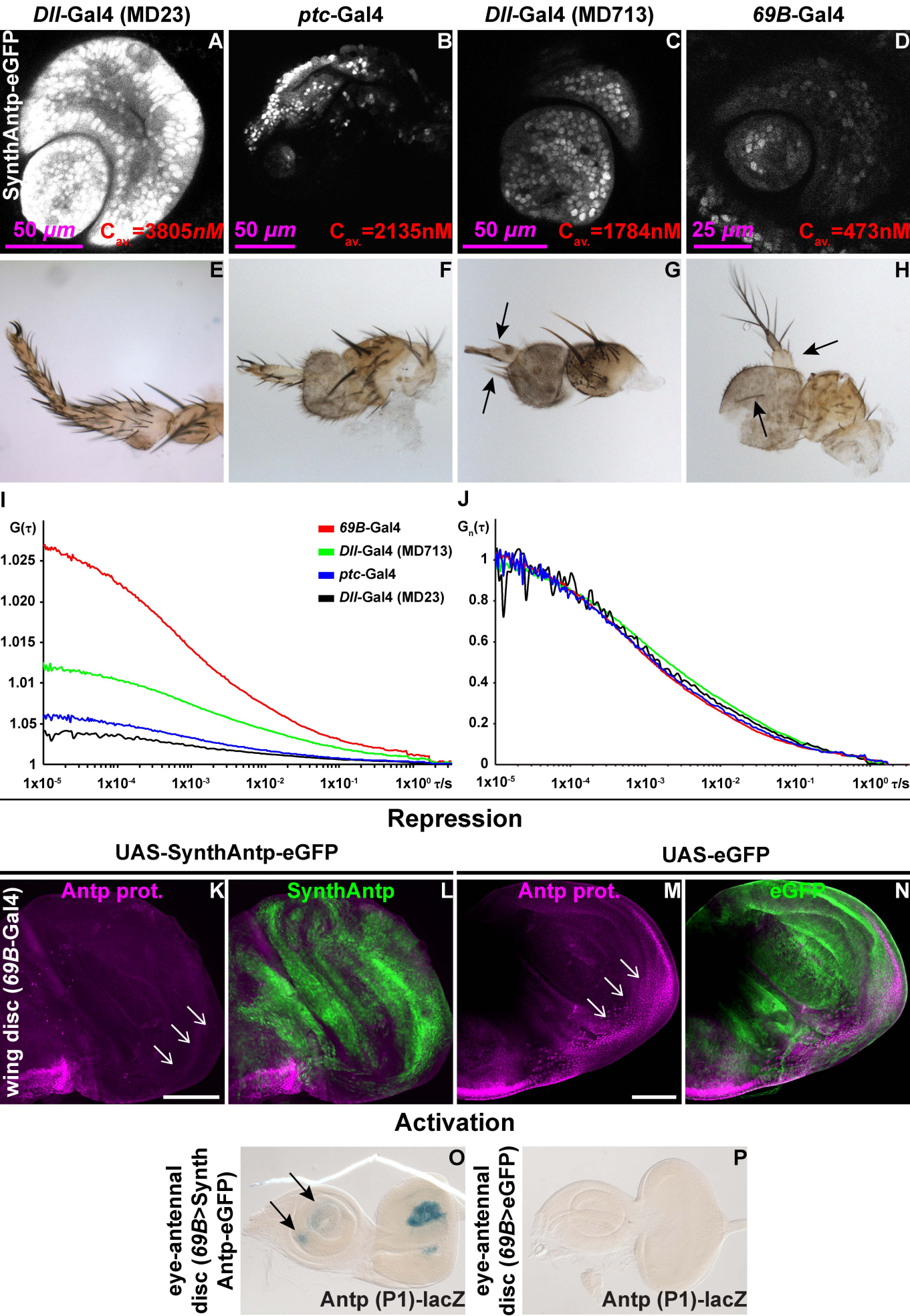

Figure 2 - figure supplement 3

Endogenous versus overexpressed

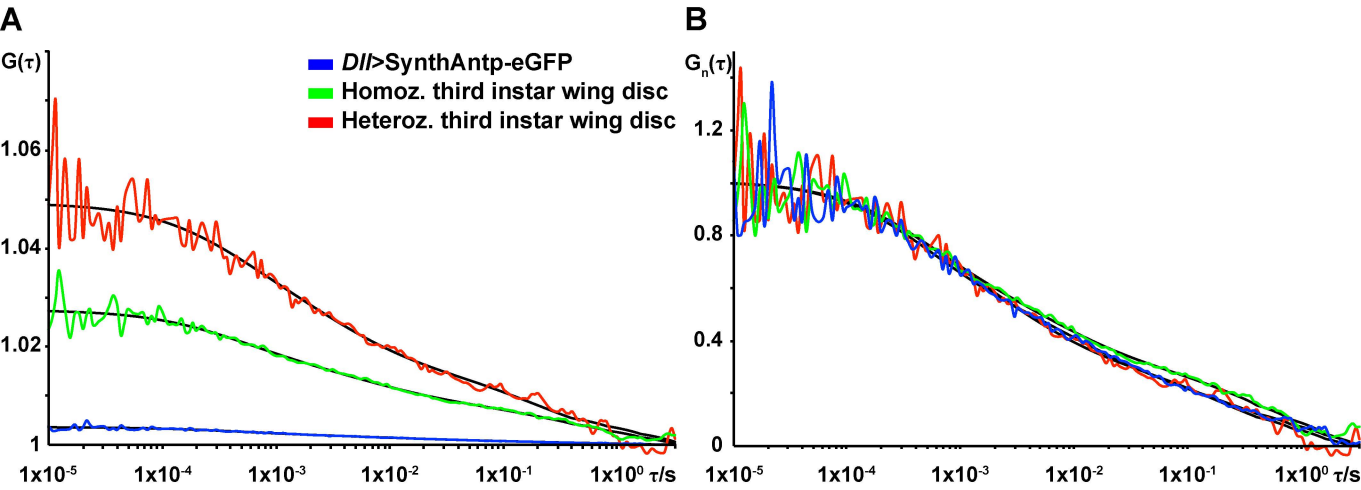

Figure 3

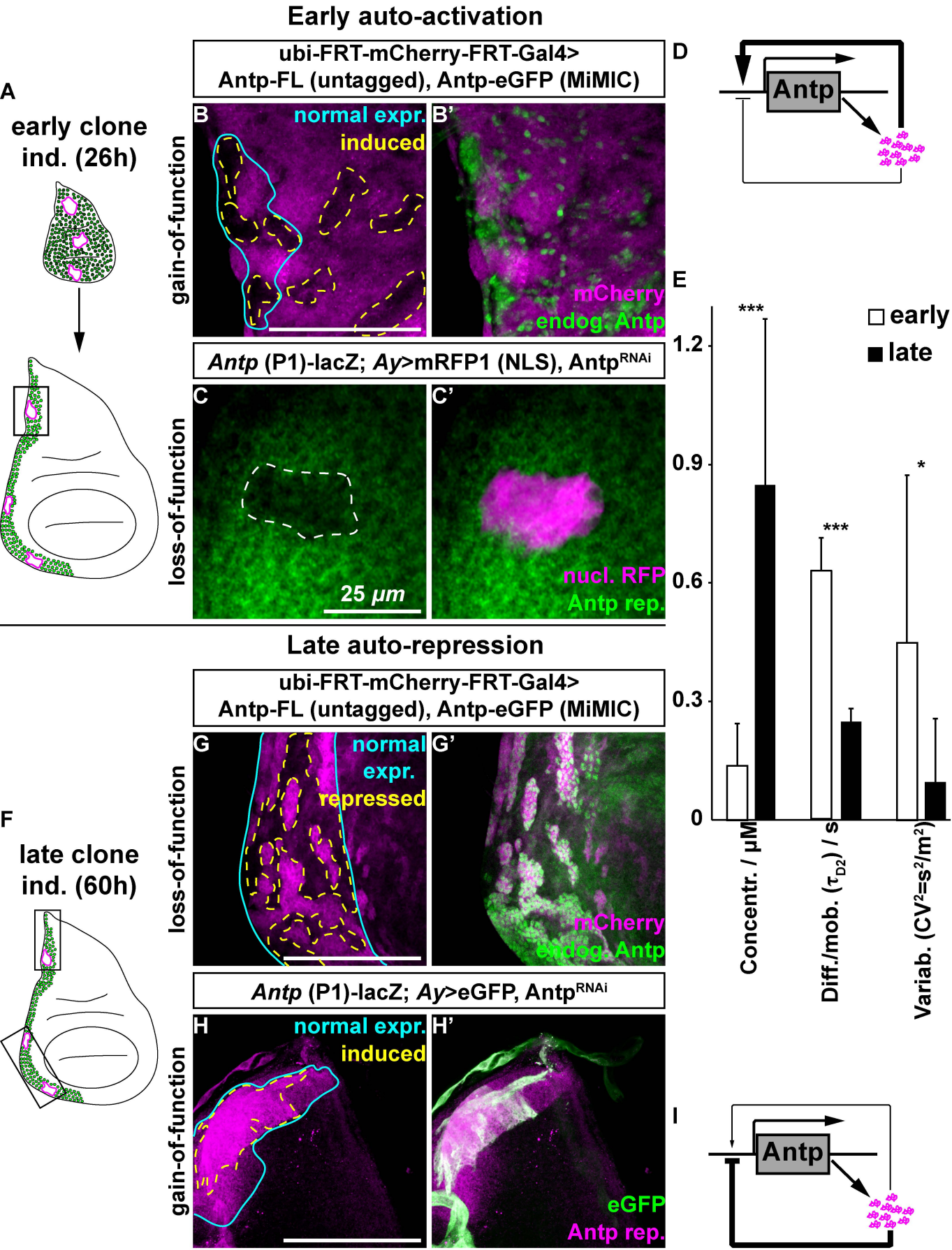
Early auto-activation
ubi-FRT-mCherry-FRT-Gal4>
Antp-FL (untagged), Antp-eGFP (MiMIC)
A
early clone
ind. (26h)
gain-of-function
B
normal expr.
induced
B'
mCherry
endog. Antp
D
Antp
Antp (P1)-lacZ; Ay>mRFP1 (NLS), Antp^RNAi
loss-of-function
C
C'
25 µm
nucl. RFP
Antp rep.
E
early
late
***
***
*
1.2
0.9
0.6
0.3
0
Concentr. / µM
Diff./mob. (τD2) / s
Variab. (CV²=s²/m²)
Late auto-repression
ubi-FRT-mCherry-FRT-Gal4>
Antp-FL (untagged), Antp-eGFP (MiMIC)
F
late clone
ind. (60h)
loss-of-function
G
normal
expr.
repressed
G'
mCherry
endog. Antp
Antp (P1)-lacZ; Ay>eGFP, Antp^RNAi
gain-of-function
H
normal expr.
induced
H'
eGFP
Antp rep.
I
Antp

Figure 3 - figure supplement 1

A

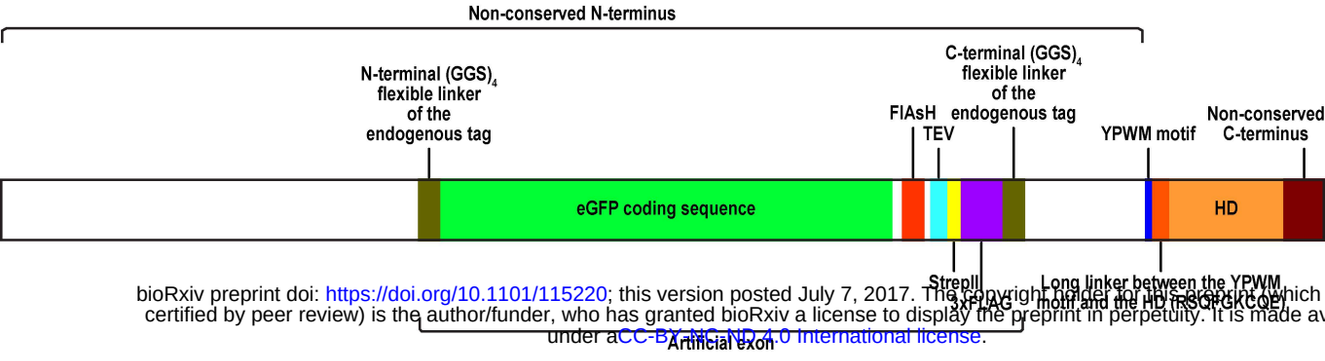

B

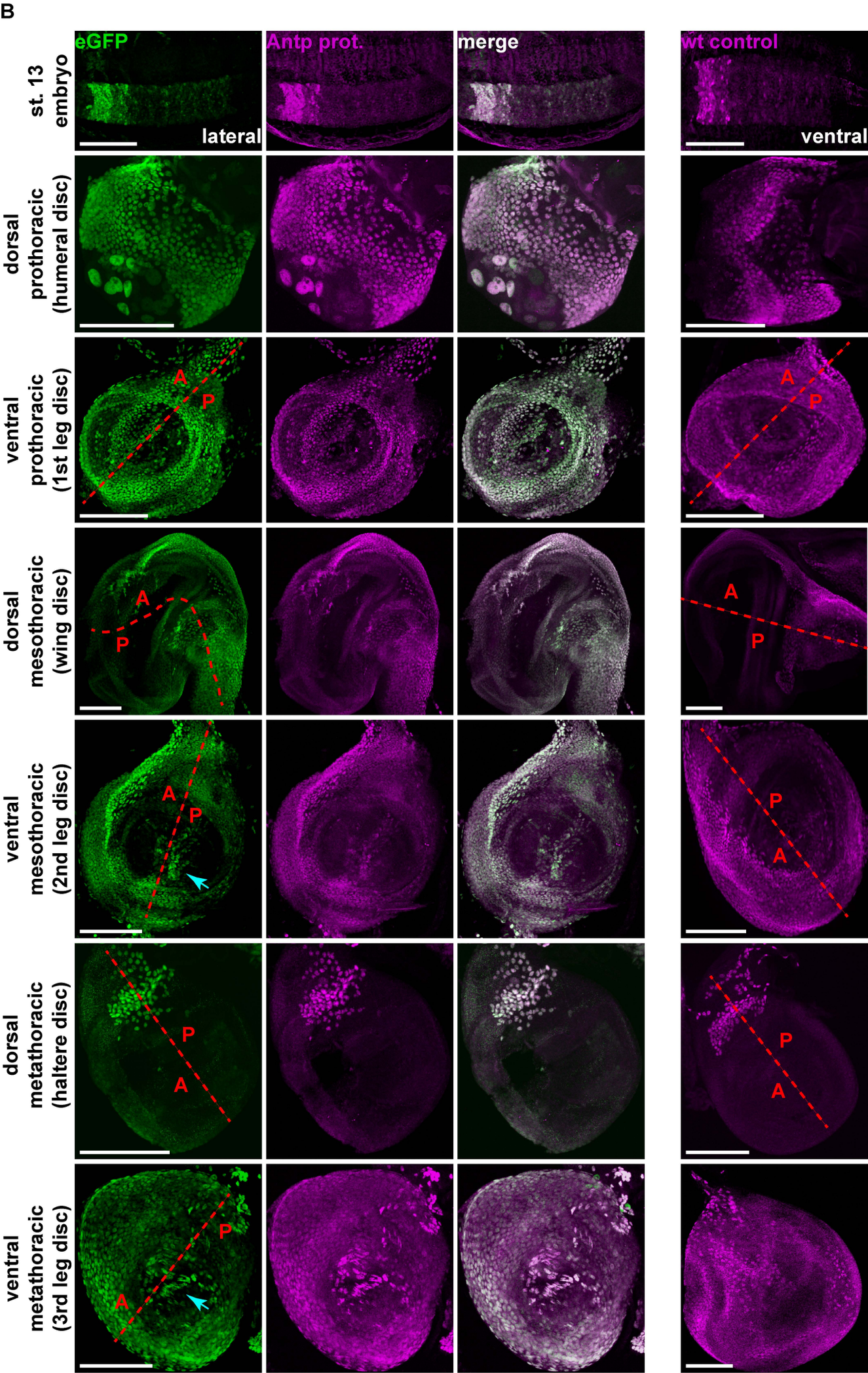

Figure 3 - figure supplement 2

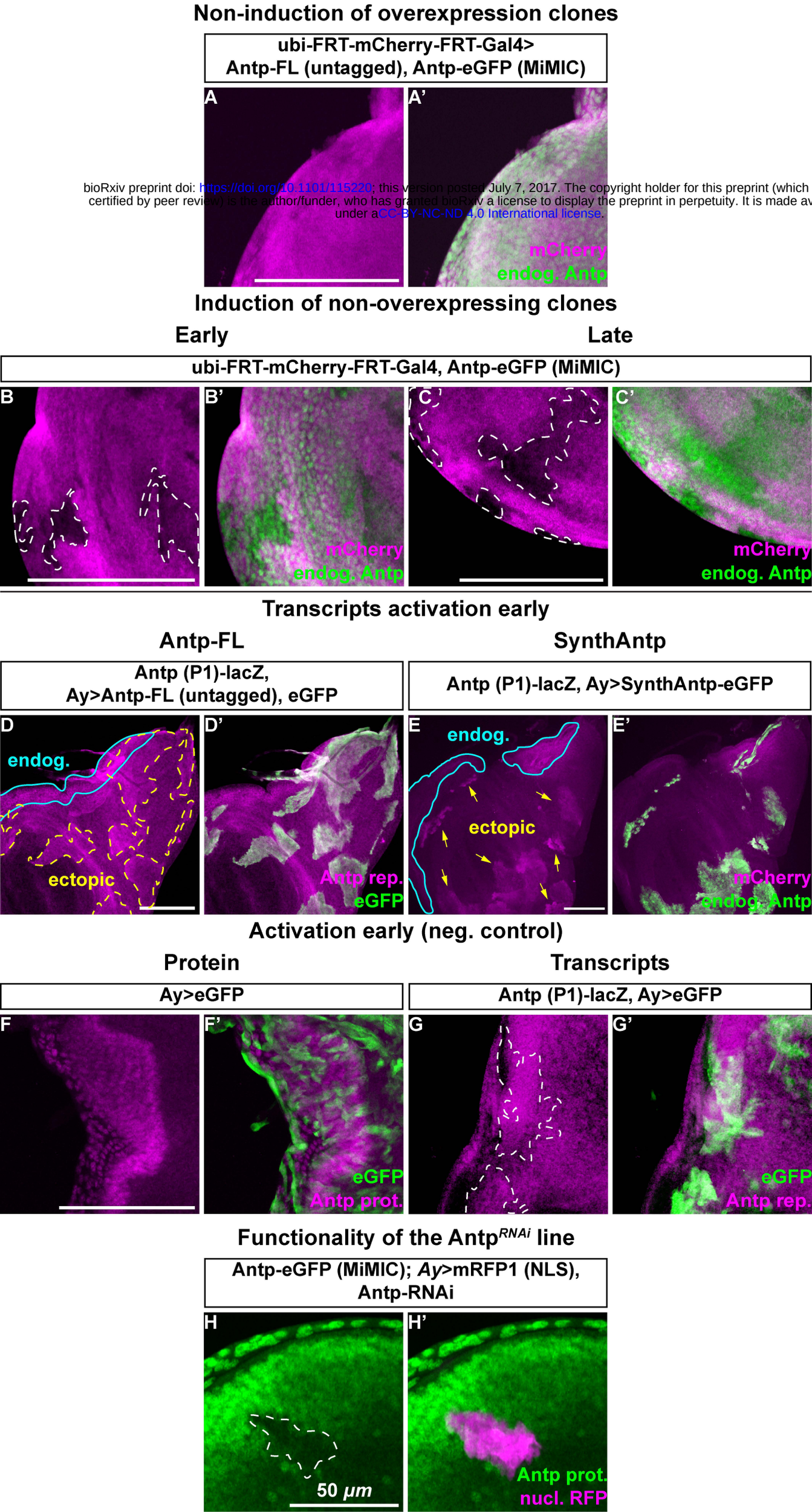

Figure 3 - figure supplement 3

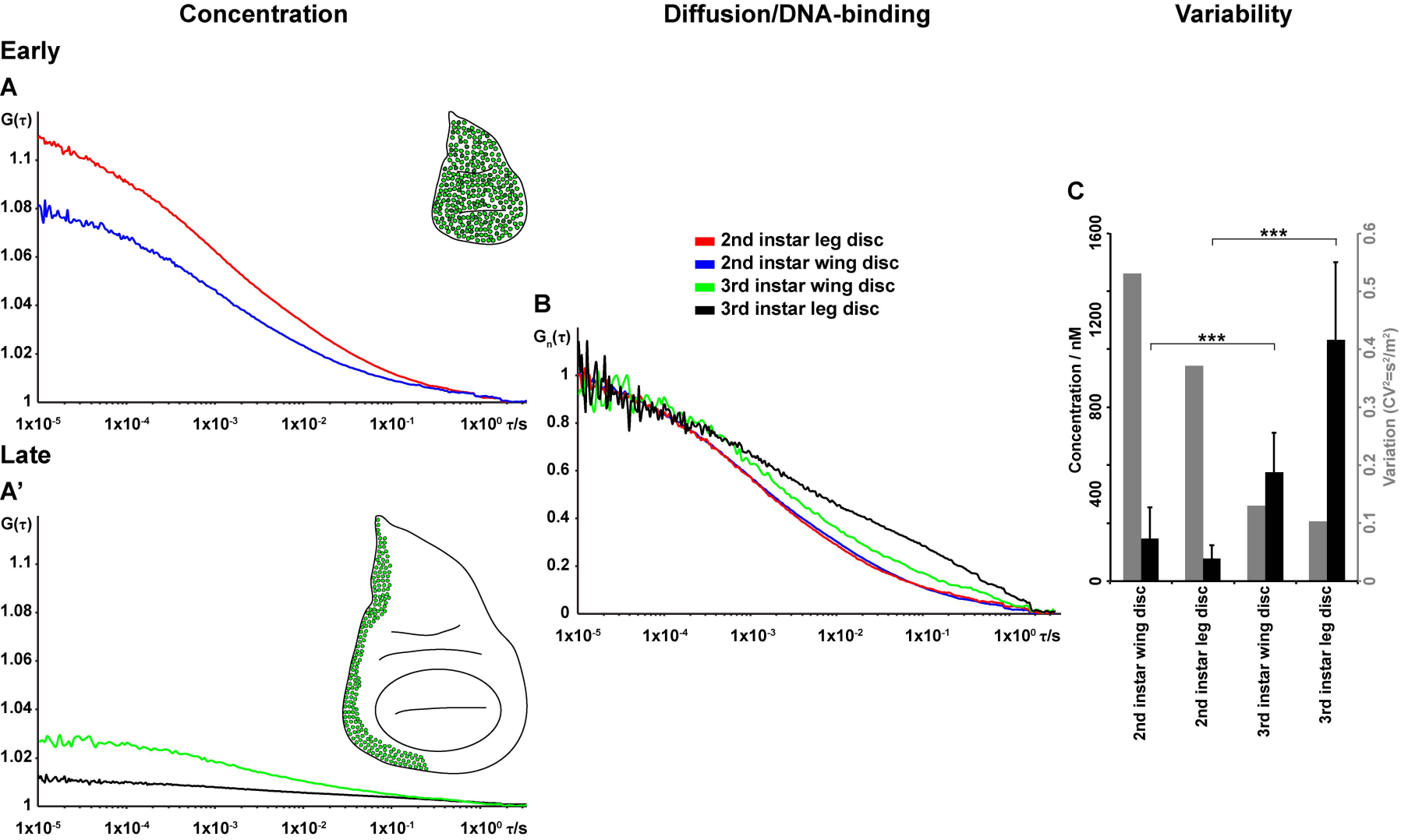

Figure 4

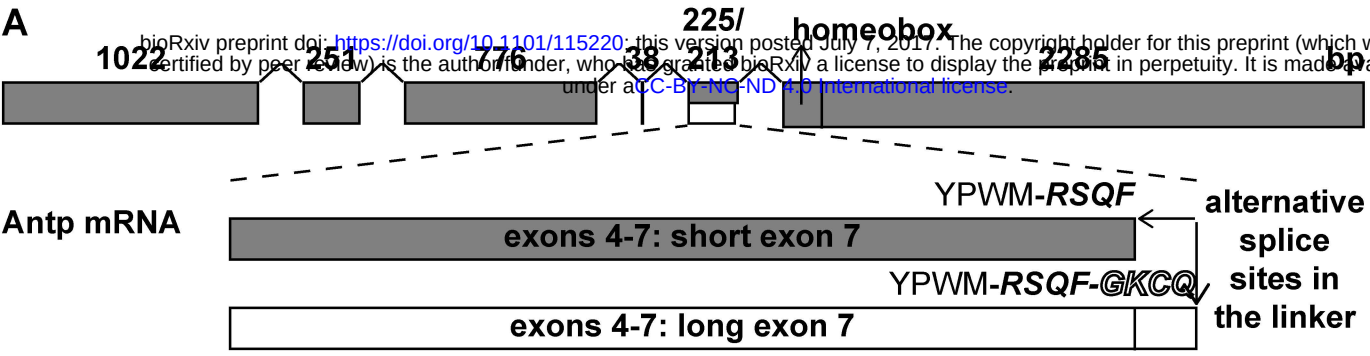

Long linker isoform (preferential activator)

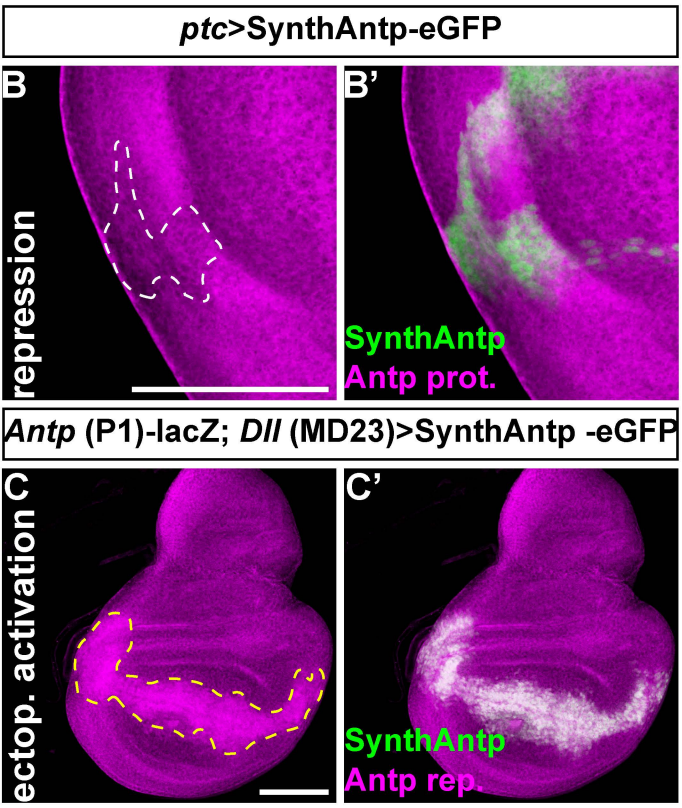

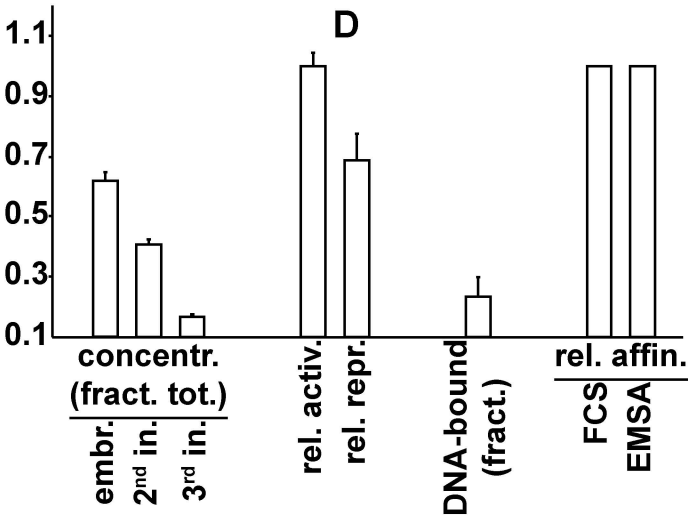

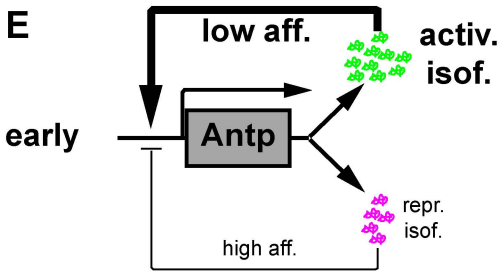

Short linker isoform (preferential repressor)

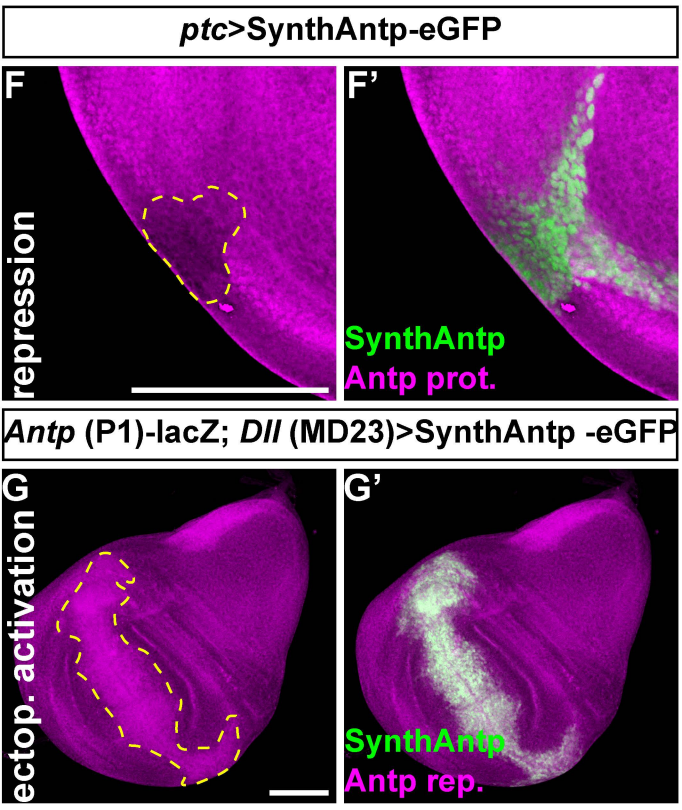

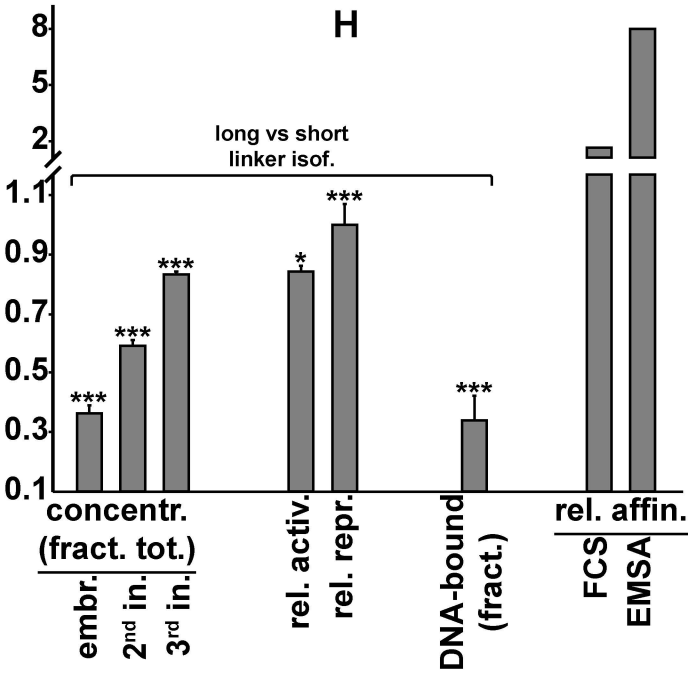

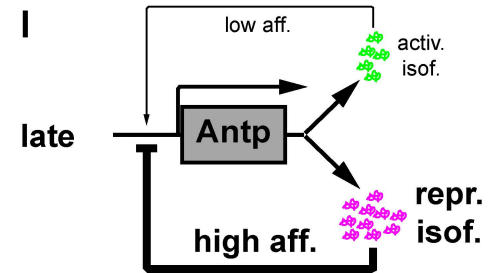

Figure 4 - figure supplement 1

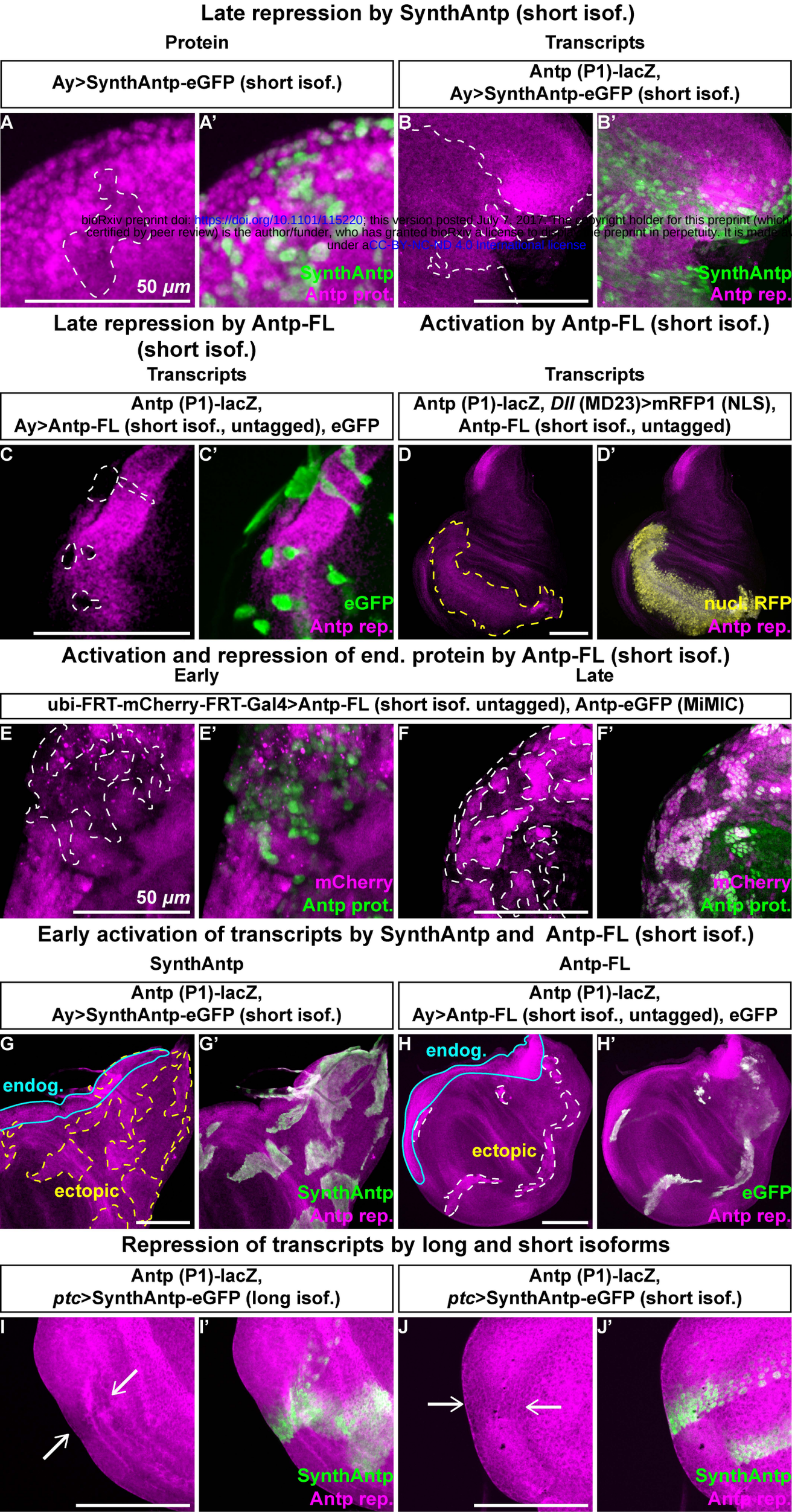

Figure 4 - figure supplement 2

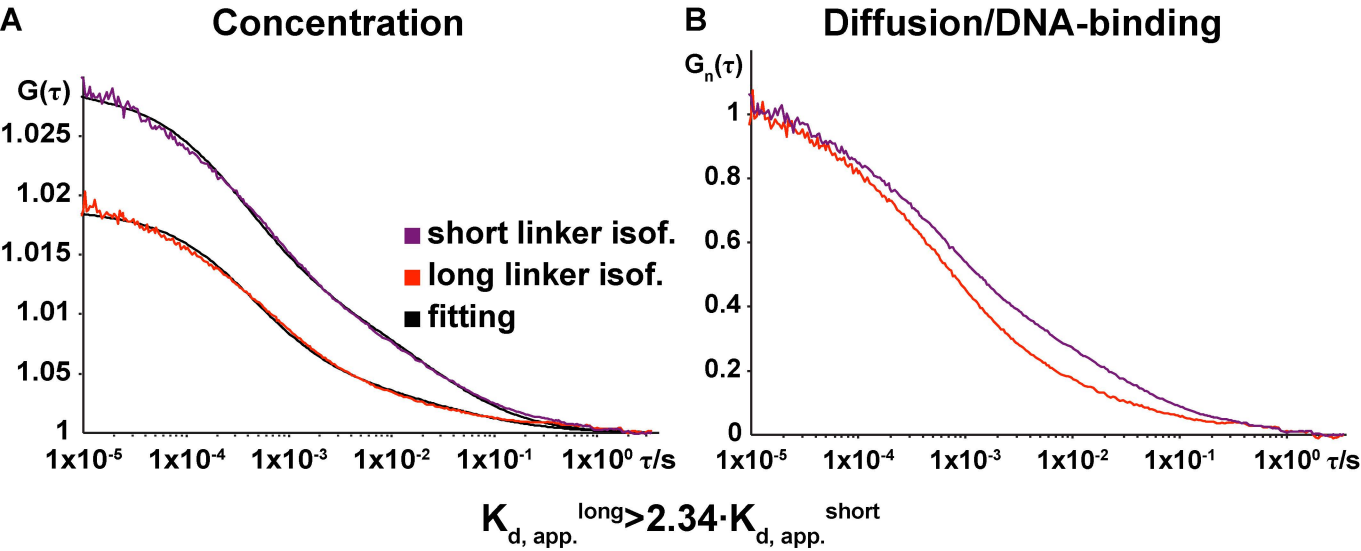

$K_{d,\,app.}^{long} > 2.34 \cdot K_{d,\,app.}^{short}$

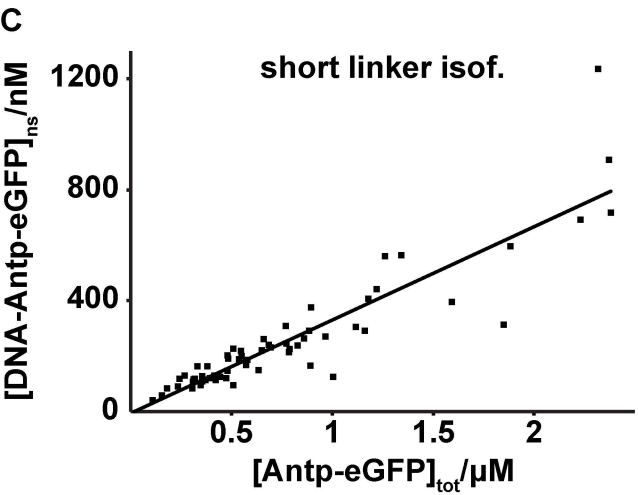

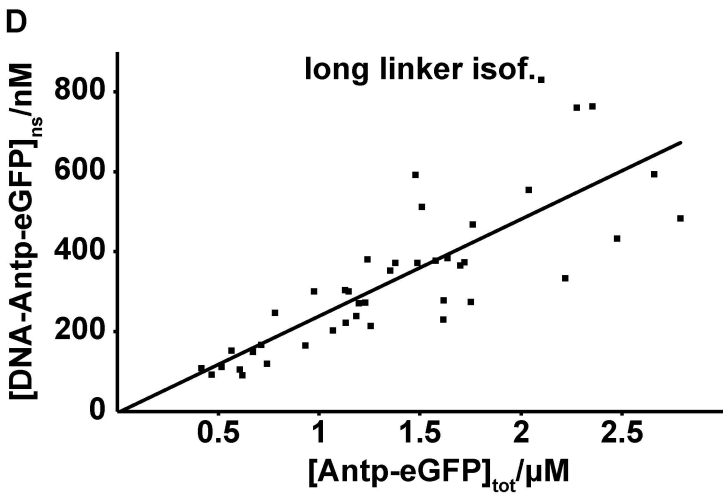

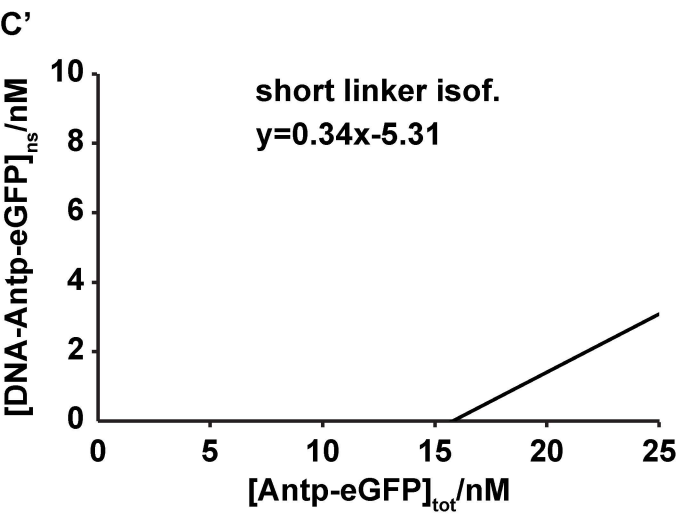

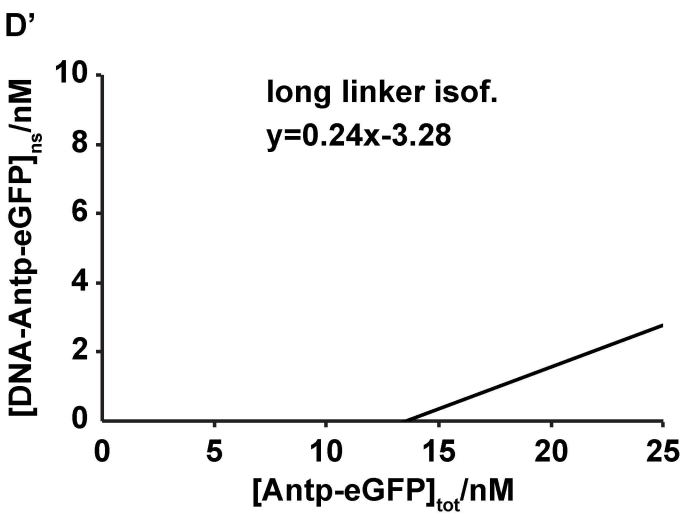

Figure 4 - figure supplement 3

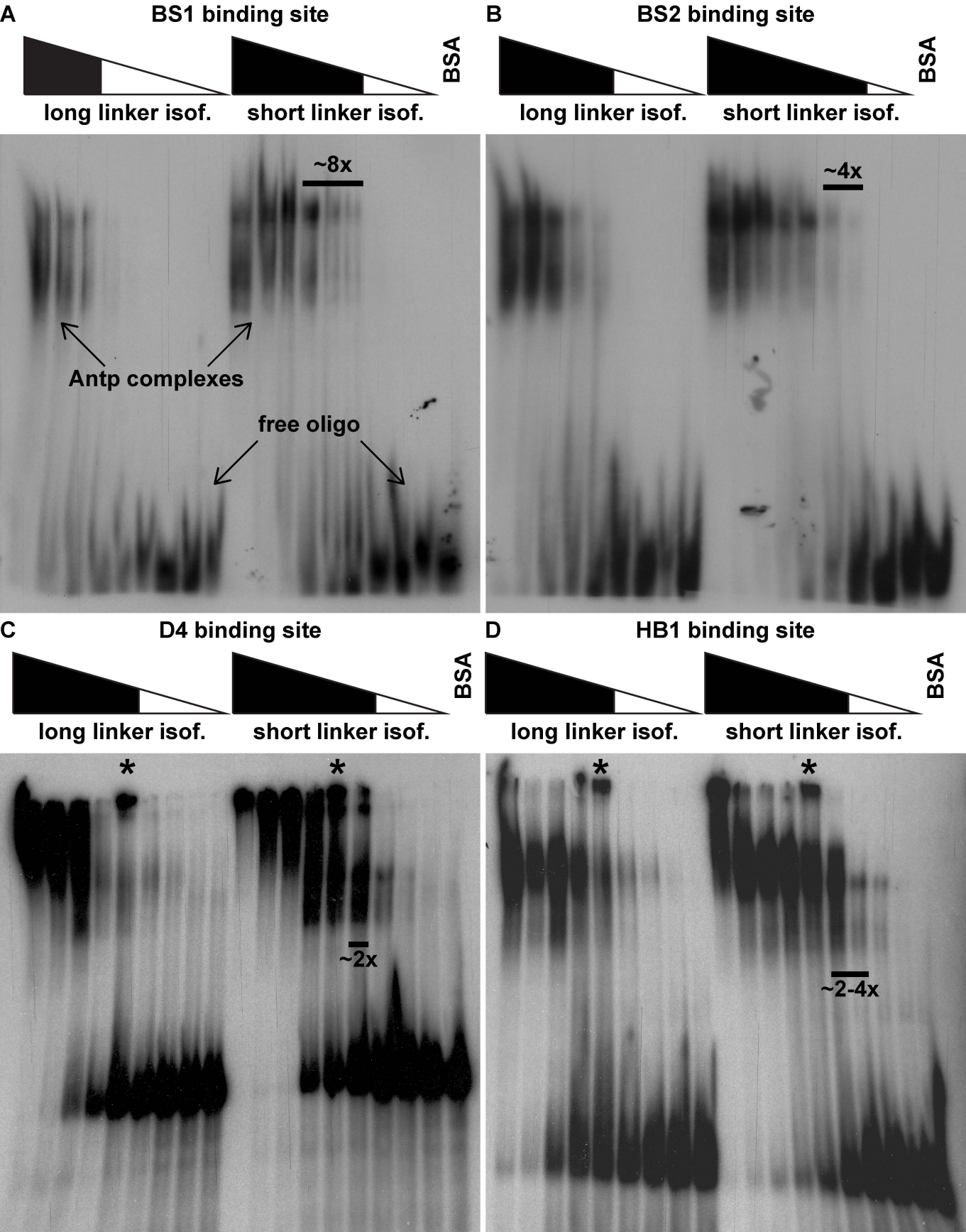

Figure 5

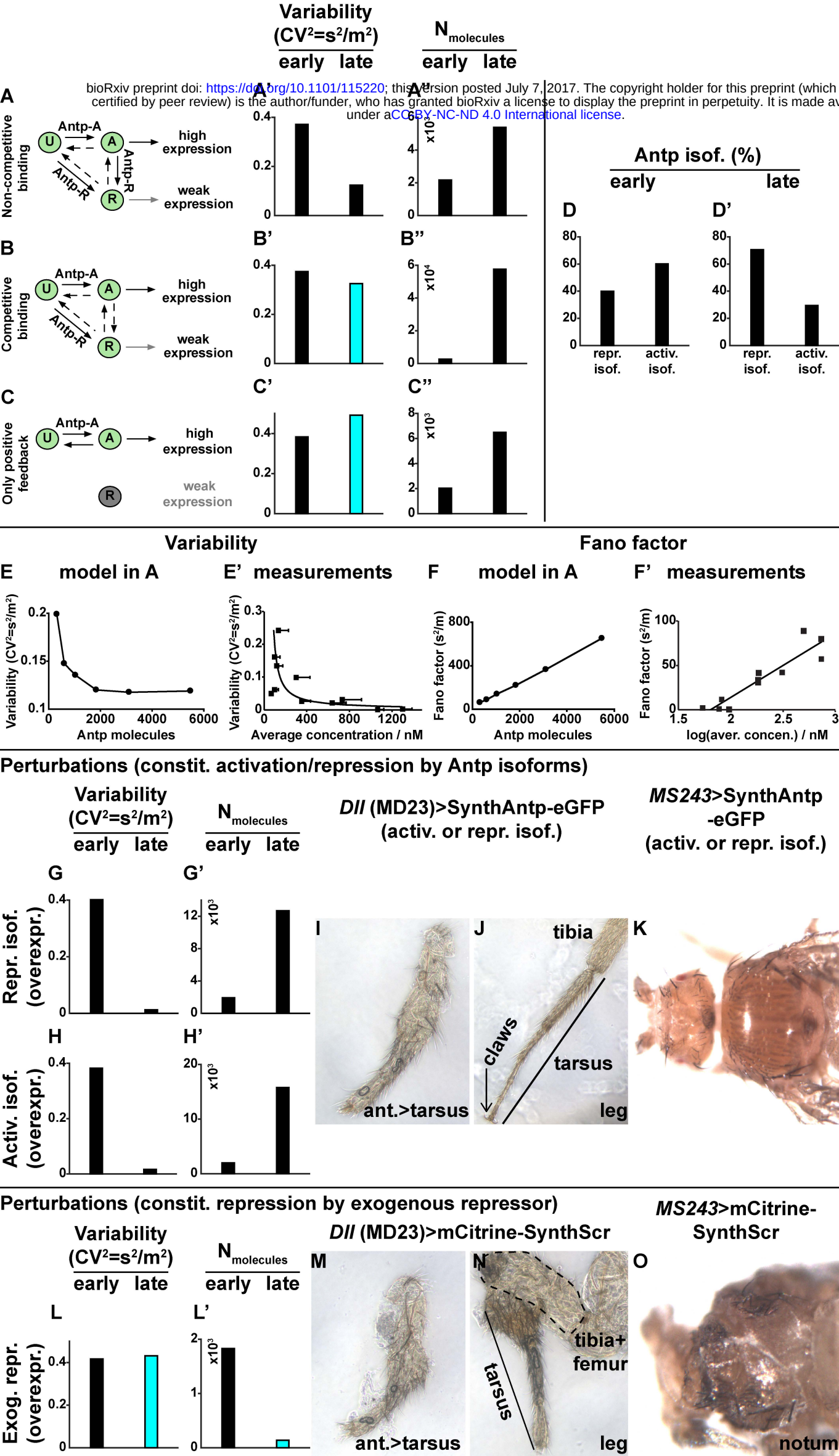

Figure 5 - figure supplement 1

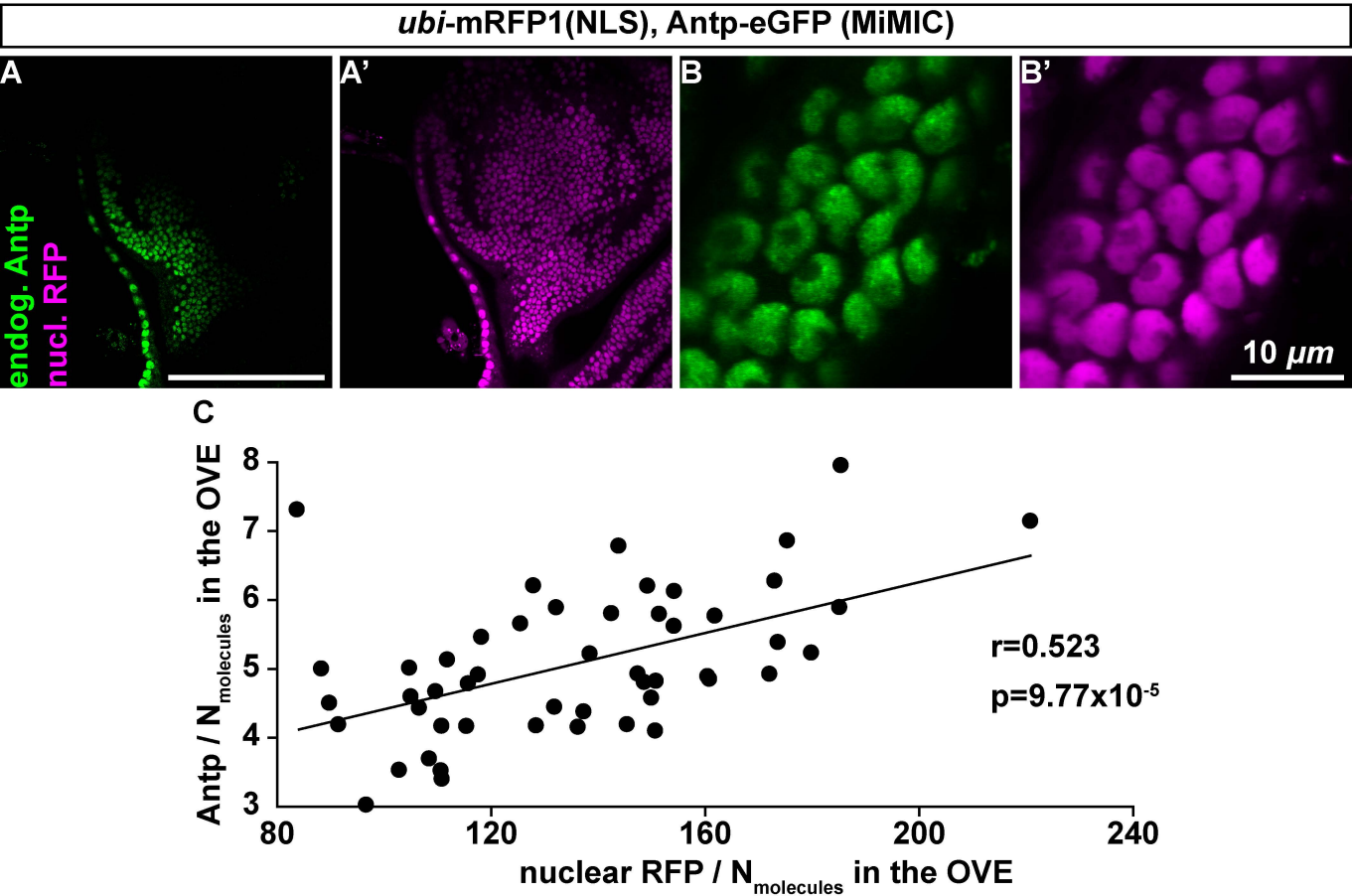

Figure 5 - figure supplement 2